MONASH University

Simulating the Flow of Semidilute Polymer Solutions

by

Chandi Sasmal

M. Tech (I.I.T. Kanpur)

A thesis submitted for the degree of Doctor of Philosophy at

Monash University in 2016

in the

Molecular Rheology Group

Department of Chemical Engineering

Monash University

Clayton, Australia

August 29, 2016

Copyright notice

Dedicated to my beloved parents

and

to my wife Shrabanti
for their unconditional support and love

Abstract

There are a number of contexts involving polymer solutions, such as in the spinning of nano-fibres or in inkjet printing, where in order to achieve the most optimal outcome, the concentration of polymers must not be too dilute or too concentrated, but somewhere in between. While a lot is known about dilute and concentrated solutions and melts, not much is known about the vast regime of concentrations that lie in between, the so-called semidilute concentration regime. The reason much is known about dilute and concentrated solutions is because in either case, their behaviour can be understood by understanding the behaviour of single molecules. In the dilute case, this is obvious since there are few molecules interacting with each other. In the concentrated case, by treating all the molecules that surround a particular molecule as obstacles that constrain its motion, the entire problem is reduced to understanding the motion of a polymer in a tube. These approximations, however, are not valid in semidilute solutions and the problem of having to account for all the many-body interactions that arise in this regime must be addressed. The onset of the semidilute regime occurs at surprisingly low concentrations because even though the monomer concentration is very low, their being strung together into polymers that are extended objects in space gives rise to the early emergence of interactions.

The broad aim of this thesis is to develop a predictive understanding of the flow behaviour of semidilute polymer solutions. In order to achieve this, firstly, an optimised mesoscopic multi-particle Brownian dynamics (BD) simulation algorithm is developed that is capable of accurately capturing both excluded volume and hydrodynamic interactions, and which can predict rheological properties of semidilute polymer solutions in shear, extensional and mixed flows. Secondly, the multi-particle BD algorithm is used to solve a number of different physical problems involving flowing semidilute polymer solutions, as discussed in greater detail below.

The first part of the thesis describes the details of the development of an optimised BD algorithm for semidilute polymer solutions. In particular, the implementation of an efficient smooth particle mesh Ewald (SPME) method. Simulating the properties of polymer solutions at finite concentrations is challenging because of the presence of long-ranged hydrodynamic interactions. The summation of these long-ranged interactions over all pair-wise interactions, in the presence of periodic boundary conditions (PBCs) is difficult because the sum is only conditionally convergent, making its direct evaluation impractical. The Ewald summation technique has been successfully used as a means of tackling this problem. A naive implementation of the Ewald sum leads to an algorithm that scales as $O(N^2)$, where N is the total number of monomers in the simulation box. Recently, Jain et al. (2012b) developed an optimized BD algorithm that scales as $O(N^{1.5})$ based on the optimization technique proposed by Fincham (1994). However, this speedup is insufficient to examine the large systems (with roughly 10^3 to 10^4 monomers), necessary to explore the universal scaling behavior of semidilute polymer solutions. Many attempts to mitigate this problem have led to the development of highly sophisticated algorithms whose computational cost typically scale as $O(N \ln N)$. One of these is the SPME method (Essmann et al., 1995) which effectively uses fast Fourier transforms (FFT) to evaluate the reciprocal part of the Ewald sum. Here, the SPME method is implemented for the Rotne-Prager-Yamakawa tensor, and a straightforward and simple technique for tuning the parameters associated with the method is introduced that renders the computational cost optimal.

The first physical problem examined with the optimised BD algorithm is that of planar mixed flows, which are linear combinations of planar shear and extensional flows. Periodic boundary conditions are implemented to account for lattice deformation due to flow by adopting Less-Edwards PBCs for shear flows and Kraynik-Reinelt PBCs for mixed and extensional flows (Jain et al., 2015). Planar mixed flows are characterized by a mixedness parameter, χ and a flow strength parameter, $\dot{\Gamma}$. In the limit of $\chi \to 0$, the flow is pure shear, while for $\chi \to 1$, it

is purely extensional. The influence of χ, and $\dot{\Gamma}$ on the size of polymer chains, $< R_{\mathrm{e}}^2 >$ and the polymer contribution to viscosity, η, is examined. In dilute polymer solutions, it has been shown that there exists a critical mixedness parameter, χ_c, below which the flow is shear dominated, while being extension dominated for $\chi > \chi_c$. Here we determine the scaling of χ_c with concentration, solvent quality, and chain length.

Nearly 40 years ago, De Gennes predicted the phenomenon of "coil-stretch hysteresis" exhibited in polymer solutions undergoing extensional flows (De Gennes, 1974). There have been a number of theoretical, numerical and experimental investigations carried out in order to prove the existence of this phenomenon. All these studies, however, have been carried out in the ultra-dilute limit of polymer solutions. To date, there are no simulations or experimental investigations of the influence of concentration on the extent of coil-stretch hysteresis. Simulations carried out with the present multi-particle BD algorithm indicate that there is an increase followed by a decrease in the coil-stretch hysteresis window size with increasing concentration. The simulation results are supported by recent scaling arguments and experimental results at Monash University by Prabhakar and Sridhar, respectively. Furthermore, the competitive influence of polymer concentration and flow mixedness on the magnitude of the hysteresis window in polymer solutions undergoing planar mixed flows, is investigated.

Several studies of single molecules of fluorescently labelled DNA have been carried out in the past in order to gain insight into the conformational evolution of polymer chains when subjected to a variety of flow fields (Mai et al., 2012). These studies have have not only enabled the direct visual observation of "molecular individualism", but have also proved to be of vital importance for the validation of molecular theories of polymer dynamics. However, nearly all these investigations have been carried out in either the dilute or concentrated solution regimes, with only a few in the semidilute regime. The recent single molecule experiments of Hsiao et al. (2016) on planar extensional flow of unentangled semidilute solutions

of λ-phage DNA, provide benchmark data against which molecular theories can be verified in the semidilute regime. Here, the multi-chain BD algorithm is used along with the successive fine-graining technique (Sunthar and Prakash, 2005), to obtain predictions that are independent of model parameters, and the results are shown to agree quantitatively with the experimental observations of Hsiao et al. (2016).

Declaration

This thesis contains no material which has been accepted for the award of any other degree or diploma at any university or equivalent institution and that, to the best of my knowledge and belief, this thesis contains no material previously published or written by another person, except where due reference is made in the text of the thesis.

Chandi Sasmal

Acknowledgements

First and foremost, I would like to convey my sincere thanks to my PhD supervisor, Prof. Ravi Prakash Jagadeeshan for his continuous invaluable support, encouragement, suggestions and guidance for the completion of this work. Moreover, thanks again to him for giving me the opportunity to get an insight into the areas of "Polymer Physics" and "Brownian dynamics simulation".

I thank Dr. Prabhakar Ranganathan and Prof. Burkhard Dünweg for their many fruitful suggestions and discussions. I would like to thank to Prof. Charles M. Schroeder and Kaiwen Hsiao for their help and support in accomplishing an wonderful and successful collaborative work. I would like to thank to all my past and present molecular rheology group members for giving me such a welcoming and energetic environment in the group. Special thanks to Dr. Aashish Jain, Dr. Anuja Mehrotra, Emma and Chamath for their entertainment, encouragement and precious responses all the time. My heartfelt thanks to all my friends whose support makes my journey a memorable one at Monash which I will cherish for the rest of my life.

I wish to thank to the Department of Chemical Engineering, Monash University and Monash Institute of Graduate Research (MIGR) for giving me the APA and IPRS scholarships to carry out this research work. My sincere thanks to all the staff members of the Chemical Engineering department, specially Lilyanne and Jill, for their help on administrative matters. This work would not have been possible without the supercomputer resources. So I would like to thank to the National Computational Infrastructure (NCI), Victorian Life Sciences Computation Initiative and Victorian Partnership for Advanced Computing (VLSCI), and Monash SunGrid for giving me the CPU time on their supercomputers.

Finally, I would like to express my reverence and great admiration for my beloved parents for giving me the all strength, inspiration and a guiding force for all of my life.

Contents

xiv

List of Figures

xxii

List of Tables

Chapter 1

Introduction

A polymer is a large molecule or macromolecule consisting of many repeated subunits or monomers. Because of their broad range of properties, these molecules are used as building blocks of many manufacturing products such as paints, pastes, fibers, films, to name but a few, which play an essential and ubiquitous role in our daily life. Polymer solutions, formed when polymer molecules are added in suitable solvents, are routinely used in varieties of industries ranging from chemical, petrochemical, food to pharmaceutical and biomedical industries. This attests to the importance of understanding polymer solutions, with their rich variety of physical and chemical properties, from a fundamental and practical point of view. Extensive investigations of polymeric solutions have been carried out in the past because of their interesting physical and chemical properties and of their technological applications. At present, we have an excellent understanding of the dynamics of dilute polymer solutions and of concentrated polymer solutions and melts by means of theoretical analysis, numerical simulations and experiments. However, not much is known about the vast regime of polymer solutions that lie in between the dilute and concentrated regimes; a regime that has unique behaviour and properties, the so-called *semidilute* concentration regime. In many practical applications involving polymer solutions, the concentration of the solutions must not be too dilute or too concentrated but it must be in semidilute regime in order to achieve the most optimal outcome. For instance, in making of nanofibers by electrospinning, semidilute polymer solutions are mandatory in order to get solid,

continuous and uniform nanofibers (Ramakrisna et al., 2005). This is because good quality nanofibers with unique mechanical and thermodynamic properties can not be obtained either by using dilute polymer solutions, which tend to break into small droplets under the influence of the external forces in the electrospinning process, or by using concentrated polymer solutions, for which it is difficult to maintain the diameter as well as the microstructure of the nanofibers. For the same reason, semidilute polymer solutions are also widely used in inkjet printing, which creates a digital image by pushing droplets of ink onto paper (Gans et al., 2004). An advanced understanding of semidilute polymer solutions is also necessary in the context of cell biology, specially, in living cell organisms. In a typical cell, 30 % of the cytoplasmic environment is occupied by macromolecules of varying size and nature, and hence the fluidic environment containing these biomacromolecules behaves like a semidilute polymer solution, and the movement of different types of proteins and the mechanism of different protein-protein interactions within this cell environment will be better understood once the physics of semidilute polymer solutions is well understood (Kozer et al., 2007). Further, the diffusion mechanism of different types of nanoparticles within a crowded biological cell of macromolecules, which is a well-known path for targeted drug delivery, will also be clarified if the semidilute regime is well investigated (Omari et al., 2009). Therefore, understanding the static and dynamic properties of semi-dilute polymer solutions is not only of fundamental importance, but is also vitally important for a number of practical applications.

The main aim of the present thesis is to develop a predictive understanding of the flow behaviour of semidilute polymer solutions. In order to achieve this, firstly, an optimized multi-particle Brownian dynamics (BD) algorithm is developed that is capable of simulating semidilute polymer solutions when subjected to various kinds of flows, e.g., shear flows, extensional flows or a mixture of both. Secondly, the multi-particle BD algorithm is used to solve a variety of interesting problems involving flowing semidilute polymer solutions. In particular, the broad objectives

of the present thesis can be listed as the following set of tasks:

1. Development of an optimized Brownian dynamics (BD) algorithm based on the smooth particle mesh Ewald (SPME) method.

2. Investigation of the dynamics of polymer molecules undergoing planar mixed flows at finite concentrations of polymer solutions.

3. Parameter-free prediction of DNA dynamics in planar extensional flow of semidilute solutions by the successive fine-graining (SFG) technique.

4. Study of the influence of concentration on the coil-stretch hysteresis phenomena exhibited in polymer solutions undergoing planar extensional and mixed flows.

In this introductory chapter, after defining more precisely what is meant by a semidilute solution, each of these objectives is briefly motivated below, while a detailed discussion is given in subsequent chapters.

1.1 Semidilute polymer solutions

One of the key variables that determines the behaviour of a polymer solution is the monomer concentration, c, (which is defined as the total number of monomers per unit volume of the solution). Additionally, the molecular weight of the polymer molecule, M_{w}, and the temperature, T, also play an important role in determining the behaviour of a polymer solution. The concentration of a polymer solution is often specified in terms of the scaled variable c/c^* instead of only c, where c^* is the *overlap* concentration. The definition of the overlap concentration is as below

$$c^* = \frac{\text{Total number of monomers in a polymer molecule}}{\text{Volume of a linear polymer chain}} = \frac{N_b}{\frac{4}{3}\pi R_g^3} \qquad (1.1)$$

The volume of a linear polymer chain can be approximated as the volume of a sphere of radius R_g as shown in Fig. 1.1, where R_g is the radius of gyration of

a polymer molecule. At low polymer concentration, as schematically shown in
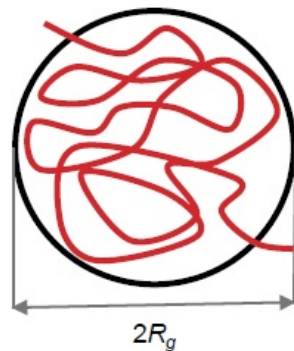
FIGURE 1.1: Approximation for the volume of a linear polymer chain

Fig. 1.2(a), these spheres of radius R_g are far apart from each other and they do not interact with each other, and this regime of polymer solution is called the *dilute* regime ($c \ll c^*$). As the polymer concentration gradually increases, polymer chains become congested and start to interact with each other. When the
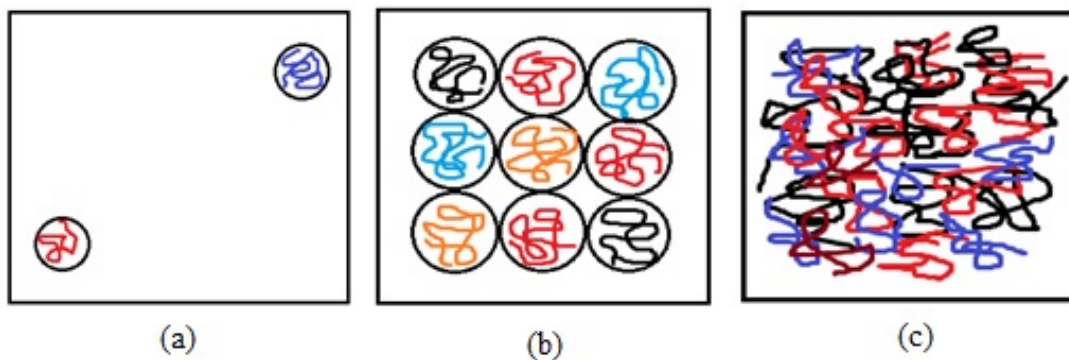
FIGURE 1.2: Different regimes of polymer solutions

polymer concentration becomes equal to the overlap concentration c^*, individual polymer chains just begin to touch other other so that they start to interact with each other, and the whole domain of the polymer solution is filled with touching spheres of radius R_g as depicted in Fig. 1.2(b). The semidilute regime of polymer solutions is considered to start at $c \cong c^*$. On the other hand, if the polymer concentration is much higher than the overlap concentration ($c \gg c^*$), then it is called a concentrated polymer solution where molecules entangle with each other as shown in Fig. 1.2(c).

In the literature, there are voluminous studies on dilute and concentrated polymer solutions because in either case, their behaviour can be understood by understanding the behaviour of single molecules. In the dilute case, this is obvious since there are few molecules interacting with each other. In the concentrated case, by treating all the molecules that surround a particular molecule as obstacles that constrain its motion, the entire problem is reduced to understanding the motion of a polymer in a tube (Doi and Edwards, 1986). These approximations, however, are not valid in semidilute solutions and the problem of having to account for all the many-body interactions that arise in this regime must be addressed. The onset of the semidilute regime occurs at surprisingly low concentrations because even though the monomer concentration is very low, their being strung together into polymers that are extended objects in space gives rise to the early emergence of interactions (Rubinstein and Colby, 2003).

In order to model polymer solutions, two significant interactions must be taken into account. The first is the excluded volume interaction which simply states that two monomers can not occupy the same place at the same time. This interaction is short-ranged in space but long-ranged along the backbone of the polymer chains. The other important interaction that occurs in polymer solutions is the hydrodynamic interaction, which is a solvent-mediated interaction which is long-ranged in space. This interaction arises due to the fact that if one part of a molecule moves then it disturbs the solvent close to it, which eventually disturbs the movement of other parts of the same molecule. This is called intra-molecular hydrodynamic interactions. Moreover, the movement of one part of a molecule disturbs the movement of parts of other surrounding molecules as well. This is called inter-molecular hydrodynamic interactions. In dilute polymer solutions, both excluded volume and hydrodynamic interactions exist, however, it is sufficient to account for only intra-molecular hydrodynamic interactions, whereas for semidilute polymer solutions, one has to incorporate both intra and inter-molecular hydrodynamic interactions

into molecular theories to understand the behaviour of this regime of polymer solutions. It should be mentioned here that both the hydrodynamic and excluded volume interactions disappear in concentrated solutions and melts (Rubinstein and Colby, 2003) and hence, one may think of the semidilute regime as the regime of polymer solutions where these interactions are gradually screened with increasing polymer concentration.

1.2 Brownian dynamics algorithm optimisation

The understanding of semidilute polymer solutions are mostly based on the theoretical scaling laws developed around the concepts of either *blob models* or the *screening* of different interactions as mentioned above (De Gennes, 1979; Rubinstein and Colby, 2003; De Gennes, 1979; De Gennes, 1976a; De Gennes, 1976b; Muthukumar and Edwards, 1982; Muthukumar and Edwards, 1983; Richter et al., 1984; Shiwa et al., 1988; Brown and Nicolai, 1990; Shiwa, 1995; Doi and Edwards, 1986). However, in recent years, significant progress in the development of mesoscopic simulation techniques has made it possible for the first time to obtain detailed predictions of equilibrium and non-equilibrium properties of semidilute polymer solutions that can be compared directly with experimental measurements. These mesoscopic simulation techniques, on one hand, should accurately depict the semidilute regime of polymer solutions, and on the other hand, must be capable of accurately capture the solvent mediated long-ranged intra and intermolecular hydrodynamic interactions. So far, three different mesoscopic simulation techniques, all of which use coarse-grained bead-spring chain models to represent a polymer molecule, have been developed to achieve these purposes. Two of these techniques, namely, the hybrid Lattice Boltzmann/Molecular Dynamics (LB/MD) method (Ahlrichs and Dünweg, 1999; Dünweg and Ladd, 2008) and the hybrid Multi-particle Collision Dynamics/Molecular Dynamics (MPCD) method treat the

solvent molecules explicitly (Malevanets and Kapral, 1999; Kapral, 2008; Gompper et al., 2009). As a consequence, hydrodynamic interactions between polymer segments arise naturally through the exchange of momentum between the beads on a chain and solvent molecules. In the third approach (Stoltz, 2006; Stoltz et al., 2006), which is based on Brownian dynamics (BD) simulations (Öttinger, 2012), the solvent degrees of freedom are removed completely, but their effect is taken into account through long-range dynamic correlations in the stochastic displacements of the polymer beads. The present study has adopted the later approach in order to simulate semidilute polymer solutions.

There are two main difficulties associated with the simulation of semidilute polymer solutions using the Brownian dynamics approach. First, one needs to implement periodic boundary conditions (PBCs) in order to describe homogeneous polymer solutions in unbounded domains, necessitating the simulation of a large number of particles. As a result, the computational effort becomes an important consideration in the BD simulation technique. Secondly, simulating semidilute polymer solutions is challenging because of the presence of long-ranged hydrodynamic interactions, which requires the summation over all pair-wise interactions. In the presence of periodic boundary conditions (PBCs), this is difficult because the sum is only conditionally convergent, making its direct evaluation impractical. The Ewald summation technique has been successfully used as a means of tackling this problem (Ewald, 1921). A naive implementation of the Ewald sum leads to an algorithm that scales as $O(N^2)$, where N is the total number of monomers in the simulation box. Recently, Jain *et al.* (Jain et al., 2012b) developed an optimized BD algorithm that scales as $O(N^{1.5})$ based on the optimization technique for electrostatic interactions proposed by Fincham (1994). However, this speedup is insufficient to examine the large systems (with roughly 10^3 to 10^4 monomers), necessary to explore the universal scaling behavior of semidilute polymer solutions. Many attempts to mitigate this problem have led to the development of highly sophisticated algorithms whose computational cost typically scale as $O(N\ln N)$. One

of these is the smooth particle particle mesh Ewald (SPME) method (Essmann et al., 1995) which effectively uses fast Fourier transforms (FFT) to evaluate the reciprocal part of the Ewald sum. Only recently, Saadat and Khomami (Saadat and Khomami, 2015a) have implemented the SPME technique for the Rotne-Prager-Yamakawa (RPY) tensor for treating hydrodynamic interactionsin in the context of Brownian dynamics simulations for simulating semidilute polymer solutions. However, there is a still lack of knowledge on how the parameters associated with this method can be optimized so that it can lead to an optimal computational cost. One of the aims of the present study is to implement the SPME method in a BD algorithm, and to introduce a straightforward and simple technique for tuning the parameters associated with this method, such that the computational cost is optimal.

1.3   Planar mixed flows at finite concentration

Almost all of the applications mentioned at the start of this chapter involve semidilute polymer solutions undergoing different kinds of flows. Therefore, it is very important to understand the behaviour of flowing semidilute polymer solutions. However, simulating flowing semidilute solutions is more difficult than those at equilibrium. This is because unlike the simulation of equilibrium systems, where periodic boundary conditions (PBCs) are used in an orthogonal cell to get rid of wall effects, simulating far from equilibrium systems need appropriate PBCs to be used such that the following two requirements are met: (i) The PBCs should be compatible with any particular flow and (ii) the simulation should be capable of running for an arbitrary amount of time. PBCs for planar shear flow and planar elongational flow were developed by Lees and Edwards (1972) and Kraynik and Reinelt (1992) respectively, such that the two requirements mentioned above were fulfilled. Lees-Edwards and Kraynik-Reinelt PBCs have been used by Bhupathiraju et al. (1996) and Todd and Daivis (1998) in their nonequilibrium molecular

dynamics (NEMD) simulation algorithms. Other than NEMD simulations, these PBCs have also been implemented in a BD algorithm by Stoltz et al. (2006) to simulate semidilute polymer solutions undergoing planar shear or planar elongational flows. In real flow situations, however, rather than only shear or elongational flow, a combination of these flows is often observed. Woo and Shaqfeh (2003); Dua and Cherayil (2003) and Hoffman and Shaqfeh (2007) have simulated dilute polymer solutions in planar mixed flow using a BD algorithm in which PBCs were not required. In a recent paper, Hunt et al. (2010) have derived suitable PBCs for planar mixed flow (which is a linear combination of planar elongational flow and planar shear flow) and implemented them in their nonequilibrium molecular dynamics (NEMD) simulation algorithm. Only recently, for the first time, PBCs for planar mixed flow have been implemented for a multichain Brownian dynamics simulation algorithm, which enables the simulation of semidilute polymer solutions undergoing different kinds of flows (Jain et al., 2015; Jain, 2013).

Here, this algorithm is used to examine the effect of shear rate and extension rate on the size of polymer chains, and on the polymer contribution to viscosity, for solutions of FENE dumbbells at finite concentrations, with excluded volume interactions between the beads taken into account. The influence of the mixedness parameter, χ, and flow strength, $\dot{\Gamma}$, is also examined, where $\chi \to 0$ corresponds to pure shear flow, and $\chi \to 1$ corresponds to pure extensional flow. In particular, the existence of a critical value, $\chi_{\rm c}$, such that the flow is shear dominated for $\chi < \chi_{\rm c}$, and extension dominated for $\chi > \chi_{\rm c}$, is established.

1.4 Parameter free prediction of DNA dynamics

Single molecule techniques, using fluorescently labelled DNA, have been extensively used to gain insight into the conformational evaluation of polymer chains when subjected to a variety of flow fields (Perkins et al., 1994a; Perkins et al., 1994b; Wirtz, 1995; Perkins et al., 1997; Shaqfeh, 2005; Teixeira et al., 2007; Mai

et al., 2012; Marciel and Schroeder, 2013; Harasim et al., 2013). These studies, on one hand, have enabled the direct visual observation of "molecular individualism" and on the other hand, have proved to be of vital importance for the validation of molecular theories of polymer dynamics (Larson et al., 1999; Jendrejack et al., 2002; Hsieh et al., 2003; Sunthar and Prakash, 2005). However, most of these investigations have been carried out in the dilute or concentrated regimes of polymer solutions, with only a few in the semidilute regime (Liu et al., 2009; Hur et al., 2001; Harasim et al., 2013). In the dilute limit, studies have proven the importance of properly accounting for hydrodynamic and excluded volume interactions in molecular theories in order to accurately predict experimental observations (Jendrejack et al., 2002; Hsieh et al., 2003; Sunthar and Prakash, 2005). However, in the semidilute regime of polymer solutions, it is well known that these interactions gradually get screened with increasing polymer concentration. Therefore, the question arises whether molecular theories are able to accurately capture the subtle changes that occur on the molecular scale, as chains begin to interact and interpenetrate with each other with increasing monomer concentration in the semidilute regime. The recent single molecule experiments of Hsiao et al. (2016) on planar extensional flow of unentangled semidilute solutions of λ-phage DNA provide the benchmark data against which the molecular theories can be verified. One of the main aims of the present thesis is to carry out simulations with a multi-chain BD algorithm in order to investigate the stretching dynamics of λ-phage DNA in an extensional flow, and the relaxation phenomena upon cessation of flow, as a function of Weissenberg number in both the dilute and semidilute regimes of polymer solutions, and then perform a detailed quantitative comparison with the experimental observations of Hsiao et al. (2016).

1.5 Coil-stretch hysteresis at finite concentrations

Single molecule studies have also been used in order to prove the existence of the "coil-stretch hysteresis" phenomena exhibited in polymer solutions. Nearly 40 years ago, this phenomena was predicted by de Gennes, who conjectured that polymer solutions could have different states of stress at the same strain rate, if their deformation histories were different (De Gennes, 1974). This phenomenon, if true, would have significant impact on a variety of industrial applications involving polymer solutions, such as ink-jet printing and the spinning of nano-fibres. The existence of coil-stretch hysteresis was a highly debated topic for several decades within the rheology community, and there have been a number of theoretical and numerical investigations. However, in 2003, nearly 30 years after de Gennes's hypothesis, the first experimental proof was obtained by Schroeder et al. (2003) using stained DNA molecules undergoing elongational flow in a cross-slot cell. Many Brownian dynamics simulations were also carried out to support the existence of this phenomena (Agarwal et al., 1998; Hsieh and Larson, 2005; Prabhakar and Prakash, 2006). All these studies, however, were carried out in the ultra-dilute limit, i.e., by observing the conformation (in the case of experiments) and performing simulations on single polymer molecules. From an industrial application perspective, on the other hand, polymer solutions are hardly likely to be in the ultra-dilute limit, but are more likely to be at finite concentrations. To the best of our knowledge, there are no prior simulations, or experimental investigations, on how concentration influences the extent of coil-stretch hysteresis exhibited in polymer solutions. One of the main aims of the present study is to examine the non-monotonic influence of concentration on the extent of coil-stretch hysteresis. Our simulation results are supported by recent scaling arguments of Prabhakar (Prabhakar et al., 2016), and experiments carried out by Sridhar and Nguyen at Monash University. Moreover, de Gennes in his original theory predicted that in planar mixed flows, the coil-stretch hysteresis window would progressively decrease with

increasing shear rate. We investigate the competitive influences of polymer concentration and flow mixedness on the extent of coil-stretch hysteresis in polymer solutions undergoing planar mixed flows, and map out the dependence of window size on concentration and shear rate.

The structure of the present thesis is as follows: In Chapter 2, the details of the polymer model and the governing equations for the multi-chain BD simulations along with the mathematical treatment of excluded volume and hydrodynamic interactions are presented. The implementation of the smooth particle mesh Ewald method and its optimization technique in the context of the present BD simulations is discussed in Chapter 3. Chapter 4 describes the dynamics of polymer molecules undergoing planar mixed flows at finite concentrations. In Chapter 5, BD simulations are carried out to study the dynamics of single DNA molecules in semidilute solutions undergoing planar extensional flows, and a detailed quantitative comparison between the present predictions with the experimental observations of Hsiao et al. (2016) is presented. The effect of concentration on the size of the "coil-stretch hysteresis" window exhibited in polymer solutions undergoing planar extensional and mixed flows is investigated in Chapter 6. Finally, the central conclusions of the present thesis and scope for the future work are presented in Chapter 7.

Chapter 2

Governing Equations for the Bead-Spring Chain Model

This chapter presents the model for describing a polymer molecule, and the basic governing equations of the Brownian dynamics simulation method in the context of a multi-chain system. The mathematical treatment of two important microscopic phenomena occurring at the molecular level, namely, hydrodynamic and excluded volume interactions are also discussed in the context of BD simulations. Finally, the velocity gradient tensor for different kind of flows, and the formulae to calculate the mean values of various equilibrium and rheological properties are presented.

2.1 The polymer model and representation of a semidilute polymer solution

A bead-spring chain model is used to represent polymer molecules whereby each molecule is coarse-grained into a sequence of N_b beads (which act as centers of hydrodynamic resistance) connected by $N_b - 1$ massless springs that represent the entropic force between two adjacent beads as presented in Fig. 2.1. A semidilute polymer solution is obtained by immersing of an ensemble of such bead-spring chains in an incompressible Newtonian solvent. The bulk concentration (c) of the solution is defined as $\frac{N}{V}$ where $N = N_b \times N_c$ is total number of beads per cubic and

periodic simulation cell of edge length L, giving a total volume of $V = L^3$, with N_c chains initially enclosed in it. Fig. 2.2 schematically shows a simple example of the simulation system in 2-D.
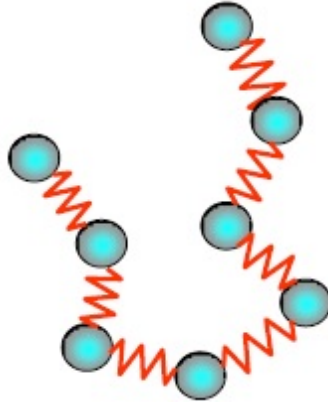
FIGURE 2.1: Bead-spring chain model of polymer molecule.
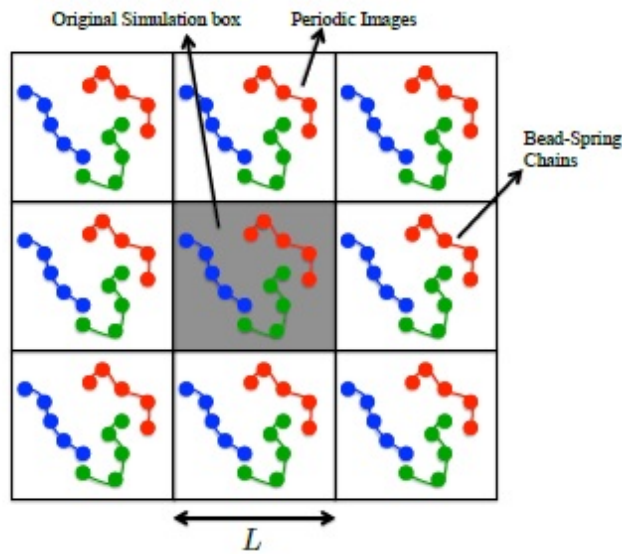
FIGURE 2.2: A schematic illustration of the simulation system in 2-D, showing an example of a system with box size L, number of chains $N_c = 3$ and number of beads in a chain $N_b = 5$. The central grey box indicates the original simulation box, whereas the surrounding white boxes are the periodic images of it.

2.2 Governing equations of the Brownian dynamics algorithm

The following non-dimensional Ito stochastic differential equation based on the Euler integration scheme governs the position vector $\mathbf{r}_\nu(t)$ of bead ν of a polymer chain with time t

$$
\mathbf{r}_\nu(t + \Delta t) = \mathbf{r}_\nu(t) + [\boldsymbol{\kappa} \cdot \mathbf{r}_\nu(t)] \, \Delta t + \frac{\Delta t}{4} \sum_{\mu=1}^{N} [\mathbf{D}_{\nu\mu}(t) \cdot \mathbf{F}_\nu(t)] + \\
\frac{1}{\sqrt{2}} \sum_{\mu=1}^{N} [\mathbf{B}_{\nu\mu}(t) \cdot \boldsymbol{\Delta W}_\nu(t)]
\tag{2.1}
$$

Here the length and time units are non-dimensionalized using a length scale $l_H = \sqrt{k_B T / H}$ and a time scale $\lambda_H = \zeta / 4H$ respectively, where T is the temperature, H is the spring constant, k_B is the Boltzman's constant, and ζ is the hydrodynamic friction coefficient associated with a bead. In Eq. (2.1), $\boldsymbol{\kappa}$ is a time dependent and homogeneous velocity gradient tensor which is equal to $(\boldsymbol{\nabla v})^T$ with $\boldsymbol{v}$ being the unperturbed solvent velocity. The non-dimensional diffusion tensor $\mathbf{D}_{\nu\mu}$ is a 3×3 square matrix for a fixed pair of particles μ and ν, which is related to the dimensionless hydrodynamic interaction tensor, $\boldsymbol{\Omega}$, as follows:

$$
\mathbf{D}_{\nu\mu} = \delta_{\nu\mu}\boldsymbol{\delta} + (1 - \delta_{\nu\mu})\boldsymbol{\Omega}(\mathbf{r}_\nu - \mathbf{r}_\mu)
\tag{2.2}
$$

where $\boldsymbol{\delta}$ and $\delta_{\mu\nu}$ represent a unit tensor and Kronecker delta respectively. The aforementioned hydrodynamic interaction tensor is represented by the Rotne-Prager-Yamakawa (RPY) tensor which is discussed further subsequently. The force, $\mathbf{F}_\nu$, incorporates all the non-hydrodynamic forces acting on bead ν due to the presence of all other beads, for instance, in the present study, these are the spring forces and excluded volume interaction forces, i.e., $\mathbf{F}_\nu = \mathbf{F}_\nu^{\mathrm{spr}} + \mathbf{F}_\nu^{\mathrm{exv}}$, discussed in greater detail below. The term $\mathbf{B}_{\nu\mu}$ is a non-dimensional tensor which is responsible for multiplicative noise, and is evaluated by decomposing the diffusion

tensor as follows:

$$\boldsymbol{\mathcal{B}} \cdot \boldsymbol{\mathcal{B}}^{\mathrm{T}} = \boldsymbol{\mathcal{D}} \tag{2.3}$$

where $\boldsymbol{\mathcal{B}}$ and $\boldsymbol{\mathcal{D}}$ are the block matrices consisting of $N \times N$ blocks each having dimensions 3×3, with the (ν, μ)th block of $\boldsymbol{\mathcal{D}}$ containing the components of the diffusion tensor $\mathbf{D}_{\nu\mu}$, and the corresponding block of $\boldsymbol{\mathcal{B}}$ being equal to $\mathbf{B}_{\nu\mu}$. The components of the Gaussian noise $\boldsymbol{\Delta W}_{\nu}$ are obtained from a real-valued Gaussian distribution with zero mean and variance Δt. In Eq. 2.1, there are three terms that are challenging to implement efficiently, namely, (i) the flow term $[\boldsymbol{\kappa} \cdot \mathbf{r}_{\nu}(t)]$ (ii) the diffusion term $\sum_{\mu=1}^{N} [\mathbf{D}_{\nu\mu}(t) \cdot \mathbf{F}_{\nu}(t)]$, and (iii) the drift term $\sum_{\mu=1}^{N} [\mathbf{B}_{\nu\mu}(t) \cdot \boldsymbol{\Delta W}_{\nu}(t)]$. The implementation and optimization of the latter two terms are presented by Jain *et al.* (Jain et al., 2012b; Jain, 2013), whereas the implementation of the flow term can be found in Jain et al. (2015) and Jain (2013).

The specification of the force term in Eq. 2.1 requires the consideration of bonded and non-bonded interactions that occur between beads. These interactions are discussed below.

2.3   Bonded interactions: Spring forces

The only bonded interactions that are considered in the present study are the spring forces. The entropic spring force, $\mathbf{F}_{\nu}^{\mathrm{spr}}$, on bead ν due to adjacent beads can be expressed as $\mathbf{F}_{\nu}^{\mathrm{spr}} = \mathbf{F}_{\nu}^{c} - \mathbf{F}_{\nu-1}^{c}$, where $\mathbf{F}_{\nu}^{c}$ is the connector force between the beads ν and $\nu + 1$, acting in the direction of the connector vector between two subsequent beads, $\mathbf{Q}_{\nu} = \mathbf{r}_{\nu+1} - \mathbf{r}_{\nu}$. A variety of different potentials have been used to model the spring forces:

- A linear Hookean spring potential:

$$\mathbf{F}^{c}(\mathbf{Q}_{\nu}) = \mathbf{Q}_{\nu} \tag{2.4}$$

- A finitely extensible nonlinear elastic (FENE) potential:

$$\mathbf{F}^c(\mathbf{Q}_\nu) = \frac{\mathbf{Q}_\nu}{1 - |\mathbf{Q}_\nu|^2/b} \tag{2.5}$$

where $b = \frac{HQ_0^2}{k_B T}$ is the dimensionless finite extensibility parameter, with Q_0 being the dimensional maximum stretch of a spring.

- A worm-like chain (WLC) potential:

$$\mathbf{F}^c_{\mathrm{WLC}}(\mathbf{Q}_\nu) = \frac{1}{6q}\left(4q + \frac{1}{(1-q)^2} - 1\right)\mathbf{Q}_\nu \tag{2.6}$$

where, $q = Q/\sqrt{b}$ with Q being the magnitude of the connector vector $\mathbf{Q}_\nu$.

The particular spring force law that is used in the different problems studied here will be clearly stated in the context of the problem.

2.4 Non-bonded interactions

In the present study, we consider two non-bonded interactions, namely, hydrodynamic and excluded volume interactions.

2.4.1 Hydrodynamic interactions (HI)

The hydrodynamic interaction tensor $\boldsymbol{\Omega}$ is given by the Rotne-Prager-Yamakawa (RPY) tensor (Rotne and Prager, 1969; Yamakawa, 1970) which is a regularization of the Oseen-Burgers tensor written in non-dimensional form as,

$$\boldsymbol{\Omega}(\mathbf{r}) = \Omega_1 \boldsymbol{\delta} + \Omega_2 \frac{\mathbf{rr}}{\mathrm{r}^2} \tag{2.7}$$

where $\mathbf{r}$ is the separation distance vector between two beads, and r is its magnitude. For r $\geq 2a$, the functions Ω_1 and Ω_2 are given by

$$\Omega_1 = \frac{3a}{4r}\left(1 + \frac{2a^2}{3r^2}\right) \text{ and } \Omega_2 = \frac{3a}{4r}\left(1 - \frac{2a^2}{r^2}\right) \tag{2.8}$$

while for $0 < r \leq 2a$, the functions Ω_1 and Ω_2 are given by

$$\Omega_1 = \left(1 - \frac{9}{32}\frac{r}{a}\right) \text{ and } \Omega_2 = \left(\frac{3}{32}\frac{r}{a}\right) \tag{2.9}$$

In the above expressions, a is the non-dimensional particle radius which is related to the conventionally defined hydrodynamic interaction parameter h^* by $a = \sqrt{\pi}h^*$ (Thurston and Peterlin, 1967; Bird et al., 1987b). It is well known that the sum, $\sum_{\mu} \mathbf{D}_{\nu\mu} \cdot \mathbf{F}_{\nu}$, in Eq. 2.1 is a conditionally and slowly converging sum. The problem of slow convergence can be resolved through either the use of the Ewald sum (Jain et al., 2012b) or by using the smooth particle mesh Ewald (SPME) method as discussed in the subsequent chapter in greater detail.

2.4.2　Excluded volume interactions (EV)

The other non-hydrodynamic as well as non-bonded force that we consider in the present study is the excluded volume (EV) interaction force which is modelled with a narrow Gaussian potential (Prakash and Öttinger, 1999; Kumar and Prakash, 2003). The non-dimensional form of this potential is given by the following expression

$$E(\mathbf{r}_{\nu\mu}) = z^* \left(\frac{1}{d^{*3}}\right) \exp\left(-\frac{1}{2}\frac{\mathbf{r}_{\nu\mu}^2}{d^{*2}}\right) \tag{2.10}$$

where, z^* is the strength of the excluded volume interactions and d^* is a dimensionless parameter that measures the range of the excluded volume interaction. For reasons elaborated in Refs. Prakash, 2001b; Kumar and Prakash, 2003, the parameter d^* is irrelevant for sufficiently long chains, and is typically calculated

by the expression $d^* = Kz^{*1/5}$, with K being an arbitrary constant. K is set equal to one in all our simulations in the present thesis.

2.5 Velocity gradient tensor for different kind of flows

The velocity gradient tensor for planar shear flow (PSF) in matrix form is (Bird et al., 1987a),

$$(\boldsymbol{\nabla v})_{\text{PSF}} = \begin{pmatrix} 0 & 0 & 0 \\ \dot{\gamma} & 0 & 0 \\ 0 & 0 & 0 \end{pmatrix} \tag{2.11}$$

where, $\dot{\gamma}$ is the shear rate. The simplicity of planar shear flows has motivated many studies that have compared experimental observations with simulation predictions (Larson, 1999; Hur et al., 2000; Hsieh and Larson, 2004; Schroeder et al., 2005).

The velocity gradient tensor for planar elongational flow (PEF) is given by (Bird et al., 1987a),

$$(\boldsymbol{\nabla v})_{\text{PEF}} = \begin{pmatrix} \dot{\epsilon} & 0 & 0 \\ 0 & -\dot{\epsilon} & 0 \\ 0 & 0 & 0 \end{pmatrix} \tag{2.12}$$

where $\dot{\epsilon}$, is the elongational rate. Planar elongational flows occur in many industrial processes, and are generally difficult to study using computer simulations and experimental techniques, since in PEF, fluid elements are stretched exponentially with time in one direction while being contracted in the perpendicular direction (Bird et al., 1987a), leading to a very short span of time in which to observe the phenomena of stretching.

In planar mixed flow (PMF), the velocity gradient tensor has the following form (Fuller and Leal, 1981; Hounkonnou et al., 1992; Hoffman and Shaqfeh,

2007; Hunt et al., 2010)

$$(\boldsymbol{\nabla v})_{\mathrm{PMF}} = \begin{pmatrix} \dot{\epsilon} & 0 & 0 \\ \dot{\gamma} & -\dot{\epsilon} & 0 \\ 0 & 0 & 0 \end{pmatrix} \qquad (2.13)$$

which is referred to as the *canonical form* (Hunt et al., 2010). The expanding direction is along the x-axis and the contracting direction is along the y-axis, with elongational field strength $\dot{\epsilon}$, while the shear gradient is along the y direction, with shear field strength $\dot{\gamma}$. It follows that the expansion axis is always parallel to the x-axis, but the contraction axis is along the direction of one of the eigenvectors of the velocity gradient tensor. While the form of the velocity gradient tensor given by $(\boldsymbol{\nabla v})_{\mathrm{PMF}}$ [Eq. (2.13)] instinctively separates the shear and elongational flow components, it does not permit one to easily study the variation in material behavior as the flow changes smoothly from pure shear to pure elongation or vice versa.

An alternative version of the velocity gradient tensor $(\boldsymbol{\nabla v})$ proposed by Fuller and Leal (1981),

$$(\boldsymbol{\nabla v}) = \begin{pmatrix} 0 & \dot{\Gamma}\chi & 0 \\ \dot{\Gamma} & 0 & 0 \\ 0 & 0 & 0 \end{pmatrix} \qquad (2.14)$$

where $\dot{\Gamma}$ is the characteristic strain rate, and χ ($\in [-1, 1]$) is the mixedness parameter (which measures the relative strength of rotational and elongational components), is more suited to this purpose. It can be shown that this form for $(\boldsymbol{\nabla v})$ reduces to PSF when $\chi \to 0$, while pure PEF is recovered in the limit $\chi \to 1$. Eq. (2.14) is also valid in the limit of $\chi \to -1$, which corresponds to the pure rotational flow limit.

In their studies of PMF of dilute polymer solutions, Hoffman and Shaqfeh (2007) have shown that Eq. (2.14) is equivalent to

$$
(\boldsymbol{\nabla v}) = \begin{pmatrix} \dot{\Gamma}\sqrt{\chi} & 0 & 0 \\ \dot{\Gamma}(1-\chi) & -\dot{\Gamma}\sqrt{\chi} & 0 \\ 0 & 0 & 0 \end{pmatrix} \tag{2.15}
$$

in a suitably rotated coordinate system, where they confine their attention to elongation-dominated mixed flow, for which $\chi > 0$. Clearly, $(\boldsymbol{\nabla v})$ and $(\boldsymbol{\nabla v})_{\mathrm{PMF}}$ are similar in structure. Comparing Eqs. (2.13) and (2.15), we can express the shear rate $\dot{\gamma}$ and elongational rate $\dot{\epsilon}$ in terms of $\dot{\Gamma}$ and χ as follows

$$
\dot{\gamma} = \dot{\Gamma}(1-\chi) \tag{2.16}
$$

and

$$
\dot{\epsilon} = \dot{\Gamma}\sqrt{\chi} \tag{2.17}
$$

The smooth crossover between pure planar shear and pure planar elongational flow limits can be studied by varying χ between 0 and 1.

2.6 Macroscopic properties

Static and dynamic properties of polymer solutions at equilibrium can be calculated once the trajectories of the time evolution of all the beads on all the chains are obtained using Eq. (2.1). For rheological properties, not only are the bead configurations required, it is also necessary to know the forces acting on them.

Two important equilibrium static properties are (i) the end-to-end distance, and (ii) the gyration radius, which are used to assess the mean dimension of a polymer chain (Doi and Edwards, 1986; Rubinstein and Colby, 2003). The end-to-end distance is defined as the mean square distance between the first and the

last beads on a chain,

$$\left\langle R_e^2 \right\rangle = \left\langle (\mathbf{r}_{N_b} - \mathbf{r}_0)^2 \right\rangle \tag{2.18}$$

where, $\langle \cdots \rangle$ represents an ensemble average, and $\mathbf{r}_0$ and $\mathbf{r}_{N_b}$ are position vectors of the first and the last bead, respectively. The mean square gyration radius, which is the mean square distance between the beads and the center of mass $\mathbf{r}_{\mathrm{cm}}$ of the chain is defined by,

$$\left\langle R_g^2 \right\rangle = \frac{1}{N_b} \sum_{\mu=1}^{N_b} \left\langle (\mathbf{r}_\mu - \mathbf{r}_{\mathrm{cm}})^2 \right\rangle \tag{2.19}$$

where, $\mathbf{r}_{\mathrm{cm}} = \frac{1}{N_b} \sum_{\mu=1}^{N_b} \mathbf{r}_\mu$.

The behaviour of polymer solutions, when subjected to an imposed flow, is described by various material functions that are defined in terms of the components of the stress tensor (Bird et al., 1987a). In the absence of external forces, the stress tensor (non-dimensionalized by $n_p\, k_B T$, where n_p is number of polymer chains per unit volume), for a multi-chain system can be shown to be (Stoltz, 2006),

$$\boldsymbol{\sigma} = \frac{1}{N_c} \left[\sum_{\mu=1}^{N} \sum_{\nu=1}^{N} \left\langle \mathbf{r}_{\mu\nu} \mathbf{F}_{\mu\nu}^{\mathrm{exv}} \right\rangle + \sum_{N_c} \sum_{\nu=1}^{N_b-1} \left\langle \mathbf{Q}_\nu \mathbf{F}^c(\mathbf{Q}_\nu) \right\rangle \right] \tag{2.20}$$

In the above equation, the first term is the contribution due to excluded volume forces among the beads, where $\mathbf{r}_{\mu\nu} = \mathbf{r}_\mu - \mathbf{r}_\nu$ is the vector between beads ν and μ, and $\mathbf{F}_{\mu\nu}^{\mathrm{exv}}$ is the excluded volume force between them. The second term is the contribution due to spring forces, where $\mathbf{Q}_\nu$ is the connector vector between the two beads $\mathbf{Q}_\nu = \mathbf{r}_{\nu+1} - \mathbf{r}_\nu$, and $\mathbf{F}^c(\mathbf{Q}_\nu)$ is the spring force between the beads ν and $\nu + 1$.

Once the stress tensor is calculated, the various solution material functions can be estimated. In this thesis, we have focused our attention on the polymer contribution to the solution's viscosity. Hounkonnou et al. (1992) have proposed the following expression for a generalized viscosity η for any arbitrary flow gradient

tensor,

$$\eta = \frac{\dot{\boldsymbol{\Gamma}} : \boldsymbol{\sigma}}{\dot{\boldsymbol{\Gamma}} : \dot{\boldsymbol{\Gamma}}} \qquad (2.21)$$

where $\dot{\boldsymbol{\Gamma}}$ is the rate of strain tensor, defined by $\dot{\boldsymbol{\Gamma}} = (\boldsymbol{\nabla v}) + (\boldsymbol{\nabla v})^{T}$. Using the definition of viscosity in Eq. (2.21), with $(\boldsymbol{\nabla v}) = (\boldsymbol{\nabla v})_{\mathrm{PMF}}$ (see Eq. (2.13)), it is straightforward to show that in planar mixed flows the viscosity is given by,

$$\eta = -\frac{2\dot{\epsilon}(\sigma_{xx} - \sigma_{yy}) + 2\dot{\gamma}\sigma_{xy}}{8\dot{\epsilon}^2 + 2\dot{\gamma}^2} \qquad (2.22)$$

In the limit of pure planar shear flow ($\dot{\epsilon} = 0$), Eq. (2.22) implies,

$$\eta_{\mathrm{PSF}} = -\frac{\sigma_{xy}}{\dot{\gamma}} \qquad (2.23)$$

while in the limit of pure planar elongational flow ($\dot{\gamma} = 0$), Eq. (2.22) leads to,

$$\eta_{\mathrm{PEF}} = -\frac{\sigma_{xx} - \sigma_{yy}}{4\dot{\epsilon}} \qquad (2.24)$$

Note that this definition of the viscosity in planar extension flows differs from the conventional definition of the viscosity $\bar{\eta}_1$ used in the rheology literature (Bird et al., 1987a),

$$\bar{\eta}_1 = -\frac{\sigma_{xx} - \sigma_{yy}}{\dot{\epsilon}} \qquad (2.25)$$

since $\eta_{\mathrm{PEF}} = \bar{\eta}_1/4$. The advantage of the Hounkonnou et al. (1992) definition is that the generalized viscosity reduces to the Newtonian viscosity in the limit of either $\dot{\gamma} \to 0$, or $\dot{\epsilon} \to 0$. We use the Hounkonnou et al. (1992) definition in all our discussions of planar mixed flows. However, we use $\bar{\eta}_1$ when comparing results of the multi-chain algorithm with single chain simulations in planar extensional flows as presented in Chapter 4.

From Eqs. (2.22) to (2.24), the viscosity in planar mixed flows can be rewritten as a linear combination of η_{PSF} and η_{PEF},

$$\eta = \frac{(4\dot{\epsilon}^2 \eta_{\text{PEF}} + \dot{\gamma}^2 \eta_{\text{PSF}})}{4\dot{\epsilon}^2 + \dot{\gamma}^2} \qquad (2.26)$$

Eqs. (2.23) - (2.26) have been used by Hounkonnou et al. (1992), Baranyai and Cummings (1995), Todd and Daivis (1998), Daivis et al. (2003), and Hunt et al. (2010) in their NEMD simulations for the viscosity of various fluids. The PMF viscosity can also be expressed in terms of the strength of mixed flow $\dot{\Gamma}$, and the mixedness parameter χ, by

$$\eta = -\frac{\sqrt{\chi}\,(\sigma_{xx} - \sigma_{yy}) + (1 - \chi)\,\sigma_{xy}}{\dot{\Gamma}\,[4\,\chi + (1 - \chi)^2]} \qquad (2.27)$$

It should be mentioned here that Jain (2013) has used a different definition of PMF viscosity in terms of $\dot{\Gamma}$ and χ, which reduces to the definitions of PSF and PEF viscosity as $\chi \to 0$ (Eq. 2.23) and $\chi \to 1$ (Eq. 2.24), respectively as given by Bird et al. (1987a). However, in all our current simulations of PMF, we use Hounkonnou et al. (1992) definition in order to map smoothly from pure shear flow to pure extensional flow just by changing the value of χ, and use the either Eq. (2.22) or Eq. (2.27) to calculate the viscosity, depending on whether we use the pair $(\dot{\gamma}, \dot{\epsilon})$, or $(\dot{\Gamma}, \chi)$ to describe the flow.

The results in this thesis are mainly presented in terms of the scaled concentration c/c^*, where c^* is the overlap concentration, which is defined by the expression,

$$c^* = \frac{N_b}{\left[(4\pi/3)(R_g^0)^3\right]} \qquad (2.28)$$

with R_g^0 being the radius of gyration for an isolated chain at equilibrium. The value of c/c^* is calculated for each simulation reported in this thesis by computing R_g^0 a priori from single-chain BD simulations at equilibrium, for the relevant set of parameter values. Furthermore, in order to prevent a chain from wrapping over

itself, the initial equilibrium box size L is selected such that $L \geq 2R_e$, where R_e is the end-to-end distance of a chain. For the purpose of selecting the box size, R_e, at any value of c/c^*, is estimated from the blob scaling law $R_e^2 = R_{e0}^2 (c/c^\star)^{\frac{2\nu-1}{1-3\nu}}$, where R_{e0} is the end-to-end distance of a chain computed in the dilute limit.

Chapter 3

Optimization of smooth particle mesh Ewald (SPME) method for treating long-ranged electrostatic and hydrodynamic interactions

3.1 Introduction

In the domain of soft condensed matter physics, there are a variety of non-bonded and long-ranged interactions present. For instance, the long-ranged Coulombic electrostatic interactions acting among charged particles in polyelectrolyte solutions, and (in colloidal suspensions and macromolecular polymer solutions) long-ranged hydrodynamic interactions between particles have been well known for many decades. It is generally difficult to include these pairwise interactions into various mesoscopic simulation techniques, such as, Molecular Dynamics (MD) and Brownian Dynamics (BD) simulations. This is mainly because these interactions decay slowly, and are conditionally convergent in nature. Furthermore, the use of periodic boundary conditions (PBCs) in order to diminish the boundary effects, and to mimic bulk systems, makes this even more difficult. It has been proven that the simple truncation of these interactions leads to artifacts, for instance, in the

case of long-ranged electrostatic interactions, see Hünenberger and McCammon (1999). Therefore, one has to consider pairwise interactions between all particles in order to obtain accurate results, which eventually leads to an unfavourable computational cost. For summing up long-ranged interactions over PBCs, the Ewald summation method (Ewald, 1921) has frequently been used. This method splits the very slowly decaying long-ranged term into two fast converging sums, namely, a direct part, which converges exponentially fast with respect to the distance carried out in the real space, and a reciprocal part, which converges exponentially fast with respect to the number of modes in the Fourier space.

A straightforward implementation of the Ewald method scales as $O(N^2)$ or at best as $O(N^{1.5})$ (where N is the total number of particles in the system), which is not sufficient for modern large scale computer simulations for carrying out simulations with number of particles of, say, of order 10^4 or beyond. This unfavourable scaling of the Ewald method makes it difficult to explore large systems and/or to compare with the experimental predictions. Therefore, several classes of alternative Ewald based fast algorithms have been proposed in order to reduce the computational complexity to a suitable level. Among those, the most popular is the particle mesh Ewald algorithm, which effectively calculates the reciprocal part of the Ewald sum by employing fast Fourier transforms (FFT), resulting in an algorithm of order of $N \ln N$ (Deserno and Holm, 1998a). However, this transition from the traditional Ewald method to the FFT based particle mesh Ewald method introduces additional governing parameters to this new class of algorithms which should be tuned in order to achieve the optimal computational cost for a desired accuracy.

The traditional Ewald sum is governed by three parameters, namely, the range of real space interactions or real space cut-off, the number of Fourier modes in the reciprocal space calculation or reciprocal space cut-off, and the Ewald splitting paramter, α, which decides how the load is to be distributed between the real space and reciprocal space calculation in order to perform the total sum. A naive

implementation of the Ewald sum leads to an algorithm of $O(N^2)$, either for the real space or for the reciprocal space summation, while the remaining sum scales as $O(N)$, so that the overall algorithm scales as $O(N^2)$. Notably, it is possible to achieve an algorithm of order $O(N^{1.5})$ (by balancing the computational load between the real and reciprocal space sum by choosing an optimal value of α), based on the optimization technique proposed by Kolafa and Perram (1992), and later by Fincham (1994). Until recently, all these implementations had been proposed in the context of electrostatic interactions. Jain et al. (2012b) adopted the same optimization technique in the context of hydrodynamic interactions, resulting in an algorithm of order $O(N^{1.5})$ for BD simulations of semi-dilute polymer solutions. They used the Rotne-Prager-Yamakawa tensor for treating hydrodynamic interactions for which the Ewald sum was first derived by Beenakker (1986). An alternative way to handle long ranged interactions is to employ fast Fourier transformations, which effectively calculates the reciprocal part of the Ewald sum with the computational expense of $N \ln N$ (Petersen, 1995). The central idea is to keep the computational cost of the real space sum to $O(N)$ by choosing a small value of the real space cut off, while attention is given to reducing the complexity of the reciprocal part of the Ewald sum, from $O(N)^2$ (for the traditional Ewald sum) and/or from $O(N)^{1.5}$ (for the optimized Ewald sum), to $N \ln N$ with the help of FFT.

FFT is a grid/mesh based method and hence, one has to place the charges (in the case of electrostatic interactions) and/or forces (in the case of hydrodynamic interactions) onto a regular three-dimensional grid of points in order to compute the Ewald sum. This has led to the development of a new class of algorithms which effectively perform the Fourier space sum with the computational cost of $N \ln N$, and these are collectively called particle mesh Ewald methods.

As pointed out above, a particle mesh Ewald method is a grid based method, and depending upon how the charges/forces are to be mapped onto the regular three dimensional grid of points, and how they compensate for the loss of accuracy

introduced due to this transformation, there are different algorithms available in the literature, e.g., particle mesh Ewald method (PME) (Darden et al., 1993), particle particle particle mesh Ewald method (PPPM or P3M) (Hockney et al., 1973; Hockney and Eastwood, 1988; Eastwood, 1975), and smooth particle mesh Ewald method (SPME) (Essmann et al., 1995). The first particle based Ewald method using FFT was the particle particle particle mesh Ewald method (P3M), introduced by Hockney et al. (1973). Darden et al. (1993) proposed the particle mesh Ewald method which uses a piecewise Lagrangian interpolation technique to map the charges onto the three dimensional regular mesh of points. Later on, Essmann et al. (1995) extended this method by smoothly interpolating the charges onto the grid points with the help of cardinal B-splines interpolation, which has since come to be known as the smooth particle mesh Ewald method. A brief comparison of different particle based methods for evaluating the Ewald sum has been clearly presented by Luty et al. (1994), and Deserno and Holm (1998a). It is also possible to convert one particle based method to another by simply tuning the lattice Green function, as discussed in Ballenegger et al. (2012). Besides these particle based mesh Ewald methods, some other alternative methods are also available for summing up long-ranged electrostatic interactions which avoid the Ewald sum, but achieve an order $O(N)$ algorithm, for example, the fast multiple method (FMM) by Greengard and Rokhlin (1987), the fast Poisson method (FPM) by York and Yang (1994), the Gaussian split method by Shan et al. (2005), and the recently proposed spectral Ewald method by Lindbo and Tornberg (Lindbo and Tornberg, 2011; Lindbo and Tornberg, 2012).

In contrast to the development of new methods for evaluating the Ewald sum, probably much less attention has been given to the development of the optimization techniques for tuning the governing parameters for the methods which are already available in the literature. Although, it is appropriate to say here that for the P3M algorithm, there are several studies available (Deserno and Holm, 1998b; Cerdà et al., 2011; Ballenegger et al., 2008) where an easy to follow optimization technique

has been proposed along with a simple analytical approximation for the error, so that one can precisely determine the optimal Ewald splitting parameter, which is a function of system specifications and P3M parameters. Similarly, for the PME method, Petersen (1995) proposed an optimization technique based on scaling arguments for the times taken by different steps involved in the method. Compared to these, to the best of our knowledge, there are very few studies available on developing a simple optimization technique for the SPME method. Recently, Wang et al. (2010) have provided error estimates for both the *ik*- and analytical differentiation schemes, based on the properties of Cardinal B-splines, however, they are restricted to only even interpolation orders. For a predetermined accuracy, it is possible to estimate the SPME parameters using their error estimates, prior to a simulation. More recently, Linse and Linse (2014) performed an investigation on the tuning of the governing parameters of the smooth particle mesh Ewald method in the context of simulations of ionic solutions and dipolar fluids. Based on the scaling dependence of execution time on the number of particles, their study displayed a scaling of $O(N \ln N)$ for the SPME sum, and of $O(N^{1.5})$ for the standard Ewald sum. For the systems under considerations in their studies, they showed that the SPME method is better in performance than the standard Ewald method, even at particle numbers of order 10^3, whereas it becomes 20 times faster than the latter at particle numbers of order 10^6.

Although these proposed methods are highly accurate, one can still ask if it is possible to develop an alternative and simpler optimization procedure, based on scaling arguments for the time taken by the different steps involved in the SPME method (similar to the arguments of Fincham (1994) in the context of the traditional Ewald sum or by Petersen (1995) in the context of the PME method. Our aim in this study is to achieve this goal in the context of both electrostatic and hydrodynamic interactions.

Long-ranged hydrodynamic interactions are commonly treated via the well known Oseen-Burgers (OB) tensor, which is a solution of the Stokes equation

in an unbounded domain (Bird et al., 1987b) or via the Rotne-Prager-Yamakawa tensor (Rotne and Prager, 1969; Yamakawa, 1970). Hasimoto (1959) applied the Ewald summation technique to the OB tensor in order to get the solution of the Stokes equation for flow past a periodic array of point forces. The main drawback associated with the OB tensor, which treats particles as point forces, is that there is a singularity at small inter particle separation distance. The RPY tensor regularizes the OB tensor in two ways. Firstly, it appropriately takes into account the finite particle radius by representing the far-field hydrodynamic interactions in a Taylor series expansion of the term $(a/\mathbf{r})$, where a is the particle radius, and $\mathbf{r}$ is the interparticle separation distance (Schmitz and Felderhof, 1982), and secondly, it regularizes the singularity that occurs at small interparticle separation distances, making the diffusion tensor always positive definite. Such a regularization is mandatory for BD simulations where configurations with overlapping particles are allowed. An excellent comparison of several models for treating hydrodynamic interactions has been presented by Knudsen et al. (2008). In the literature, there are some alternative techniques available which can also be used for treating near-field hydrodynamic interactions, without the need for regularization. For instance, in BD simulations, the problem of the formation of overlapping configurations can be avoided by introducing strong excluded volume interactions between the beads, thereby preventing beads from coming close together. The OB tensor can then be used for treating far field hydrodynamic interactions. Further, in the context of BD simulations of colloidal suspensions and fibre sedimentation, the near-field hydrodynamic interactions are treated via short range lubrication forces, whereas far-field hydrodynamic interactions are accounted for with the OB tensor (Saintillan et al., 2005). However, in order to be able to simulate all possible situations and configurations of particles, it is more suitable to use the RPY tensor in place of the OB tensor. For instance, for simulating semi-dilute polymer solutions under θ conditions using BD, where beads overlap will occur, (usually achieved by switching off excluded volume interactions), one has to use the

regularized RPY tensor, which allows the overlapping of beads.

Besides particle mesh Ewald methods, there are other techniques also available in the literature which efficiently achieve an order $N \ln N$ algorithm for evaluating long-ranged hydrodynamic interacting terms. For instance, Sierou and Brady (2001) proposed the accelerated Stokesian dynamics (ASD) which is a modification of the conventional Stokesian Dynamics method for calculating hydrodynamic interactions among non-Brownian particles suspended in a viscous fluid at small Reynolds numbers with an effective computational cost of $N \ln N$. On the other hand, Hernández-Ortiz et al. (2006) have developed a $N \ln N$ BD method for calculating hydrodynamic interactions in polymer systems confined between two parallel walls based on a Fourier series representation of the Stokeslet, which essentially satisfies the no-slip boundary condition at the walls. Lindbo and Tornberg (2010) have proposed a Spectral Ewald (SE) method for fast summation of periodic Stokes potentials, which they claim as being as accurate as the smooth particle mesh Ewald method. Also recently, Liang et al. (2013) implemented a fast multiple method for the RPY tensor, and applied it in their BD simulations. However, in the context of hydrodynamic interactions, the application of the particle mesh Ewald method for evaluating the Ewald sum is very limited. For instance, Saintillan et al. (2005) used the SPME technique in order to efficiently compute hydrodynamic interactions between the particles suspended in a Stokes suspension. It has been observed from their investigation that a speed factor of several orders of magnitude could be achieved for the SPME technique over the traditional Ewald sum, which is again a function of system size and the specified error tolerance. Along similar this, very recently Crosby and Lister (2013) have used Saintillan *et al.*'s SPME technique for evaluating the reciprocal space part of the Ewald sum for the OB tensor, while studying the viscous sedimentation of a suspension consisting of monodisperse point particles in a vertically sheared periodic system. The implementation of the SPME technique for the RPY tensor

has also recently been carried out by Saadat and Khomami (2015a) in the context of Brownian dynamics simulations of dilute and semidilute polymer solutions. Although their matrix free approach successfully achieves an algorithm of order $N \ln N$, they have not discussed the optimization of parameters associated with the SPME method in order to obtain the minimal computational cost.

In summary, this study contributes two aspects to the problem of carrying out pair-wise sums over long-ranged interactions: (i) we implement the smooth particle mesh Ewald method for the Rotne-Prager-Yamakawa tensor, which allows for rapid simulation of polymer solutions and colloidal suspensions at finite concentrations, (ii) we propose a relatively simple to follow and easy to implement optimization technique for the SPME method in the context of both electrostatic and hydrodynamic interactions.

This chapter is organized is as follows: In Section 3.2, we present the governing equations for the hydrodynamic and electrostatic interactions along with the smooth particle mesh Ewald method for evaluating the structure factor. In Section 3.3, we propose an optimization technique based on scaling arguments for the computational costs involved with the various steps of the SPME method. In Section 3.4, we present the main result, and in Section 3.5, we summarize the key findings of our present work.

3.2   Governing equations

We treat the governing equations for hydrodynamic interactions first, before discussing those for electrostatic interactions.

3.2.1   Hydrodynamic interactions

Let us consider N point particles initially enclosed in a cubic shaped simulation box of edge length L, and of volume, $V = L^3$, giving a bulk concentration of $c = N/V$. The forces, $\mathbf{F}_1, \mathbf{F}_2, ..., \mathbf{F}_N$, on the particles residing at positions, $\mathbf{r}_1, \mathbf{r}_2, ..., \mathbf{r}_N$, act

in such a way that the total force on all the particles in the main simulation box vanishes, i.e., $\sum_{\mu=1}^{N} \mathbf{F}_\mu = 0$. The simulation box in real space is described by the vectors $\mathbf{a}_\alpha$, while the corresponding conjugate reciprocal vectors $\mathbf{a}_\beta^*$ are defined in reciprocal space by the relation $\mathbf{a}_\alpha \cdot \mathbf{a}_\beta^* = 2\pi\delta_{\alpha\beta}$ (Kronecker delta), $(\alpha, \beta = 1, 2, 3)$. For the simulations, $L = |\mathbf{a}_1| = |\mathbf{a}_2| = |\mathbf{a}_3|$. We impose periodic boundary conditions (PBCs) in order to capture the long-ranged interactions. Therefore, a particle residing in the main simulation box at position $\mathbf{r}$ will interact with all other particles in the main simulation box, and their periodic images, and also with its own periodic images at $\mathbf{r} + \mathbf{n}L$, where $\mathbf{n} = (n_1, n_2, n_3)$ is the lattice vector with n_1, n_2, n_3 being integer numbers. Under these circumstances, Beenakker's representation of the sum $\sum_\mu \mathbf{D}_{\nu\mu} \cdot \mathbf{F}_\mu$ (which appears in the Ito stochastic differential equation(Eq. 2.1) given in Chapter 2) as an Ewald sum, using the RPY tensor in order to treat the hydrodynamic interactions, has the following form (Beenakker, 1986)

$$\sum_{\mu=1}^{N} \mathbf{D}_{\mu\nu} \cdot \mathbf{F}_\mu = \left(1 - \frac{6a\alpha}{\sqrt{\pi}} + \frac{40a^3\alpha^3}{3\sqrt{\pi}}\right)\mathbf{F}_\nu + \sum_{\mathbf{n}'}\sum_{\mu=1}^{N} \mathbf{M}^{(1)}(\mathbf{r}_{\nu\mu,\boldsymbol{n}}) \cdot \mathbf{F}_\mu$$
$$+ \sum_{\mathbf{k}\neq 0} \mathbf{M}^{(2)}(\mathbf{k}) \cdot \left[\cos(\mathbf{k}\cdot\mathbf{r}_\nu)\sum_{\mu=1}^{N}\cos(\mathbf{k}\cdot\mathbf{r}_\mu)\mathbf{F}_\mu\right]$$
$$- \sum_{\mathbf{k}\neq 0} \mathbf{M}^{(2)}(\mathbf{k}) \cdot \left[\sin(\mathbf{k}\cdot\mathbf{r}_\nu)\sum_{\mu=1}^{N}\sin(\mathbf{k}\cdot\mathbf{r}_\mu)\mathbf{F}_\mu\right] \qquad (3.1)$$

In the above equation, the non-dimensional diffusion tensor $\mathbf{D}_{\nu\mu}$ is a 3×3 square matrix for a fixed pair of particles μ and ν, which is related to the dimensionless hydrodynamic interaction tensor, $\boldsymbol{\Omega}$, by the Eq. 2.2 given in Chapter 2. In Eq. 3.1, the first term in the RHS is a correction term due to self interactions which does not involve any summation, whereas the second and third terms representing two sums, both of which converge exponentially fast, are carried out in real and reciprocal space, respectively. The parameter α, known as the Ewald splitting parameter, decides about how the computational load is to be distributed between the real

and reciprocal space sums. The distance vector $\mathbf{r}_{\nu\mu,\mathbf{n}}$ is defined by the relation $\mathbf{r}_{\nu\mu,\mathbf{n}} = \mathbf{r}_\nu - \mathbf{r}_\mu + \mathbf{n}L$, with $\mathbf{n} = 0$ corresponding to the main simulation box. The first summation in the RHS of the Eq. (3.1), i.e. the real space sum, is carried out in the main simulation box, and over all its periodic images surrounding it. The prime over $\mathbf{n}$ indicates that the terms with $\nu = \mu$ are omitted in the main simulation box with $\mathbf{n} = 0$. On the other hand, the second summation in Eq. (3.1), i.e., the reciprocal space sum, is performed over the lattice vectors $\mathbf{k} = 2\pi\mathbf{n}/L$ in the reciprocal space. $\mathbf{M}^{(1)}(\mathbf{r})$ is a 3×3 matrix in real space which depends on the particle radius, a, and the Ewald splitting parameter, α, whereas $\mathbf{M}^{(2)}(\mathbf{k})$ is a 3×3 matrix in the reciprocal space which again depends on a and α in addition to the volume of the simulation box. The expressions for $\mathbf{M}^{(1)}(\mathbf{r})$ and $\mathbf{M}^{(2)}(\mathbf{k})$ are as follows:

$$
\begin{aligned}
\mathbf{M}^{(1)}(\mathbf{r}) =& \operatorname{erfc}(\alpha r) \left(\frac{3a}{4r} + \frac{a^3}{2r^3} \right) \\
&+ \frac{\exp(-\alpha^2 r^2)}{\sqrt{\pi}} \left(3a\alpha^3 r^2 - \frac{9a\alpha}{2} + 4a^3\alpha^7 r^4 - 20a^3\alpha^5 r^2 + 14a^3\alpha^3 + \frac{a^3\alpha}{r^2} \right) \boldsymbol{\delta} \\
&+ \operatorname{erfc}(\alpha r) \left(\frac{3a}{4r} - \frac{3a^3}{2r^3} \right) \\
&+ \frac{\exp(-\alpha^2 r^2)}{\sqrt{\pi}} \left(\frac{3a\alpha}{2} - 3a\alpha^3 r^2 - 4a^3\alpha^7 r^4 + 20a^3\alpha^5 r^2 - 2a^3\alpha^3 - \frac{3a^3\alpha}{r^2} \right) \hat{\mathbf{r}}\hat{\mathbf{r}}
\end{aligned}
$$
$$(3.2)$$

where erfc is a complementary error function, and

$$
\mathbf{M}^{(2)}(\mathbf{k}) = \left(a - \frac{a^3 k^2}{3} \right) \left(1 + \frac{k^2}{4\alpha^2} + \frac{k^4}{8\alpha^4} \right) \left(\frac{6\pi}{k^2 V} \right) \exp\left(\frac{-k^2}{4\alpha^2} \right) (\boldsymbol{\delta} - \hat{\mathbf{k}}\hat{\mathbf{k}}) \quad (3.3)
$$

In Eqs. (3.2) and (3.3), r and $\hat{\mathbf{r}}$ are the magnitude and unit vector respectively of the vector $\mathbf{r}$ in real space, whereas k and $\hat{\mathbf{k}}$ are the magnitude and unit vector respectively corresponding to the vector $\mathbf{k}$ in reciprocal space. As pointed out earlier, for the evaluation of $\sum_\mu \mathbf{D}_{\mu\nu} \cdot \mathbf{F}_\mu$ with help of the SPME method, while the real space sum is again tackled with the same technique as in the traditional Ewald sum, the Fourier space sum is treated differently. The central idea is to

maintain the real space sum as $O(N)$ (by choosing a small cut-off radius) while effort is made to reduce the computational complexity of the Fourier space from $O(N^2)$ to $N \ln N$, so that the overall algorithm scales as $N \ln N$. Keeping this in mind, we concentrate only on the Fourier space sum defined in Eq. 3.1, which is rewritten as below

$$
\begin{aligned}
\left(\sum_\mu \mathbf{D}_{\mu\nu} \cdot \mathbf{F}_\mu \right)_{\text{Fourier sum}} &= \\
&\sum_{\mathbf{k} \neq 0} \mathbf{M}^{(2)}(\mathbf{k}) \cdot \left[\cos(\mathbf{k} \cdot \mathbf{r}_\nu) \sum_{\mu=1}^N \cos(\mathbf{k} \cdot \mathbf{r}_\mu) \mathbf{F}_\mu \right] \\
&- \sum_{\mathbf{k} \neq 0} \mathbf{M}^{(2)}(\mathbf{k}) \cdot \left[\sin(\mathbf{k} \cdot \mathbf{r}_\nu) \sum_{\mu=1}^N \sin(\mathbf{k} \cdot \mathbf{r}_\mu) \mathbf{F}_\mu \right] \\
&= \sum_{\mathbf{k} \neq 0} \mathbf{M}^{(2)}(\mathbf{k}) \cdot \left[\sum_{\mu=1}^N \mathbf{F}_\mu \cos \mathbf{k} \cdot (\mathbf{r}_\mu - \mathbf{r}_\nu) \right]
\end{aligned}
\tag{3.4}
$$

The above equation can be recast using Euler's identity as follows

$$
\left(\sum_\mu \mathbf{D}_{\mu\nu} \cdot \mathbf{F}_\mu \right)_{\text{Fourier sum}} = \sum_{\mathbf{k} \neq 0} \mathbf{M}^{(2)}(\mathbf{k}) \cdot e^{-2\pi i \mathbf{k} \cdot \mathbf{r}_\nu} \mathbf{S}^{\text{HI}}(\mathbf{k})
\tag{3.5}
$$

where $\mathbf{S}^{\text{HI}}(\mathbf{k})$ is called the structure factor defined (in non-dimensional form) by

$$
\mathbf{S}^{\text{HI}}(\mathbf{k}) = \sum_{\mu=1}^N \mathbf{F}_\mu e^{2\pi i \mathbf{k} \cdot \mathbf{r}_\mu}
\tag{3.6}
$$

3.2.2   Electrostatic interactions

Let us consider N discrete point charges, $q_1, q_2, ..., q_N$, which are randomly placed in a cubic shaped simulation box of side length L and of volume $V = L^3$. The charges, $q_1, q_2, ..., q_N$, at positions, $\mathbf{r}_1, \mathbf{r}_2, ..., \mathbf{r}_N$, satisfy the condition, $q_1 + q_2 + ... + q_N = 0$, within the unit cell, i.e., the simulation cell is charge neutral. The simulation box in real space is described by the vectors $\mathbf{a}_\alpha$, while the corresponding conjugate reciprocal vectors $\mathbf{a}_\beta^*$ are defined in reciprocal space by the relation as $\mathbf{a}_\alpha \cdot \mathbf{a}_\beta^* = 2\pi \delta_{\alpha\beta}$ (Kronecker delta), $(\alpha, \beta = 1, 2, 3)$. Furthermore, in order

to capture the long-ranged electrostatic interactions, again we impose periodic boundary conditions (PBCs), so that the main simulation box contains infinite periodic images of itself in all three directions, designated by $\mathbf{n}$ (n_1, n_2, n_3), where n_1, n_2, n_3 are all integers which tend to infinity, and $\mathbf{n} = 0$ corresponds to the main simulation box. Therefore, a point change, q_μ residing at $\mathbf{r}_\mu$, in the main simulation box will interact with all other charges, q_ν, such that $\mu \neq \nu$, as well as with all of their periodic images at positions $\mathbf{r}_\nu + n_1\mathbf{a}_1 + n_2\mathbf{a}_2 + n_3\mathbf{a}_3$, and also its own periodic images at positions $\mathbf{r}_\mu + n_1\mathbf{a}_1 + n_2\mathbf{a}_2 + n_3\mathbf{a}_3$ according to Coulomb's law. Under these circumstances, the total electrostatic energy of the unit cell can be written in non-dimensional form as follows:

$$E = \frac{1}{2} \sum_{\mathbf{n}'} \sum_\mu \sum_\nu \frac{q_\mu q_\nu}{|\mathbf{r}_\mu - \mathbf{r}_\nu + \mathbf{n}|} \tag{3.7}$$

In the above equation, the prime over $\mathbf{n}$ indicates that the terms with $\mu = \nu$ and $\mathbf{n} = 0$ are not included. From the expression of the sum in Eq. (3.7), it can be seen that it decays as the inverse of the distance. It can also be shown that the sum is only conditionally convergent. Ewald transformed this slowly and conditionally converging sum into two sums, namely, a direct sum in real space, and a reciprocal sum in Fourier space, both converging exponentially fast, and a correction term, respectively, as follows (Ewald, 1921):

$$E_{\text{real}} = \frac{1}{2} \sum_{\mathbf{n}'} \sum_{\mu,\nu=1}^{N} \frac{q_\mu q_\nu \, \text{ercf}\,(\alpha|\boldsymbol{r}_\nu - \mathbf{r}_\mu + \mathbf{n}|)}{|\mathbf{r}_\nu - \mathbf{r}_\mu + \mathbf{n}|} \tag{3.8}$$

$$E_{\text{reci}} = \frac{1}{2\pi V} \sum_{\mathbf{k}\neq 0} \frac{\exp\,(-\pi^2 \mathbf{k}^2/\alpha^2)}{\mathbf{k}^2} \mathbf{S}^{\text{ES}}(\mathbf{k})\mathbf{S}^{\text{ES}}(-\mathbf{k}) \tag{3.9}$$

$$E_{\text{corr}} = -\frac{1}{2} \sum_{(\mu,\nu)\in M} \frac{q_\mu q_\nu \, \text{erf}\,(\alpha|\mathbf{r}_\mu - \mathbf{r}_\nu|)}{|\mathbf{r}_\mu - \mathbf{r}_\nu|} - \frac{\alpha}{\sqrt{\pi}} \sum_{\mu=1}^{N} q_\mu^2 \tag{3.10}$$

where, prime over $\mathbf{n}$ in Eq. (3.8) again indicates that terms with $\mathbf{n} = 0$ and $\mu = \nu$ are omitted from the summation. In Eq. (3.9), $V = \mathbf{a}_1 \cdot \mathbf{a}_2 \times \mathbf{a}_3$, is the volume of the simulation box in the reciprocal space, and $\mathbf{k}$ are the reciprocal lattice vectors

defined by, $\mathbf{k} = k_1 \mathbf{a}_1^* + k_2 \mathbf{a}_2^* + k_3 \mathbf{a}_3^*$, where k_1, k_2 and k_3 are all integers. Based on these reciprocal lattice vectors, the structure factor, $\mathbf{S}^{\mathrm{ES}}(\mathbf{k})$, defined in Eq. (3.9), is given as follows:

$$\mathbf{S}^{\mathrm{ES}}(\mathbf{k}) = \sum_{\mu=1}^{N} q_\mu e^{2\pi i \mathbf{k} \cdot \mathbf{r}_\mu} \qquad (3.11)$$

The force $\mathbf{F}_\mu$ on particle μ can then be calculated by differentiating the total energy, $E(\mathbf{r}_1, ..., \mathbf{r}_N) = E_{\mathrm{real}} + E_{\mathrm{reci}} + E_{\mathrm{corr}}$, with respect to the corresponding particle position, $\mathbf{r}_\mu$, which implies $\mathbf{F}_\mu = -\frac{\partial E}{\partial \mathbf{r}_\mu} = -\left[\frac{\partial E_{\mathrm{real}}}{\partial \mathbf{r}_\mu} + \frac{\partial E_{\mathrm{reaci}}}{\partial \mathbf{r}_\mu} + \frac{\partial E_{\mathrm{corr}}}{\partial \mathbf{r}_\mu} \right]$.

3.2.3 Approximation of the reciprocal space sum in the context of hydrodnamic interactions

It can be clearly seen that the reciprocal part of the Ewald sum for both the hydrodynamic (HI) and electrostatic interactions (ES) contains the structure factor defined by Eq. (3.6) for HI, and by Eq. (3.11) for ES. The presence of structure factor enables the use of FFT. As the point forces/charges can be located at arbitrary locations in the main simulation box, prior interpolation is necessary onto the three dimensional Cartesian grid points in order to apply the FFT algorithm. In case of the SPME method, this is achieved using Cardinal B-splines. In the context of electrostatic interactions, the calculation of the structure factor using Cardinal B-splines has been discussed comprehensively by Essmann et al. (1995) and others (Ballenegger et al., 2012; Wang et al., 2010), and is consequently not repeated here. Only the final expressions used for the present study are presented in Appendix A. In this section, we focus on deriving the sturcture factor in the context of hydrodynamic interactions using the SPME technique. At the onset of the derivation, a three dimensional grid is defined inside the reciprocal unit cell by introducing three positive integers $K_1, K_2,$ and K_3 corresponding to the total number of grid points along the reciprocal lattice vectors $\mathbf{a}_1^*, \mathbf{a}_2^*,$ and $\mathbf{a}_3^*$. If $\mathbf{r}_\mu$ is any particle position inside the unit cell, then we redefine its fractional co-ordinates by $\xi_{\mu i} = K_i r_{\mu i} / L$, where K_i is the total number of mesh points in the direction i,

and this results in $0 \leq \xi_i \leq K_i$. Now, we wish to approximate the structure factor defined in Eq. 3.6 onto the discrete grid points as formed above. This problem has a particular solution based on the properties of exponential Euler splines (Schoenberg, 1973; Chui, 2014) which particularly makes the SPME method distinguishable from other particle mesh Ewald methods. In the new fractional co-ordinate system, the exponential terms in the structure factor become:

$$\exp(2\pi i \mathbf{k} \cdot \mathbf{r}_\mu) = \exp\left(2\pi i k_1 \frac{\xi_{\mu 1}}{K_1}\right) \exp\left(2\pi i k_2 \frac{\xi_{\mu 2}}{K_2}\right) \exp\left(2\pi i k_3 \frac{\xi_{\mu 3}}{K_3}\right) \qquad (3.12)$$

Now, we can approximate the one-dimensional function $\exp\left(2\pi i k_i \frac{\xi_{\mu i}}{K_i}\right)$ by a piecewise interpolation technique based on the properties of Cardinal B-splines as follows:

$$\exp\left(2\pi i k_i \frac{\xi_{\mu i}}{K_i}\right) \approx b_\mu(k_{\mu i}) \sum_{m=-\infty}^{+\infty} M_p(\xi_{\mu i} - m) \cdot \exp\left(2\pi i \frac{k_i}{K_i} m\right) \qquad (3.13)$$

where

$$b_\mu(k_{\mu i}) = \exp\left[2\pi i (p-1) \frac{k_{\mu i}}{K_i}\right] \times \left[\sum_{k=0}^{p-2} M_p(k+1) \exp\left(2\pi i k_{\mu i} \frac{k}{K_i}\right)\right]^{-1} \qquad (3.14)$$

where $M_p(u)$ are cardinal B-splines with p^{th} order of interpolation. For any real number, $M_p(u)$ is nothing but a hat function,

$$M_p(u) = \begin{cases} 1 - |u - 1|, & 0 \leq u \leq 2 \\ 0, & \text{otherwise.} \end{cases} \qquad (3.15)$$

Higher order splines are obtained from a recursive definition as given by:

$$M_p(u) = \frac{u}{u-1} M_{p-1}(u) - \frac{p-u}{p-1} M_{p-1}(u-1), \quad \text{for } p > 2 \qquad (3.16)$$

The big advantage of using Cardinal B-spline is that the bases are $p - 2$ times continuously differentiable and the support of the splines $M_p(u)$ is a bounded set:

$u \in [0, p]$. Therefore, the evaluation of the exponential function is purely a local operation. The structure factor, $\mathbf{S}^{\text{HI}}(\mathbf{k})$, is then approximated as follows:

$$\mathbf{S}^{\text{HI}}(\mathbf{k}) \approx \tilde{\mathbf{S}}^{\text{HI}}(\mathbf{k}) \approx b_1(k_1)b_2(k_2)b_3(k_3)\mathcal{F}(Q)(k_1, k_2, k_3) \tag{3.17}$$

where $\mathcal{F}(Q)$ is the three-dimensional discrete Fourier transform of the matrix array $Q(\mathbf{k})$ of dimension $K_1 \times K_2 \times K_3$ given by the following expression:

$$Q(k_1, k_2, k_3) = \sum_{\mu=1}^{N} \sum_{p_1,p_2,p_3} \mathbf{F}_\mu M_p(\xi_1^\mu - k_1 - p_1 K_1) M_p(\xi_2^\mu - k_2 - p_2 K_2) M_p(\xi_3^\mu - k_3 - p_3 K_3)$$

$$\tag{3.18}$$

Therefore, the reciprocal part of the Ewald sum can be written in approximate form as follows:

$$\left(\sum_{\mu=1}^{N} \mathbf{D}_{\mu\nu} \cdot \mathbf{F}_\mu \right)_{\text{Fourier sum}} = \sum_{\mathbf{k} \neq \mathbf{0}} \mathbf{M}^{(2)}(\mathbf{k}) \cdot B(k_1, k_2, k_3) \mathcal{F}(Q)(k_1, k_2, k_3)$$

$$\mathcal{F}(Q)(-k_1, -k_2, -k_3)$$

$$= \frac{1}{2} \sum_{k_1=0}^{K_1-1} \sum_{k_2=0}^{K_2-1} \sum_{k_3=0}^{K_3-1} Q(k_1, k_2, k_3) \cdot (\theta_{\text{rec}} \star Q)(k_1, k_2, k_3)$$

$$\tag{3.19}$$

where the array B is given by the following expression:

$$B(k_1, k_2, k_3) = \Pi_{i=1}^{3} |b_i(k_i)|^2$$

$$= |b_1(k_1)|^2 \cdot |b_2(k_2)|^2 \cdot |b_3(k_3)|^2 \tag{3.20}$$

and the pair potential θ_{rec} is given by $\theta_{rec} = F(B \cdot C)$. Here the operator $\star$ denotes the convolution between θ_{rec} and Q, and the array C is simply the $\mathbf{M}^{(2)}(\mathbf{k})$ matrix. Therefore, the overall algorithm for evaluating the Fourier space sum using the SPME technique can now be summarized as follows. The first step is the assignment of the point forces $\mathbf{F}_\mu$ onto the three dimensional grid points using cardinal B-splines, i.e., the calculation of the array $Q(k_1, k_2, k_3)$ using the

interpolation formula of Eq. 3.18 (Step 1). The discrete Fourier transform $\mathcal{F}(Q)$ is then computed using the fast Fourier transforms algorithm (FFT), which is in turn multiplied by the B array for getting the structure factor defined in Eq. 3.17 (Step 2). The result is then multiplied by the C array (i.e., $\mathbf{M}^{(2)}(\mathbf{k})$ matrix), and then an inverse FFT is applied to yield the Fourier space sum at the grid points defined by Eq. 3.19 (Step 3). At last, the sum can then be interpolated back from the grid points to the original particle positions, again using the same assignment function which has been used for the force assignment onto the three dimensional grid points as defined in Eq. 3.18 (Step 4).

3.3   Optimization procedure

The optimization of the traditional Ewald sum in the context of electrostatic interactions has been carried by Kolafa and Perram (1992), followed by Fincham (1994). Jain et al. (2012b) successfully implemented the same optimization technique in the context of hydrodynamic interactions. As pointed out earlier, a similar optimization technique is not available for the SPME method, based on scaling arguments for the time taken by the different steps involved both in the context of electrostatic and hydrodynamic interactions. Our aim is to achieve this goal for BD simulations using the SPME method. It is appropriate to note here that the optimization procedure will be identical for electrostatic and hydrodynamic interactions. The discussion is consequently presented in a general form. Further, the real space error can be calculated by exactly the same procedure as was used for the optimized Ewald sum by Fincham (1994) and Jain et al. (2012b), since the SPME scheme is only concerned with the Fourier space sum.

3.3.1   Error estimation

If the bulk concentration in the cubic unit cell is c (the total number of particles, N, per unit volume, $V = L^3$), then the length of the simulation box, L, is given

by $L = (N/c)^{1/3}$. Therefore, it can be easily seen that at fixed concentration c, the box size increases as $N^{1/3}$.

Real space error

The convergence of the real space sum depends on the complementary error function $\mathrm{erfc}(\alpha r)$, where r is the distance between a pair of particles and/or forces. In practice, this real space sum is evaluated only for $r \leq r_c$, where r_c is the cut-off radius. The value of the splitting parameter, α, is chosen in such a way that the term $\mathrm{erfc}(\alpha r_c)$ becomes small. At large values of αr_c, the term $\mathrm{erfc}(\alpha r_c)$ behaves like $\exp(-\alpha^2 r_c^2)$. If we specify M as an accuracy parameter such that $\exp(-M^2)$ is very small, then for a desired accuracy, M, and a given cut-off radius, r_c, the value of α is simply the ratio between these two, which means,

$$\alpha^2 r_c^2 = M^2 \quad \text{or} \quad \alpha = M/r_c \tag{3.21}$$

Fourier space error

At the outset, it is reasonable to assume that to get the same accuracy, M, the error tolerance, say ϵ, should be of the same order for both the real and reciprocal space sums (Essmann et al., 1995), i.e.,

$$\epsilon_{\mathrm{real}} \sim \epsilon_{\mathrm{reci}} = \exp(-M^2) \tag{3.22}$$

From the preceding discussion, it is clear that the error in the reciprocal space sum is different for the SPME method compared to the standard Ewald method where, error is introduced due to the use of a limited number of Fourier modes in reciprocal space. In the context of the SPME method, while the same error occurs due to the use of a limited number of grid points, K_{mesh} (the number of mesh points in one direction, $K_1 = K_2 = K_3 = K_{\mathrm{mesh}}$) in the cubic unit call, additional error is introduced due to the interpolation of the random forces onto

three dimensional mesh points. It has been shown that the error introduced in the first case is small in comparison to the error introduced in the latter process (Wang et al., 2010). Therefore, the error in reciprocal space can be estimated to be,

$$\epsilon_{\text{reci}} \propto (\Delta x)^p = C_1(\Delta x)^p, \quad \text{where} \quad (\Delta x) = L/K_{\text{mesh}} \qquad (3.23)$$

In the above equation, C_1 is a proportionality constant. One can show that the error in the standard Ewald method is of $O(1)$ when $\Delta x \sim \frac{1}{\alpha}$ (Jain et al., 2012b). This gives us an estimate of the upper bound on Δx. As a result, in order to ensure that the interpolation error is never greater than $O(1)$, we must choose $C_1 \propto \alpha^p$. As a result,

$$\epsilon_{\text{reci}} \propto (\alpha \Delta x)^p \qquad (3.24)$$

Setting the interpolation error equal to the error tolerance e^{-M^2}, and using the expression for Δx, we get,

$$\left(\frac{\alpha L}{K_{\text{mesh}}} \right)^p = \exp\left(-M^2 \right) \qquad (3.25)$$

3.3.2   Scaling arguments

The main idea behind Fincham's (Fincham, 1994) optimization procedure for the traditional Ewald sum was to minimize the total CPU time with respect to the splitting parameter, α, and the real space cut-off, r_c, in the context of the electrostatic interactions. Subsequently, a similar argument was made in the context of hydrodynamic interactions by Jain et al. (2012b). For the present SPME method, we adopt a similar procedure, but now we minimize the total CPU time with respect to the Ewald splitting parameter (α) and the order of interpolation (p). In order to achieve this, we need to calculate the CPU time required for every step separately, which is subsequently discussed in detail below.

Real space time

The number density of the particles is chosen in such a way that the distribution of particles is homogeneous in the main simulation box. Then, the total number of particles residing inside the sphere of cut-off radius, r_c, is $\frac{4\pi}{3}r_c^3 c$, where c is the bulk concentration of the particles. If t_{real} is the execution time for one interaction (between two particles) in real space, then the total real space execution time T_{real} for one time step is

$$T_{\text{real}} = \left(\frac{4\pi}{3}r_c^3\right) N c\, t_{\text{real}} \tag{3.26}$$

where N is the total number of particles in the main simulation box. Of course, this is the same expression as was derived by Fincham (1994) in the context of the electrostatic interactions, and as used by Jain et al. (2012b) in the context of the hydrodynamic interactions.

Interpolation time

This is the time required to interpolate the random forces and/or charges, residing in the main simulation box, onto the three dimensional mesh points. If Cardinal B-splines of order M_p, are used for interpolation, then every force needs to be distributed three dimensionally onto a total of p^3 mesh points, where p is the total number of sites in one direction. If t_{in} is the execution time for interpolating one force to one site, then the total interpolation execution time, T_{in}, for distributing N forces, each to p^3 sites, is given as (Wang et al., 2010; Petersen, 1995)

$$T_{\text{in}} = N p^3 t_{\text{in}} \tag{3.27}$$

Fast Fourier transforms time

The *FFTW package* has been used for the fast Fourier transform calculations. The CPU time for this calculation scales as $K \ln K$, where $K = K_{\text{mesh}}^3$ (Petersen, 1995; Wang et al., 2010). If the total CPU time for this calculation is T_{fft}, then it is

given as

$$T_{\text{fft}} = K \ln K \; t_{\text{fft}} \tag{3.28}$$

where t_{fft} is the pre-factor in the time needed to perform the fast Fourier transforms. It should be noted that the values of t_{real}, t_{in} and t_{fft} depend on machine architecture. In the present instance, all these paramters are estimated on an IBM iDataplex x86 system (Merri) housed at the Victorian Life Sciences Computation Initiative (VLSCI) in the University of Melbourne.

3.3.3   Minimization of the total CPU time

In this section, we wish to optimize the total CPU time, T_{CPU}, at a fixed accuracy parameter, M. The total CPU time, T_{CPU}, for one time step is the combination of T_{real}, T_{in} and T_{fft}, i.e. ,

$$T_{\text{CPU}} = T_{\text{real}} + T_{\text{in}} + T_{\text{fft}} \tag{3.29}$$

On substituting the expressions for T_{real} (Eq. 3.26), T_{in} (Eq. 3.27), and T_{fft} (Eq. 3.28), we get

$$T_{\text{CPU}} = \left(\frac{4\pi}{3} r_c^3 \right) N c \, t_{\text{real}} + N p^3 t_{\text{in}} + K \ln K \; t_{\text{fft}} \tag{3.30}$$

Replacing r_c by M/α (from Eq. 3.21), and K by $\left[\alpha L \exp\left(\frac{M^2}{p} \right) \right]^3$ (from Eq. 3.25) in the above equation, we obtain an expression which is now a function of α and p. Therefore, in order to find the minimum CPU time, we need to solve the set of equations, $\frac{\partial T_{\text{CPU}}}{\partial \alpha} = 0$; $\frac{\partial T_{\text{CPU}}}{\partial p} = 0$. These lead to the following two coupled non-linear equations, which need to be solved simultaneously in order to get the optimum values of α and p,

$$-\frac{4}{\alpha^4} \pi M^3 c N t_{\text{real}} + 3 L^3 \alpha^2 \exp\left(\frac{3M^2}{p} \right) \left[1 + \ln\left((\alpha L)^3 \exp\left(\frac{3M^2}{p} \right) \right) \right] t_{\text{fft}} = 0 \tag{3.31}$$

and

$$3Np^2 t_{\text{in}} + (L\alpha)^3 \left(\frac{3M^2}{p^2}\right) \exp\left(\frac{3M^2}{p}\right) \left[1 + \ln\left((\alpha L)^3 \exp\left(\frac{3M^2}{p}\right)\right)\right] t_{\text{fft}} = 0$$

(3.32)

Note that we treat p as a continuous variable in these expressions. Once the optimal values of α and p are obtained, the total number of mesh points K_{mesh} in a direction can be calculated using Eq. 3.25.

3.4 Results and discussion

3.4.1 Evaluation of t_{real}, t_{in} and t_{fft}

The aim of the present optimization procedure is to minimize the total execution time, which is a combination of the real space execution time (T_{real}), the interpolation execution time (T_{in}), and the FFT execution time (T_{fft}), for both hydrodynamic ($T_{\text{CPU}}^{\text{HI}}$) and electrostatic ($T_{\text{CPU}}^{\text{ES}}$) interactions, with respect to the order of interpolation p and Ewald splitting parameter α. Therefore, the first step in the present optimization procedure is the determination of the scaling parameters, namely, t_{real}, t_{in} and t_{fft} for both the long-ranged interactions. The real space execution time t_{real} is evaluated using the Eq. 3.26. Numerical data are obtained by running simulations for various combinations of the real space cut-off and concentration at different values of the total number of particles, N. For each combination of r_c, c and N, the data is acquired by running 100 independent trajectories. Figs. 3.1 and 3.2 show the representative plots for hydrodynamic and electrostatic interactions, respectively. The figues in the inset show the results for all combinations of r_c and c along with the upper and lower limit of standard deviations at different values of N, whereas the main figures show the mean value with the upper limit of error being the highest value of the standard deviation amongst all combinations of r_c and c, and the lower limit being the lowest value at a particular value of N. Performing a least squares regression analysis fitting
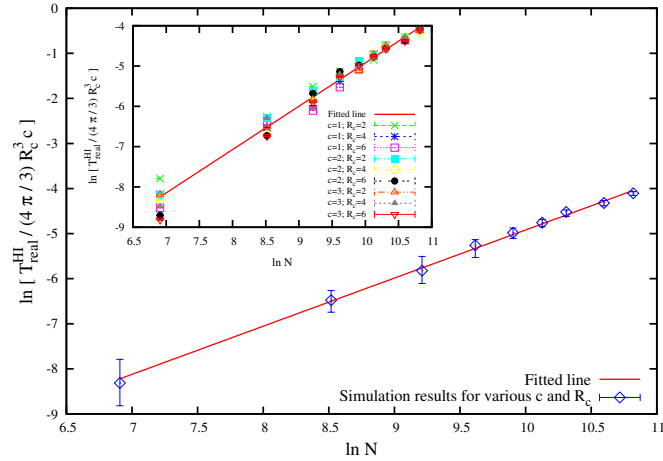
FIGURE 3.1: Real space execution time calculation for hydrodynamic interactions
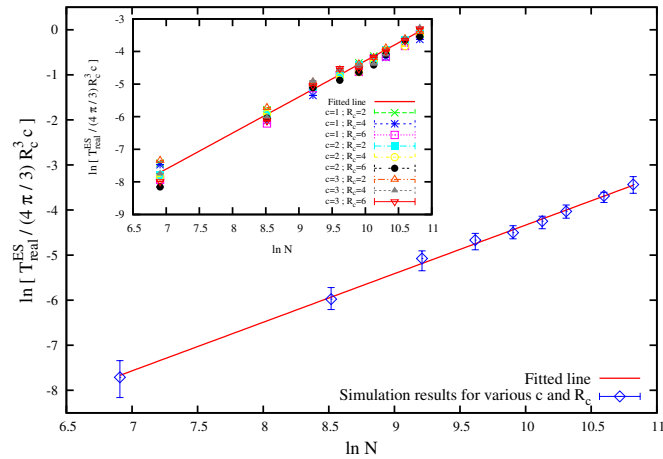
FIGURE 3.2: Real space exexution time calculation for electrostatic interactions

of all the data according to Eq. 3.26, the values of $t_{\text{real}}^{\text{HI}}$ and $t_{\text{real}}^{\text{ES}}$ are evaluated to be $1.55 \times 10^{-7} \pm 3.52 \times 10^{-8}$ (s) and $2.73 \times 10^{-7} \pm 1.26 \times 10^{-8}$ (s) for HI and ES respectively. Here two points are worth noting. Firstly, it can be seen that the total real space execution time T_{real} is independent of the values of the real space cut-off, r_c, and concentration, c, once it is divided by the factor $(4\pi/3)r_c^3 c$, which demonstrates the validity of the scaling argument proposed for evaluating the real space time (Eq. 3.26). Secondly, it can be seen that the equation can be used for evaluating the term t_{real} for these type of long-ranged interactions. Furthermore, it should be mentioned here that none of the parameters, say, the accuracy parameter, (M), Ewald splitting parameter, (α), order of interpolation (p) or number of

mesh points (K_{mesh}) have any influence on the value of t_{real}.

Next, we turn our attention for calculating the interpolation execution time, t_{in}, for which the governing equation is Eq. 3.27. In order to do this, the value of order of interpolation, p, has been chosen to be $6, 9$ and 12, for each value of N, which ranges from 1000 to 40000 for both HI and ES interactions. The results are presented in Figs. 3.3a and 3.3b for HI and ES interactions, respectively. After carrying out a linear least squares regression fitting analysis spanning all the data, the values of t_{in} are evaluated to be $4.5 \times 10^{-8} \pm 2.05 \times 10^{-10}$ (s) and $1.41 \times 10^{-8} \pm 9.73 \times 10^{-11}$ (s) for HI and ES interactions, respectively. From this
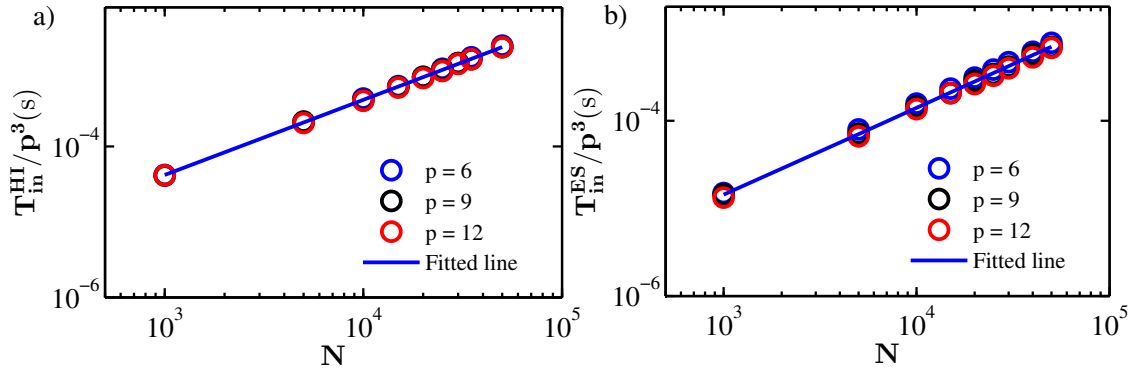
FIGURE 3.3: Interpolation execution time calculation for a) hydrodynamic interactions b) electrostatic interactions

analysis, it can be seen that the total time taken by the interpolation is independent on the interpolation order once it is divided by the factor p^3, which once again, proves that our scaling argument for evaluating the term T_{in} is valid. Also, none of the parameters, M, α, c, r_c or K_{mesh} have any influence on the value of t_{in}.

As mentioned in the preceding section, for the present analysis, the Fourier transforms are performed by using the FFTW_MEASURE subroutine available in the *FFTW package*. The scaling parameter t_{fft}, in Eq. 3.28, is obtained numerically by varying the value of K_{mesh} from 25 to 400 for HI interactions, and from 15 to 400 for ES interactions. After getting the numerical results at various values of K_{mesh}, they are fitted according to Eq. 3.28, using linear least squares regression fitting analysis, and the results are presented in Figs. 3.4a and 3.4b for HI and ES,
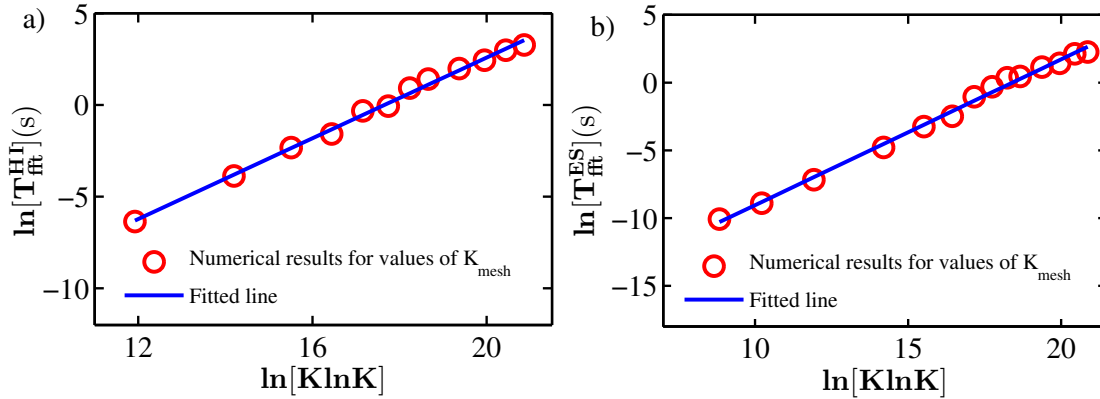
FIGURE 3.4: FFT execution time calculation for a) hydrodynamic
interactions b) electrostatic interactions

respectively. The values of $t_{\text{fft}}^{\text{HI}}$ and $t_{\text{fft}}^{\text{ES}}$ are obtained as $3.62 \times 10^{-9} \pm 2.33 \times 10^{-11}$
(s) and $2.47 \times 10^{-9} \pm 2.14 \times 10^{-11}$ (s) for HI and ES interactions, respectively.

3.4.2   Comparison between the analytical and numerical total execution time

After evaluating the values of t_{real}, t_{in} and t_{fft} for both HI and ES interactions,
we can analytically calculate the total CPU time by substituting these values into
Eq. 3.30 for a system with $N = 5000$, $c = 2$ and $M = 3.3$ for both HI and ES
interactions separately. In order to do this, we vary the value of α from 0.8 to 2.4
with a step of 0.0014 for HI, and from 0.85 to 2.7 with a step of 0.0037 for ES
interactions, whereas, the value of p is varied from 6.8 to 11 with a step of 0.0084
for HI, and from 5.8 to 19 with a step of 0.026 for ES interactions. In Figs. 3.5
and 3.6, we represent three dimensional graphs which show the total computational
time for various combinations of the values of α and p for HI and ES interactions,
respectively. These figures clearly demonstrate that, for this combinations of N,
c and M, the total computation time attains an optimum value for a particular
set of values of α and p, for both HI and ES interactions. In order to verify this
numerically, we compare our analytical T_{CPU} with numerical values at different
cross sections of the three dimensional plot, along the axes of α and p, for both
HI and ES interactions at the specified values of N, c and M. Figs. 3.7a and 3.7b
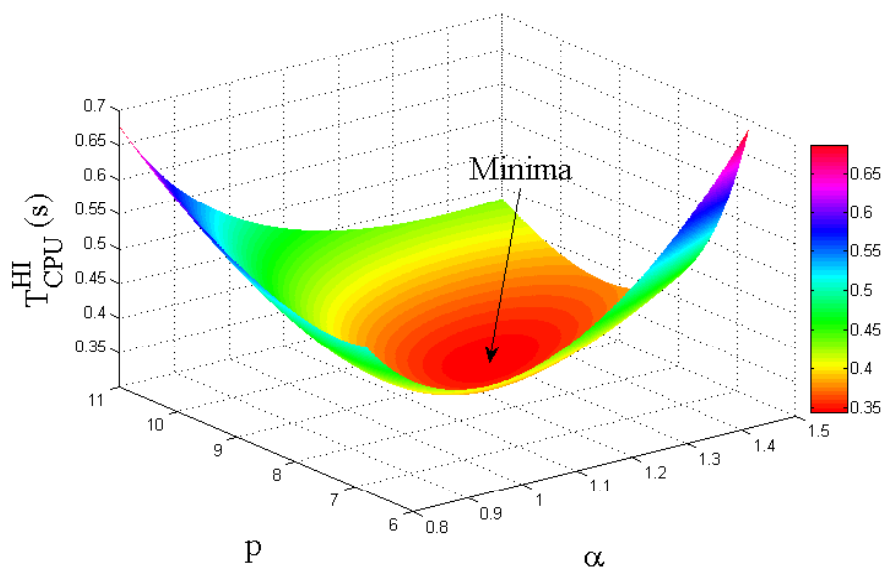
FIGURE 3.5: Three dimensional plot showing the analytical minima of the total execution time for hydrodynamic interactions at $N = 5000$, $c = 2$ and $M = 3.3$

show comparisons of the analytical and numerical total computational times as a function of the value of order of interpolation, p, at various constant values of the Ewald splitting parameter, α, for HI and ES interactions, respectively. From these figures, it can be clearly seen that there is excellent agreement between the results predicted analytically by Eq. 3.30 and numerically, for both hydrodynamic and electrostatic interactions. Comparisons of the total CPU time taken by analytical predictions and numerical simulations for differnt values of α, at different constant values of order of interpolation p, are presented in Figs. 3.8a and 3.8b for HI and ES interactions, respectively. Once again, the agreement seen between the analytical predictions and numerical simulations is very satisfactory for both HI and ES interactions.

It follows that for any given value of simulation parameters, the optimum values of α and p to be used in the SPME method can be obtained by finding the roots of the two non-linear Eqs. 3.31 and 3.32.
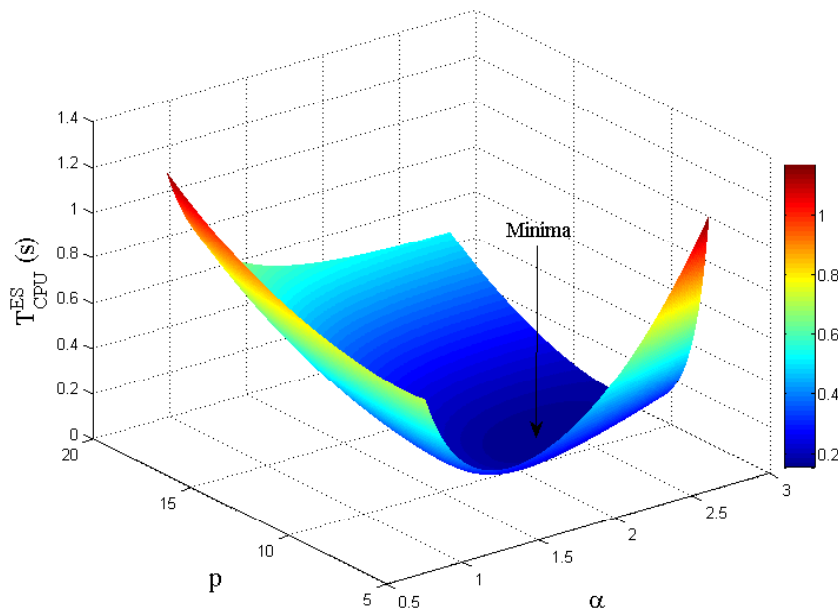
FIGURE 3.6: Three dimensional plot showing the analytical minima
of the total execution time for electrostatic interactions at $N =
5000$, $c = 2$ and $M = 3.3$

3.4.3   Comparison with the optimized Ewald sum

In this section, we present a detailed comparison of the total CPU time taken
between the current optimized SPME method and the previous optimized Ewald
sum techniques (Fincham, 1994; Jain et al., 2012b) for evaluating both long-ranged
hydrodynamic and electrostatic interactions. For the present simulation system,
there are two input paramters which can be adjusted, namely, the concentration,
c, and the desired accuracy parameter, M. Once these two are fixed, we vary
the total number of particles, N, in the system, and compute the total CPU time
needed for calculating both HI and ES interactions by the optimized SPME and
the optimized Ewald sum techniques separately, in order to carry out a comparison
between them. For this purpose, we choose a system with concentration of $c = 1$,
and we maintain an accuracy determined by setting $M = 3.3$, while we vary N
between 1000 and 40000 for both HI and ES interactions. As mentioned earlier, in
case of the optimized Ewald sum, for known values of c, M and N, the procedure
for calculating the optimized total CPU time was proposed by Fincham (1994) in
the case of ES interactions, while Jain et al. (2012b) proposed a scheme for HI
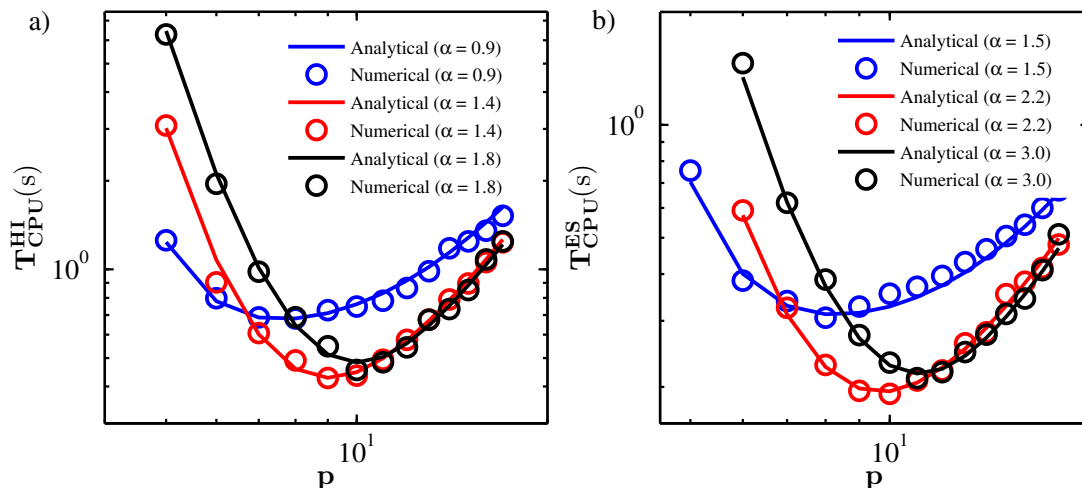
FIGURE 3.7: Comparison between the analytically predicted T_{CPU} and numerically obtained T_{CPU} at various constant values of α for a) hydordynamic interactions b) electrostatic interactions

interactions. In the present case, the total CPU time for the optimized Ewald sum is calculated exactly as was done by Fincham and Jain *et al.* for ES and HI interactions, respectively. Their optimization procedure eventually leads to an algorithm of order $O(N^{1.5})$, by balancing the computational load between the real space and reciprocal space sums with the help of an optimum choice of the Ewald spliting parameter α for both HI and ES interactions. On the other hand, for the present SPME technique, once the values of c, M and N are choosen, the other governing parameters are calculated as follows: the length of the system is calculated from the expression $L = (N/c)^{1/3}$, the optimum values of order of interpolation, p, and Ewald spliting parameter, α, are calculated by solving the two non-linear coupled equations defined by Eqs. 3.31 and 3.32, and finally the number of mesh points is calcualted based on Eq. 3.25, using the optimum values of p and α. For each particle number, we follow the aformentioned procedure in order to calculate the total CPU time for both HI and ES interactions. As discussed earlier, the highest computational cost that is needed for any step for evaluating the long-ranged interactiing terms for both HI and ES interactions, is the FFT evaluation step amongst all the steps involved in the SPME technique. As we know that FFT always performs all its calcualtion with an order of $O(N \ln N)$, so one can
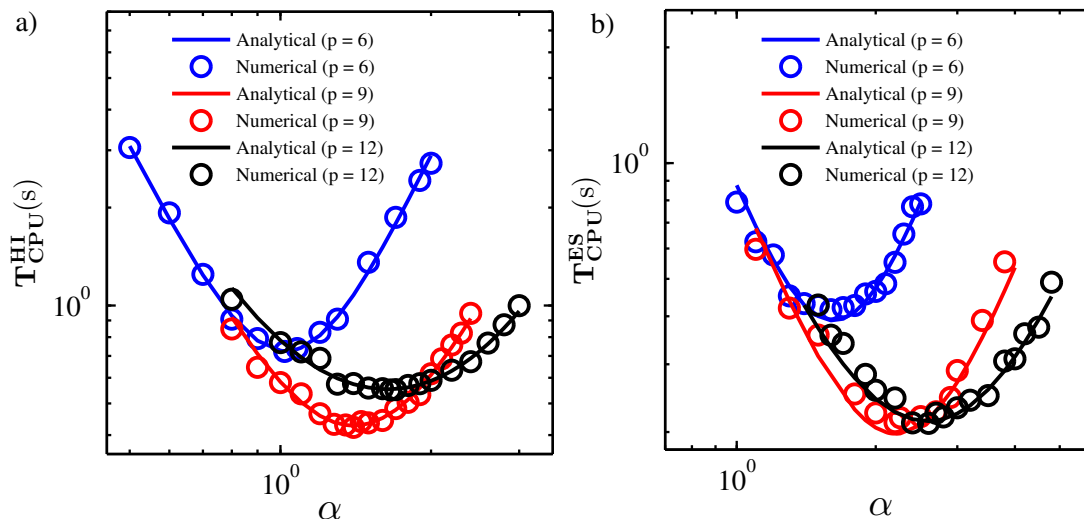
FIGURE 3.8: Comparison between the analytically predicted T_{CPU} and numerical obtained T_{CPU} at various constant values of p for a) hydrodynamic interactions b) electrostatic interactions

expect that the present algorithm will follow the same. Figs. 3.9 and 3.10 depict the plots of the total CPU time versus the total number of particles for both the optimized Ewald sum and SPME method for HI and ES interactions, respectively. From these figures, two points can be made: firstly, the SPME technique scales as $O(N \ln N)$ as expected for both HI and ES interactions. Secondly, there is a crossover at around $N \approx 2500$ below which the optimized Ewald sum is better in performance, but above which the optimzed SPME technique is much faster. For instance, in the case of HI interactions, for a system of 40000 particles, the optimized Ewald sum takes ~ 90.44 (s), while the optimized SPME takes only ~ 3.82 (s) for identical systems.

However, it should be noted that the current algorithm is not the fastest one that can be developed. It can be made faster by employing paralalliza-tion techniques using MPI (Message Passing Interface) or OpenMP (Open Multi-Processing) for the operation of FFTW. Further, the present optimization tech-nique has been proposed for a system at equilibrium, where the simulation box is a cube which is fixed in shape, i.e., it is not deforming with time. It could be more challenging to develop such a scheme for a system which is under flow. In
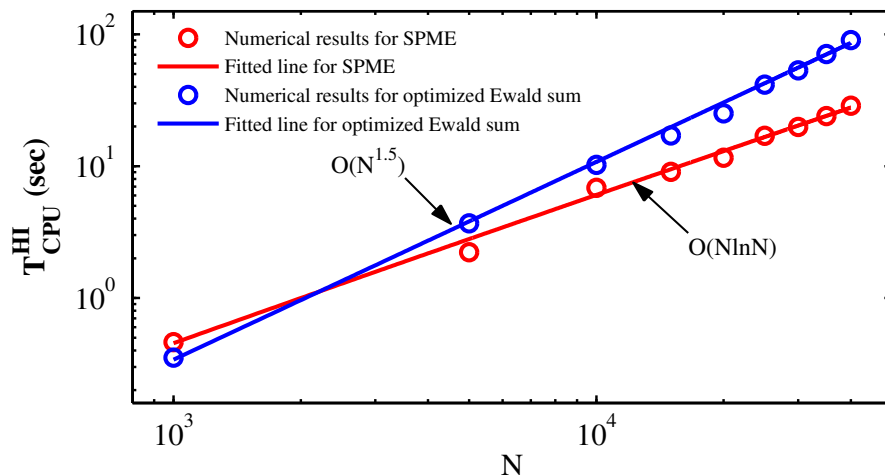
FIGURE 3.9: Comparison of total CPU time taken between the optimized Ewald sum and optimized SPME method for hydrodynamic interactions

the literature, there are two types of canonical flows present, namely, shear flows and extensional flows. In both shear and extensional flows, the simulation box deforms in time, and therefore, making it more challenging to implement the SPME technique. As far as we know, there has so far not been an implementation of the SPME technique for a system undergoing flow. This is worthy of study in the future.

3.5 Summary

In this work, a range of issues related to the implementation of the smooth particle mesh Ewald method, and its optimization procedure has been discussed in detail both in the context of long-ranged hydrodynamic and electrostatic interactions, which are present in a variety of soft matter systems, such as polymer solutions, colloidal suspensions, polyelectrolyte solutions, etc. The key findings are summarized here as follows:

1. In the present study, the well known smooth particle mesh Ewald technique originally developed by Essmann et al. (1995) for long-ranged electrostatic
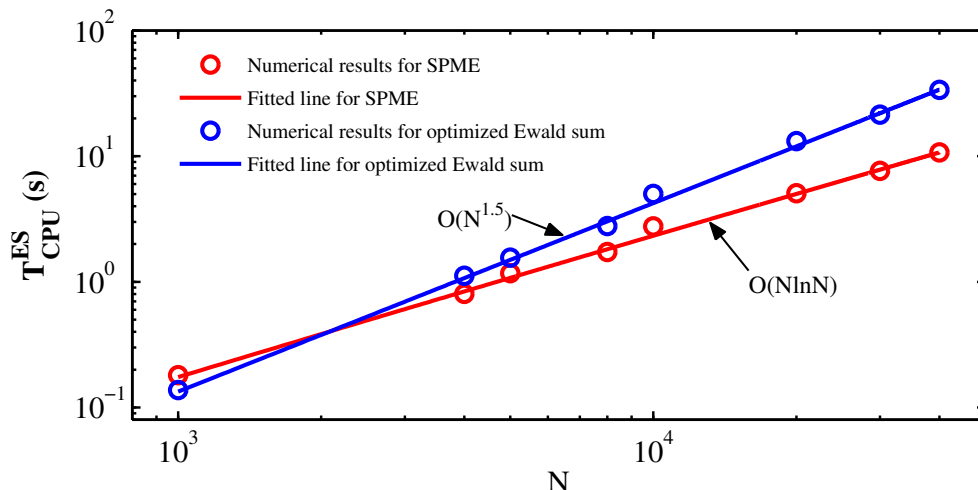
FIGURE 3.10: Comparison of total CPU time taken between the
optimized Ewald sum and optimized SPME method for electrostatic
interactions

interactions, has been successfully extended to long-ranged hydrodynamic
interactions treated by the Rotne-Prager-Yamakawa tensor.

2. It is possible to choose the optimal governing parameters for the SPME
    technique based on scaling arguments for the times taken by different steps
    involved in the method, for both the HI and ES interactions. This in turn,
    leads to the total CPU time needed for the evaluation of the long-ranged
    interactions to be a minimum value.

3. Based on the scaling arguments, as expected, the SPME method scales as
    $N \ln N$ for both electrostatic and hydrodynamic interactions. Furthermore,
    the total CPU time taken by the SPME method is compared with that of
    optimized Ewald sum, which scales as $O(N^{1.5})$, in the context of both HI
    and ES interactions. Interestingly, there is a crossover at around a total
    number of particles, $N \approx 2500$, for both HI and ES interactions, below
    which the optimized Ewald sum seems to be faster than the optimized SPME
    method. Overall, for a system of particles more than 5000, depending upon
    the particle number, the present optimized SPME method may lead a 5 to 30
    fold improvement in the speed of calculation for both HI and ES interactions.

The present study has shown that under otherwise identical conditions, the optimized Ewald method seems to be faster than the optimized SPME method for particle number below 2500 in the context of both HI and ES interactions. The maximum number of particles that we consider in the present thesis to solve all the problems as mentioned in Chapter 1, is around 2000. Therefore, we have used the optimized Ewald method to treat long-ranged hydrodynamic interactions in all our simulations.

Chapter 4

Planar mixed flows of polymer solutions at finite concentrations

4.1   Introduction

The study of the rheological behaviour of polymer solutions under different flow conditions has always been of great interest to the rheology community, both from a fundamental, and a practical point of view (Bird et al., 1987a; Larson, 1999). The most commonly studied flows are shear and elongational flows because of their simplicity. They have proven to be useful in understanding many industrial processes such as extrusion, injection molding and sheet casting, to name but a few (Baird and Collias, 1998). In many practical situations, however, rather than only shear or elongational flow, a combination of these flows is often observed. A special case is the linear combination of shear and elongational flow, the so-called *mixed flow* (Fuller and Leal, 1981; Hur et al., 2002; Woo and Shaqfeh, 2003; Dua and Cherayil, 2003; Hoffman and Shaqfeh, 2007). While elongational flows are shear free flows, shear flows have equal contributions from vorticity and elongation. In mixed flows both elongational and rotational components exist but their contributions vary, characterized by a *mixedness* parameter χ. In the limit $\chi \to 0$, the flow reduces to shear flow, while the limits $\chi \to -1$ and $\chi \to 1$, correspond to pure rotational and pure elongational flow, respectively. Experimentally, mixed flows have been generated and studied using the four-roll mill (Lee et al., 2007).

While there have been relatively few computational studies of mixed flows of dilute polymer solutions (Hur et al., 2002; Woo and Shaqfeh, 2003; Dua and Cherayil, 2003; Hoffman and Shaqfeh, 2007), there have been almost no computational studies of polymer solutions at finite concentrations undergoing mixed flow. Such flows are of significant interest in many practical applications, particularly in situations where there is a strong elongational component to the deformation, such as in inkjet printing or fibre spinning (Xu et al., 2007; Zettl et al., 2009). Consequently, obtaining a quantitative understanding of the rheological behaviour of non-dilute polymer solutions is not only of fundamental importance, but also vitally important for a number of practical applications. The aim of this chapter is to develop a predictive understanding of polymer solutions at finite concentrations subjected to planar mixed flows.

A challenging aspect of the development of an algorithm to simulate flows of finite-concentration polymer solutions, is the implementation of appropriate periodic boundary conditions (PBCs), arising from the need to carry out simulations for an indefinitely long time. PBCs for planar shear flows and planar elongational flows have been developed by Lees and Edwards (1972) and Kraynik and Reinelt (1992), respectively, that enable computations to run indefinitely in these flows. These PBCs have, for example, been used by Bhupathiraju et al. (1996) and Todd and Daivis (1998) in nonequilibrium molecular dynamics (NEMD) simulations. Apart from NEMD simulations, these PBCs have also been implemented in a Brownian dynamics (BD) simulation algorithm by Stoltz et al. (2006) to simulate semidilute polymer solutions undergoing planar shear and planar elongational flows. In the context of planar mixed flows, Woo and Shaqfeh (2003) and Dua and Cherayil (2003) and Hoffman and Shaqfeh (2007) have carried out simulations of dilute polymer solutions using a BD algorithm. However, PBCs are *not* required in single chain simulations. Hunt et al. (2010) have derived suitable PBCs for planar mixed flows and implemented them in an NEMD algorithm, which has recently been applied in a couple of different contexts (Hartkamp et al., 2012; Hartkamp

et al., 2013)

While NEMD simulations have led to important insights into the behaviour of polymer melts in a variety of flows (Todd, 2001; Kröger, 2004; Hajizadeh et al., 2014) they are not suited to simulating the large-scale and long-time behaviour of solutions of long polymer chains, because of the large number of degrees of freedom involved, and because such systems typically have relaxation times that are of the order of several seconds. Basically, the need to resolve the uninteresting motions of all the solvent molecules for extended periods of time, makes NEMD simulations computationally expensive and inefficient. It is generally accepted that the best approach under these circumstances is to use mesoscopic simulation algorithms, such as the hybrid LB/MD (Ahlrichs and Dünweg, 1999), or MPCD (Gompper et al., 2009) algorithms, or Brownian dynamics, in which the solvent molecules are discarded altogether and treated implicitly.

Only recently, mixed flow PBCs have been implemented in the context of a BD algorithm by Jain (2013) by adopting the PBC implementation in NEMD by Hunt et al. (2010). The development of such an algorithm enables the simulation of the large-scale and long-time properties of polymer solutions in industrially relevant flows at finite concentrations.

Shaqfeh and coworkers (Hur et al., 2002; Woo and Shaqfeh, 2003; Hoffman and Shaqfeh, 2007), have shown that the mixedness parameter χ is essential to understanding the nature of polymer behaviour in mixed flows. For instance, χ is a key parameter in determining the existence of the phenomenon of coil-stretch hysteresis (Gennes, 1974; Schroeder et al., 2003; Schroeder et al., 2004a). Here, we study the influence of flow type χ, and flow strength $\dot{\Gamma}$ on the viscosity in planar mixed flows, using the definition of viscosity introduced by Hounkonnou et al. (1992) (as defined by Eq. 2.27 in Chapter 2). Additionally we show that, as in the case of dilute solutions, there exits a critical value, χ_c, below which the flow is shear dominated, while being extension dominated for $\chi > \chi_c$. We find that the concentration of the polymer solution influences χ_c, and consequently the nature

of the flow.

The plan of this chapter is as follows. In Section 4.2, we present the details of simulations, summary of the implementation of PBCs in planar mixed flows (Section 4.2.1), and the validation of the BD algorithm by comparison with known results (Section 4.2.2). In Section 4.3, the results of simulations of FENE dumbbells are presented, and the influence of flow strength and mixedness parameter on polymer size and viscosity is discussed. The central conclusions of this work are summarised in Section 4.4.

4.2   Polymer model and simulation details

The polymer model and the governing equations are given in Chapter 2 for the bead position vectors (Section 2.2), different spring force laws (Section 2.3), and EV potential (Section 2.4.2). Different forms of the velocity gradient tensor for planar mixed flows and the definition of various macroscopic properties are discussed in Sections 2.5 and 2.6, respectively in Chapter 2.

4.2.1   Periodic boundary conditions for planar mixed flows

The details of the implementations of PBCs in planar mixed flows in the context of present multi-chain BD algorithm can be found in Jain (2013). Here we present a summary of the implementation. In flow simulations, PBCs require that the shape of the simulation box changes with time in accordance with the flow such that the deformation of the simulation box follows the streamlines of the flow. As the simulation box deforms with respect to time, there comes a time when the box has deformed to such an extent that the minimum spacing between any two sides of the box becomes less than twice the inter-particle interaction range. At that point in time, particles start to interact with themselves and the simulation needs to be stopped. There might also be cases, such as in shear flows, where after some time, one of the sides of the box becomes very large resulting in numerical

problems. In other words, the deformation of the simulation box in such a manner restricts the simulation from proceeding for long times. In fact, this issue becomes even more serious for polymer molecules, since in this case, relaxation times in general are quite long, and it is very important to simulate them for sufficiently long time in order to capture their dynamics accurately. It is consequently necessary to perform a mapping of the simulation box such that the initial box configuration is periodically recovered. Remapping of the box configuration requires two conditions to be met: (i) *Compatibility*, which means that the minimum lattice spacing should never be less than twice the range of inter-particle interactions, and (ii) *Reproducibility*, which means that the lattice points of a lattice should overlap with the lattice points of the same lattice at a different time. Remapping of the lattice in NEMD simulations of planar shear flow was first carried out by Evans (1979) and Hansen and Evans (1994) who modified the original sliding-brick algorithm of Lees and Edwards (1972) to a deforming-box algorithm. Satisfying the two conditions of compatibility and reproducibility, Kraynik and Reinelt (1992) developed PBCs capable of being remapped, for planar elongational flows. The Kraynik-Reinelt PBCs were first implemented by Todd and Daivis (1998) and Baranyai and Cummings (1999) in their planar elongational NEMD simulation algorithms. In these PBCs, basically the lattice is started at an angle θ (the so-called magic angle) (Kraynik and Reinelt, 1992), then deformed for a certain period of time τ_p (the strain period), and then mapped back to its original state. This process of deforming the lattice till τ_p and mapping back to its original state is repeated as many times as needed, to achieve extended simulations.

Hunt et al. (2010) extended the PBCs for planar elongational flows to planar mixed flows in their NEMD simulations for the first time. Jain (2013) then adopted the reproducible periodic boundary conditions for planar mixed flow developed by Hunt et al. (2010), and used it in a multi-chain Brownian dynamics simulation algorithm for semidilute polymer solutions. Implementation of PBCs for planar mixed flow is similar to that for planar elongational flow (Kraynik and Reinelt,
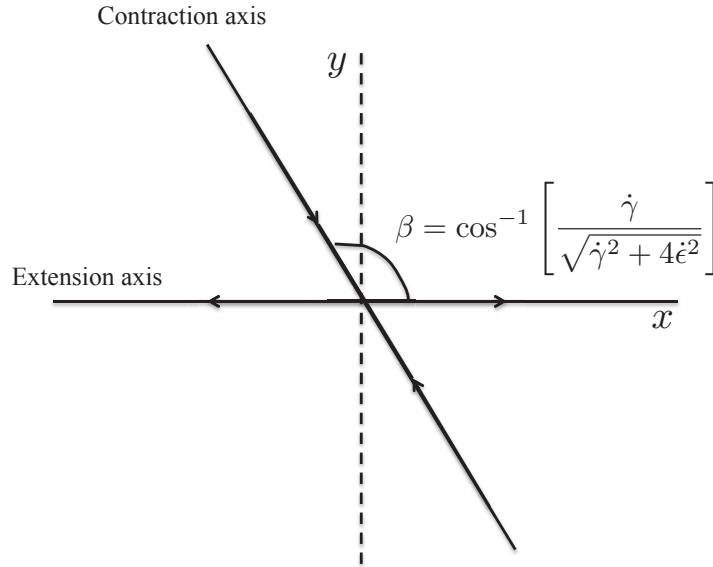
FIGURE 4.1:   Extension and contraction axes in planar mixed flow (Jain, 2013).

1992; Todd and Daivis, 1998), except for some differences due to the presence of a rotational component. These differences are briefly outlined below, along with the major steps in the implementation of PBCs for PMF.

In the canonical representation, the eigenvalues of $(\nabla v)_{\text{PMF}}$ are $\{\dot{\epsilon}, -\dot{\epsilon}, 0\}$, and a possible choice of the corresponding eigenvectors is $(1, \dot{\gamma}/2\dot{\epsilon}, 0)$, $(0, 1, 0)$ and $(0, 0, 1)$. It is worth noting that the eigenvalues of the velocity gradient tensor of the canonical PMF are equivalent to those for PEF, where $(\nabla v)_{\text{PEF}}$ is already in a diagonal form. However, the eigenvectors corresponding to the eigenvalue $\dot{\epsilon}$ are different for $(\nabla v)_{\text{PMF}}$ and $(\nabla v)_{\text{PEF}}$. For PEF, the eigenvector corresponding to $\dot{\epsilon}$ is $(1, 0, 0)$, which leads to the fact that the extension axis and contraction axis are orthogonal. In case of the canonical PMF, the eigenvector corresponding to $\dot{\epsilon}$ is $(1, \dot{\gamma}/2\dot{\epsilon}, 0)$, resulting in a system where the extension axis and contraction axis are non-orthogonal (for simplicity, we will henceforth refer to "canonical" PMF as PMF). In PMF, the angle β between the extension axis and the contraction axis (displayed in Fig. 4.1), depends on the ratio of $\dot{\gamma}$ to $\dot{\epsilon}$ since,

$$\beta = \cos^{-1}\left[\frac{\dot{\gamma}}{\sqrt{\dot{\gamma}^2 + 4\dot{\epsilon}^2}}\right] \tag{4.1}$$

Two important parameters with regard to PBC implementation in flow are the magic angle and strain period, both of which depend on the eigenvalues of the velocity gradient tensor. Since the eigenvalues of the velocity gradient tensor for PMF and PEF are the same, the magic angle and strain period for PMF can be obtained in a similar manner as in the case of PEF. However, the initial lattice configuration for PMF is different from that of PEF because of the differences in the eigenvectors discussed above. Details of the initial lattice vectors for both PEF and PMF can be found in Jain (2013).

For the sake of completeness, the derivation of initial lattice vector for PMF is discussed in Appendix B. Here, the steps involved in the implementation of PBCs for PMF are briefly enumerated below:

1. An integer value of the parameter $\tilde{k}$ (which controls both the magic angle and the strain period) is chosen, such that $\tilde{k} \geq 3$, and $\tilde{k} \in [3, 4, 5, \ldots]$.

2. The eigenvalue ϕ (as defined in Kraynik and Reinelt (1992)) is calculated using the expression,

$$\phi = \frac{\tilde{k} + \sqrt{\tilde{k}^2 - 4}}{2} \tag{4.2}$$

3. The strain period τ_p is estimated using the expression $\tau_p = \log(\phi)/\dot{\epsilon}$, where $\dot{\epsilon}$ is the elongational rate.

4. A choice is made for the values of N_{11} and N_{12}, which are the "11" and "12" elements of a 3×3 integer matrix that describes the mapping between the deformed and original matrix, as follows. Basically, a positive integer value of N_{11} is selected such that an integer value of N_{12} is obtained using the expression,

$$N_{12} = -\sqrt{N_{11}(\tilde{k} - N_{11}) - 1} \tag{4.3}$$

Various possible values of N_{11} and N_{12} are listed in Kraynik and Reinelt (1992).

5. Finally, the magic angle is calculated from,

$$\theta = \tan^{-1}\left[\frac{N_{11} - \phi}{N_{12}}\right] \tag{4.4}$$

Using initial lattice vectors that depend on the magic angle, the simulation can be started and run until the strain period. The lattice is then mapped back to its original state, and this way the simulation can be carried out for an extended period.

With regard to the compatibility condition, as discussed earlier, there is an issue with the length of one of the sides of the simulation box decreasing with time. Kraynik and Reinelt (1992) have shown that the reproducibility condition automatically guarantees the compatibility condition, i.e., they have shown that the distance $D(\tau_p)$ between any two lattice points at time τ_p is never less than the minimum lattice spacing $D_{\min}$, such that the lattice points do not overlap. In simulations, the cutoff radius of any inter-particle interaction potential is always chosen to be less than $D_{\min}/2$, which ensures that the compatibility condition is always satisfied. The derivation of $D_{\min}$ for PMF has been discussed by Hunt et al. (2010).

4.2.2   Validation of the BD algorithm

In order to validate the multi-chain BD flow algorithm, results are compared with the results from single-chain BD simulations in the dilute limit. Since the current algorithm is an extension of the previous equilibrium multi-chain BD algorithm (Jain et al., 2012b), the new additional features in the present algorithm are the implementation of (i) periodic boundary conditions for planar mixed flows, and (ii) a neighbour-list consistent with PBCs for PMF.

Results are reported in terms of the scaled variable, $c/c^\star$ and in order to compare results of the multi-chain algorithm with dilute solution results, we typically

choose extremely small values of $c/c^\star$ to prevent any likelihood of chain-chain interactions.

The Weissenberg number is defined as $Wi = \lambda_\eta \dot{\gamma}$, which is a non-dimensional measure of the strain rate. The quantity λ_η is a characteristic relaxation time defined by,

$$\lambda_\eta = \frac{[\eta]_0 M \eta_s}{N_A k_B T} \tag{4.5}$$

where, $[\eta]_0$ is the zero shear rate intrinsic viscosity of the solution, M is the molecular weight, η_s is the solvent viscosity, and N_A is Avagadro's number. One can show (Prakash, 2002a), in terms of the non-dimensionalisation scheme used here, that this definition implies that $\lambda_\eta = \eta_0$, where η_0 is the zero shear rate polymer contribution to the viscosity. Consequently, $Wi = \eta_0 \dot{\gamma}$.

The neighbour-list and PBCs do not play a role in the flow simulation when hydrodynamic and excluded volume interactions are ignored. This situation corresponds to the Rouse model for which analytical expressions for various properties are known. For instance, the Rouse model predicts a constant viscosity in case of shear flow, independent of the shear rate, which can be calculated analytically to be (Bird et al., 1987b),

$$\eta_{\text{Rouse}} = \frac{N_b^2 - 1}{3} \tag{4.6}$$

In order to test the neighbour-list and PBCs implementations, multi-chain BD simulations of dumbbells ($N_b = 2$) have been carried out in the ultra dilute limit, with excluded volume interactions between the dumbbell beads. In particular, we set $z = 1.7$, $N_c = 10$, $c/c^\star = 6 \times 10^{-12}$ and $\Delta t = 0.005$. A large number of independent runs (in the range of 10^3 - 10^6) were performed in order to obtain results with acceptable error bars. We first examine the behaviour of the algorithm in transient flows, followed by steady state flows, in both planar shear and extensional modes of deformation. The former is important in order to ensure that there are no artifacts caused due to the periodic re-mapping of the system after every strain period.
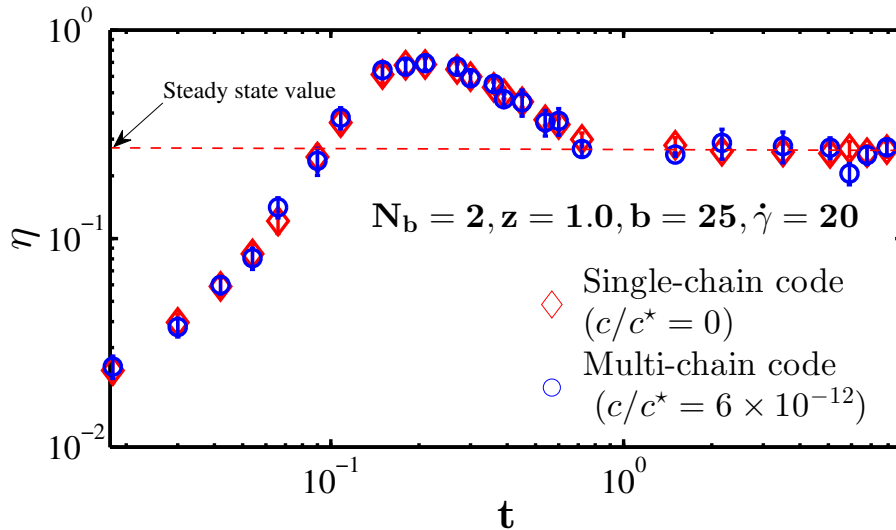
FIGURE 4.2: Comparison of the transient viscosity upon inception
of steady planar shear flow at non-dimensional times t, predicted
by the multi-chain BD algorithm, with the results of single-chain
BD simulations in the dilute limit. Excluded volume interactions
are taken into account but hydrodynamic interactions are switched
off. The parameter values are as indicated in the figure legend.

Figure 4.2 displays the growth in the transient viscosity upon inception of
steady planar shear flow as a function of time. Clearly, there is excellent agreement
between the multi-chain and single chain simulations (for which the neighbour-list
and PBCs are not required). In particular, the well known overshoot phenomena
in such flows (Bird et al., 1987b), that occurs at high shear rates, is accurately
captured by the multi-chain simulations.

Figure 4.3 compares the steady state viscosity ratio η/η_{Rouse}, as a function
of Wi, predicted by the multi-chain and single chain BD simulations. As is well
known, the incorporation of excluded volume interactions into kinetic theory mod-
els of polymer solutions leads to the prediction of shear thinning (Prabhakar and
Prakash, 2002; Kumar and Prakash, 2004a). This is believed to arise for the fol-
lowing reason. The value of the zero shear rate viscosity is greater in the presence
of excluded volume interactions than in its absence, because of the swelling of the
polymer coil. When flow is switched on, however, the increase in the separation be-
tween segments of the chain leads to a weakening of excluded volume interactions,
and consequently a decrease in the viscosity. The behaviour displayed in Fig. 4.3
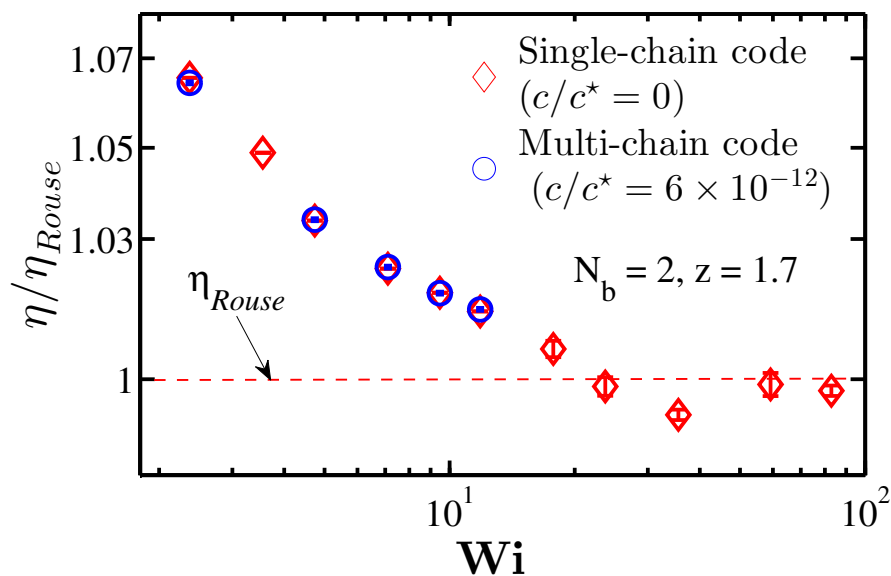
FIGURE 4.3: Comparison of the viscosity η, at various Wi, predicted by the multi-chain BD algorithm with the results of single-chain BD simulations in the ultradilute limit.

is in line with this expectation, with the viscosity decreasing from its enhanced value at low shear rates, where excluded volume interactions are still strong, to the Rouse viscosity in the limit of high shear rates, where excluded volume interactions are absent. Once again, the agreement between multi-chain and single chain simulations indicates the robustness of the former algorithm.

We turn our attention now to validation studies for planar elongational flows. In all the PEF simulations reported here, we have used $\tilde{k} = 3$ and $N_{11} = 2$, which are required for calculating the strain period and the magic angle as discussed in the previous section. For PEF simulations, spring forces cannot be modeled using the Hookean force law, which permits the physically unrealistic indefinite extension of the spring. Since the finite extensibility of the polymer is important in situations where the molecule is likely to be close to full extension, such as in strong shear or elongational flows, a FENE spring force (defined by Eq. 2.5 of Chapter 2) is used here to model spring forces in PEF.

As in the case of planar shear flow, we first examine the validity of the algorithm for a transient flow, namely, the inception of steady planar elongational
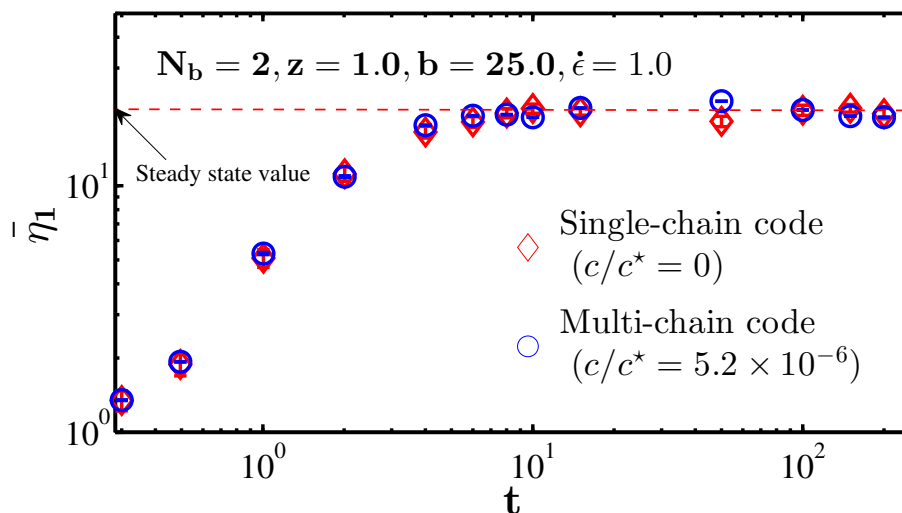
FIGURE 4.4:   Comparison of the transient viscosity upon inception of steady planar extensional flow, at non-dimensional times t, predicted by the multi-chain BD algorithm, with the results of single-chain BD simulations in the dilute limit.
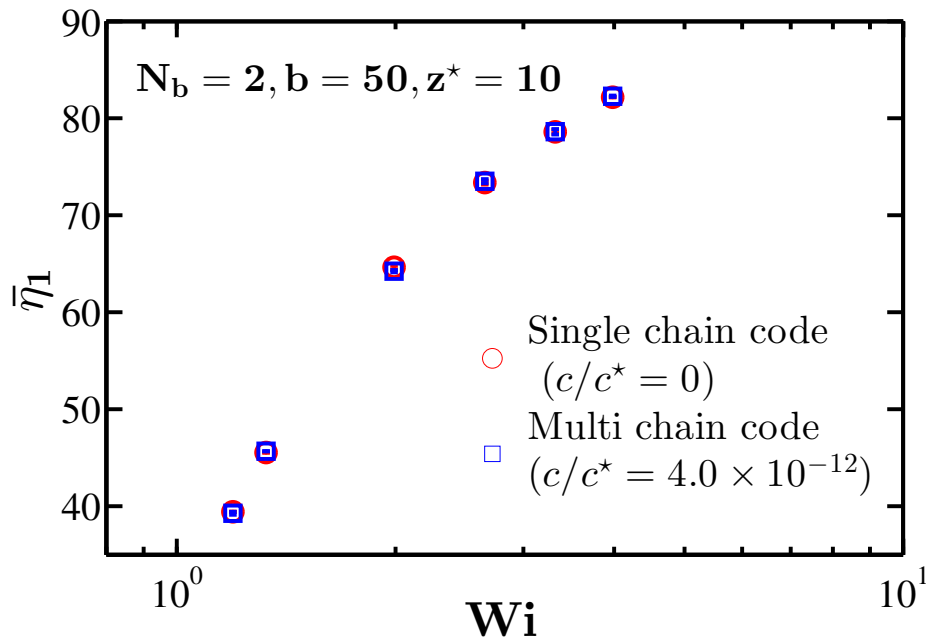
(b)

FIGURE 4.5:   Comparison of $\bar{\eta}_1$ predicted by the multi-chain BD algorithm with the results of single-chain BD simulations, at various $\dot{\epsilon}$, in the dilute limit for $z^{\star} = 10$.

flow. Figure 4.4 displays the growth in the extensional viscosity as a function of time. As is well known, the viscosity increases monotonically as polymer chains unravel from a coiled state to a stretched state under the action of flow, before levelling off to a steady state value (Bird et al., 1987b). It is clear that the multi-chain algorithm accurately captures the variation of the viscosity with time. The perfect agreement between the multi-chain and single chain simulations in both the transient flows examined here indicates that the remapping of the system at each strain period has been implemented successfully.

Multi-chain BD simulations have been carried out to obtain the steady state value of $\bar{\eta}_1$ for a range of $\dot{\epsilon}$, for $z^\star = 10$, corresponding to a good solvent. We set $d^\star = 1$, $N_c = 500$, $c/c^\star = 2 \times 10^{-16}$ and the FENE parameter $b = 50$. Simulation results are shown in Fig. 4.5, obtained by multi-chain and single-chain simulations, in terms the Weissenberg number, which in this case is defined by the expression, $Wi = \lambda_\eta \dot{\epsilon}$. Clearly, there is excellent agreement between the multi-chain and single-chain results, validating the implementation of the current BD algorithm in planar extensional flows.

4.3 Planar mixed flows of polymer solutions at finite concentrations

In this section, we describe the new results of this work, namely, the prediction of polymer size (in terms of the end-to-end distance, $\langle R_e^2 \rangle$, defined by Eq. 2.18 in Chapter 2) and viscosity (defined by Eq. 2.26 in Chapter 2) in planar mixed flows at finite concentrations. We consider a simple system of FENE dumbbells ($N_b = 2$) with finite extensibility parameter $b = 25$. The excluded volume parameters are chosen to be $z^\star = 1/\sqrt{2}$, and $d^\star = 0.93$. Data is presented for two values of $c/c^\star$: (i) $c/c^\star = 0.176$, and (ii) $c/c^\star = 1.0$. The lattice parameters $\tilde{k}$ and N_{11} are chosen to be 3 and 2, respectively, for all the results reported in this section.
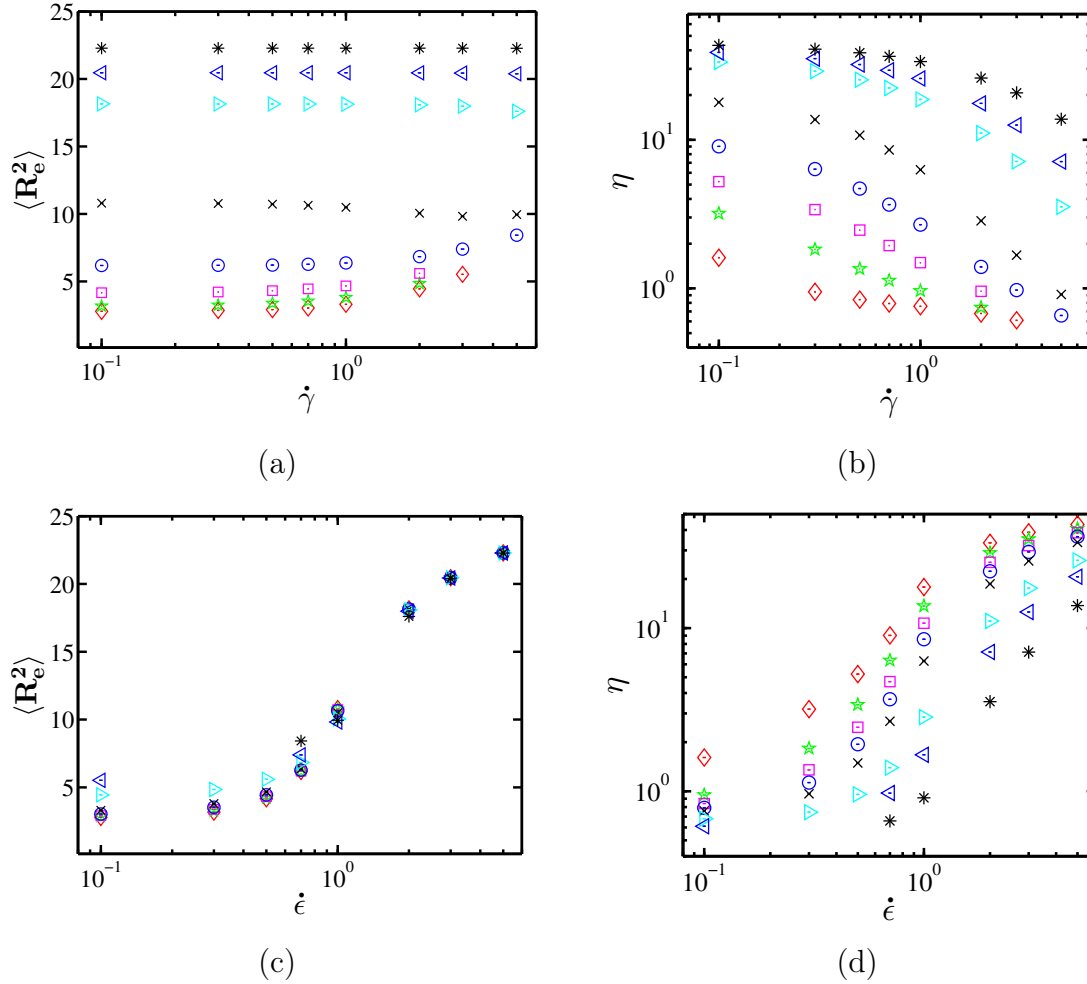
FIGURE 4.6:   Variation of polymer size and viscosity with shear rate $\dot{\gamma}$, and elongation rate $\dot{\epsilon}$, in planar mixed flow. (a) Variation of polymer size with $\dot{\gamma}$ at various fixed values of $\dot{\epsilon}$: $\diamond$ $\dot{\epsilon} = 0.1$, $\star$ $\dot{\epsilon} = 0.3$, $\square$ $\dot{\epsilon} = 0.5$, $\circ$ $\dot{\epsilon} = 0.7$, $\times$ $\dot{\epsilon} = 1.0$, $\triangleright$ $\dot{\epsilon} = 2.0$, $\triangleleft$ $\dot{\epsilon} = 3.0$, $*$ $\dot{\epsilon} = 5.0$; (b) Variation of viscosity with $\dot{\gamma}$ at various fixed values of $\dot{\epsilon}$: $\diamond$ $\dot{\epsilon} = 0.1$, $\star$ $\dot{\epsilon} = 0.3$, $\square$ $\dot{\epsilon} = 0.5$, $\circ$ $\dot{\epsilon} = 0.7$, $\times$ $\dot{\epsilon} = 1.0$, $\triangleright$ $\dot{\epsilon} = 2.0$, $\triangleleft$ $\dot{\epsilon} = 3.0$, $*$ $\dot{\epsilon} = 5.0$; (c) Variation of polymer size with $\dot{\epsilon}$ at various fixed values of $\dot{\gamma}$: $\diamond$ $\dot{\gamma} = 0.1$, $\star$ $\dot{\gamma} = 0.3$, $\square$ $\dot{\gamma} = 0.5$, $\circ$ $\dot{\gamma} = 0.7$, $\times$ $\dot{\gamma} = 1.0$, $\triangleright$ $\dot{\gamma} = 2.0$, $\triangleleft$ $\dot{\gamma} = 3.0$, $*$ $\dot{\gamma} = 5.0$.; (d) Variation of viscosity with $\dot{\epsilon}$ at various fixed values of $\dot{\gamma}$: $\diamond$ $\dot{\gamma} = 0.1$, $\star$ $\dot{\gamma} = 0.3$, $\square$ $\dot{\gamma} = 0.5$, $\circ$ $\dot{\gamma} = 0.7$, $\times$ $\dot{\gamma} = 1.0$, $\triangleright$ $\dot{\gamma} = 2.0$, $\triangleleft$ $\dot{\gamma} = 3.0$, $*$ $\dot{\gamma} = 5.0$. In these simulations, $N_b = 2$, $b = 25$, $z = 1$, $d^\star = 0.93$, and $c/c^\star = 0.176$.

The influence of shear rate $\dot{\gamma}$ on the polymer size and viscosity at a fixed value of elongation rate $\dot{\epsilon}$, is examined in Figs. 4.6 (a) and (b), while the influence of elongation rate $\dot{\epsilon}$ at a fixed value of shear rate $\dot{\gamma}$, is examined in Figs. 4.6 (c) and (d). There are several features that can be discerned from these figures, which we discuss in turn below.

Fig. 4.6 (a) indicates that at any value of shear rate $\dot{\gamma}$, the polymer size increases with increasing elongation rate $\dot{\epsilon}$. This is to be expected since it is well known that chains unravel in extensional flows. The interesting point to note is that for $\dot{\epsilon} < 1$, $\langle R_e^2 \rangle$ increases with increasing $\dot{\gamma}$ until it asymptotes to a value of $\langle R_e^2 \rangle \approx 10$, while for $\dot{\epsilon} \geq 1$, $\langle R_e^2 \rangle$ *decreases* with increasing $\dot{\gamma}$, and appears to be reaching the same asymptotic value. Several experimental and theoretical studies of polymer conformations in pure simple shear flow have shown that the polymer size increases with increasing shear rate and typically saturates to roughly 40% of its fully stretched size. The chain is never fully stretched in shear flow because it experiences repeated stretching and tumbling events (readers can find an extended discussion of chain conformations in shear flow in Ref. Dalal et al. (2012), and references therein). This is consistent with the results in Fig. 4.6 (a) for $\dot{\epsilon} < 1$, since the square of the fully stretched contour length in the current simulations is given by the parameter $b = 25$ (in non-dimensional units). The decrease in polymer size with increasing shear rates, for $\dot{\epsilon} \geq 1$, can be understood from the fact that at any given elongation rate $\dot{\epsilon}$, the flow becomes increasingly shear dominated at sufficiently high values of $\dot{\gamma}$. This can be seen from the expression,

$$\frac{\dot{\gamma}}{\dot{\epsilon}} = \frac{(1-\chi)}{\sqrt{\chi}} \tag{4.7}$$

For a fixed value of $\dot{\epsilon}$, as $\dot{\gamma} \to \infty$, the mixedness parameter $\chi \to 0$. As a result, at sufficiently high values of $\dot{\gamma}$, we expect the polymer size to asymptote to its value in pure shear flow, regardless of the value of $\dot{\epsilon}$.

Fig. 4.6 (b) shows that at any value of shear rate $\dot{\gamma}$, the polymer contribution to

the solution viscosity, η, increases with increasing elongation rate $\dot{\epsilon}$. This behaviour is directly correlated with the size of the chain, since a larger chain size implies a larger volume fraction occupied by the chain, and consequently a larger viscosity. The shear thinning that is evident with increasing $\dot{\gamma}$, at all values of $\dot{\epsilon}$, is because of the inclusion of finite extensibility and excluded volume interactions in the model. The influence of these non-linear mesoscopic phenomena on dilute polymer solution behaviour in pure shear flows, has been discussed in detail in Refs. Prabhakar and Prakash (2002) and Prabhakar and Prakash (2004).

The unravelling of the polymer chain with increasing $\dot{\epsilon}$, at all values of $\dot{\gamma}$, is clearly evident in Fig. 4.6 (c). As is well known, in pure extensional flows, the conformation of a chain changes from being coil-like at low extension rates, to being fully stretched and rod-like at high extension rates, undergoing a coil-stretch transition at intermediate extension rates Prakash, 2009. At the lowest values of $\dot{\epsilon}$, the increase in $\langle R_e^2 \rangle$ with increasing $\dot{\gamma}$ is discernible on the scale of the figure. However, at values of $\dot{\epsilon} \gtrsim 10$, changes in $\dot{\gamma}$ have negligible influence on $\langle R_e^2 \rangle$. From Eq. (4.7), it is clear that at a fixed value of $\dot{\gamma}$, as $\dot{\epsilon} \to \infty$, the mixedness parameter $\chi \to 1$. As a result, at sufficiently high values of $\dot{\epsilon}$, we expect the polymer size to asymptote to its fully stretched value in pure elongational flow, i.e., $\langle R_e^2 \rangle / b \to 1$ as $\dot{\epsilon} \to \infty$, regardless of the value of $\dot{\gamma}$.

The behaviour of the polymer contribution to solution viscosity displayed in Fig. 4.6 (d), can be understood in the light of the results shown in Figs. 4.6 (b) and (c). At any value of extension rate $\dot{\epsilon}$, η decreases with increasing shear rate $\dot{\gamma}$, because of shear thinning. However, η increases with increasing $\dot{\epsilon}$ at all values of $\dot{\gamma}$, because the chain undergoes a coil-stretch transition in this process. The levelling off of η to a constant value at high extension rates, is related to the chain reaching its maximum state of stretch, at that particular value of $\dot{\gamma}$.

A completely different and valuable insight is obtained when we consider the behaviour of η (defined by Eq. 2.27 in Chapter 2) as a function of $\dot{\Gamma}$ and χ, instead of $\dot{\gamma}$ and $\dot{\epsilon}$. In contrast to η, however, the variation of $\langle R_e^2 \rangle$ with $\dot{\Gamma}$ and χ does not

have many features that cannot be anticipated from the results already displayed in Figs. 4.6 (a) and (c). These observations are discussed in greater detail below in the context of Figs. 4.7 (a) to (d), where results are presented in terms of a non-dimensional Weissenberg number defined by the expression, $Wi = \lambda_\eta \dot{\Gamma}$.
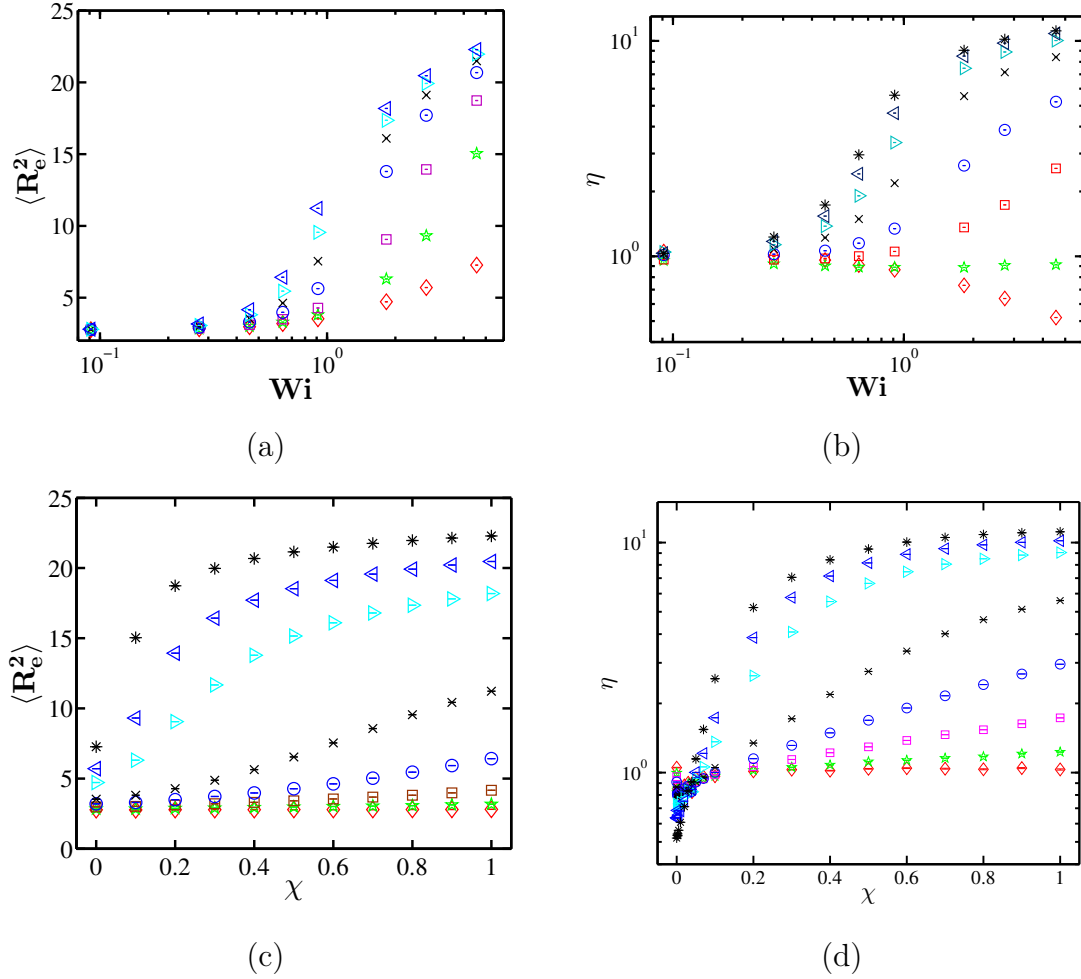
FIGURE 4.7:   Variation of polymer size and viscosity with flow strength $\dot{\Gamma}$, and mixedness parameter χ, in planar mixed flow. (a) Variation of polymer size with $\dot{\Gamma}$ at various fixed values of χ: $\diamond$ $\chi = 0.0$, $\star$ $\chi = 0.1$, $\square$ $\chi = 0.2$, $\circ$ $\chi = 0.4$, $\times$ $\chi = 0.6$, $\triangleright$ $\chi = 0.8$, $\triangleleft$ $\chi = 1.0$; (b) Variation of viscosity with $\dot{\Gamma}$ at various fixed values of χ: $\diamond$ $\chi = 0.0$, $\star$ $\chi = 0.04$, $\square$ $\chi = 0.1$, $\circ$ $\chi = 0.2$, $\times$ $\chi = 0.4$, $\triangleright$ $\chi = 0.6$, $\triangleleft$ $\chi = 0.8$, $*$ $\chi = 1.0$; (c) Variation of polymer size with χ at various fixed values of $\dot{\Gamma}$: $\diamond$ $\dot{\Gamma} = 0.1$, $\star$ $\dot{\Gamma} = 0.3$, $\square$ $\dot{\Gamma} = 0.5$, $\circ$ $\dot{\Gamma} = 0.7$, $\times$ $\dot{\Gamma} = 1.0$, $\triangleright$ $\dot{\Gamma} = 2.0$, $\triangleleft$ $\dot{\Gamma} = 3.0$, $*$ $\dot{\Gamma} = 5.0$; (d) Variation of viscosity with χ for various fixed values of $\dot{\Gamma}$: $\diamond$ $\dot{\Gamma} = 0.1$, $\star$ $\dot{\Gamma} = 0.3$, $\square$ $\dot{\Gamma} = 0.5$, $\circ$ $\dot{\Gamma} = 0.7$, $\times$ $\dot{\Gamma} = 1.0$, $\triangleright$ $\dot{\Gamma} = 2.0$, $\triangleleft$ $\dot{\Gamma} = 3.0$, $*$ $\dot{\Gamma} = 5.0$. In these simulations, $N_b = 2$, $b = 25$, $z = 1$, $d^\star = 0.93$, and $c/c^\star = 0.176$.

We anticipate that with increasing flow strength Wi, the polymer size $\langle R_e^2 \rangle$

will increase, regardless of the value of χ. This is indeed the case, as displayed in Fig. 4.7 (a). Since a polymer chain tumbles continuously in shear flow while undergoing exponential stretching in extensional flows, the change in $\langle R_e^2 \rangle$ will become more pronounced as the value of χ changes from 0 to 1, over a similar range of values of Wi. This behaviour is evident in Fig. 4.7 (c).

The behaviour of η displayed in Figs. 4.7 (b) and (d) demonstrates the existence of a critical value of the mixedness parameter, χ_c, such that for $\chi < \chi_c$, the flow is shear dominated, while being extension dominated for values of $\chi > \chi_c$. For instance, as can be seen from Fig. 4.7 (b), the viscosity *decreases* with increasing flow strength at $\chi = 0$, while *increasing* with Wi for all values of $\chi > 0.04$. At $\chi = 0.04$, the viscosity appears to be nearly independent of flow strength. The precise value of χ_c will be discussed in greater detail shortly below, however, the alteration in the variation of η with Wi can be seen more dramatically in Fig. 4.7 (d), where the viscosity appears to be shear thinning for values of χ close to 0, but extension hardening for all large values of χ.

The existence of a critical mixedness parameter in mixed flows of dilute polymer solutions was first demonstrated by Woo and Shaqfeh (2003), who also proposed an explanation for the significant change in behaviour observed in the response of the solution for values of χ on either side of χ_c. They argued that when a molecule, which is aligned along the extension axis, undergoes thermal fluctuations, it suffers a tumbling like motion if it is displaced sufficiently by a fluctuation to end up being aligned along the contraction axis. This can only happen if the angle between the extension and contraction axis is not too large. As can be seen from Fig. (4.1) and Eq. (4.1), the magnitude of the angle between the axis is determined by χ, since in terms of χ, $\beta = \cos^{-1}\left[(1-\chi)/(1+\chi)\right]$. Since β increases with increasing χ, the critical value χ_c determines when the angle is too large for thermal fluctuations to cause a molecule to hop from being aligned along the extension axis to being aligned along the contraction axis. Shaqfeh and co-workers have also discussed the scaling of χ_c with chain length N_b (Woo and Shaqfeh, 2003; Hoffman and Shaqfeh,
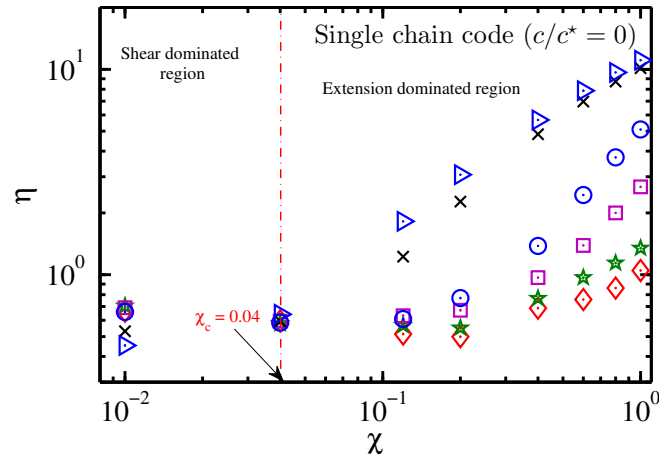
(a)
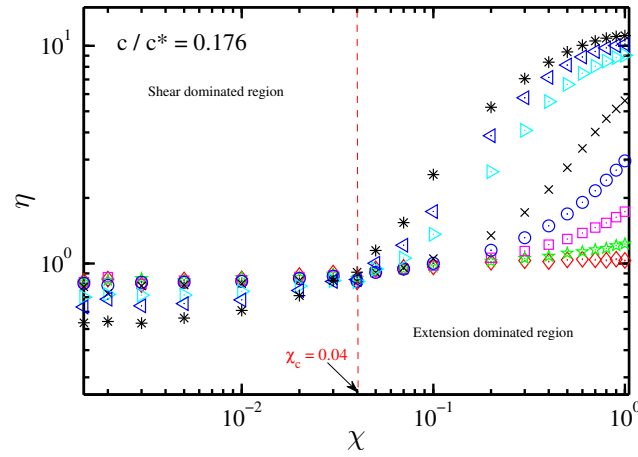
(b)
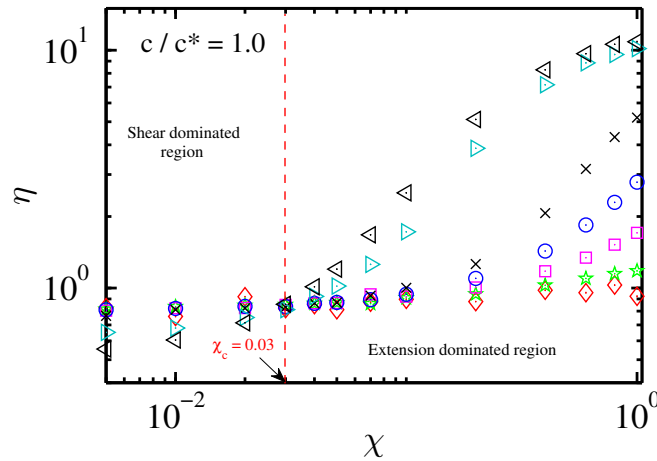
(c)

FIGURE 4.8: Demonstration of the existence of a critical mixedness parameter, χ_c, in planar mixed flows. The flow is shear dominated for $\chi < \chi_c$, while being extension dominated for values of $\chi > \chi_c$. (a) Variation of η with χ for a dilute solution: $\diamond$ $\dot{\Gamma} = 0.1$, $\star$ $\dot{\Gamma} = 0.4$, $\square$ $\dot{\Gamma} = 0.7$, $\circ$ $\dot{\Gamma} = 1.0$, $\times$ $\dot{\Gamma} = 3.0$, $\triangleright$ $\dot{\Gamma} = 5.0$; (b) Variation of η with χ at $c/c^* = 0.176$: $\diamond$ $\dot{\Gamma} = 0.1$, $\star$ $\dot{\Gamma} = 0.3$, $\square$ $\dot{\Gamma} = 0.5$, $\circ$ $\dot{\Gamma} = 0.7$, $\times$ $\dot{\Gamma} = 1.0$, $\triangleright$ $\dot{\Gamma} = 2.0$, $\triangleleft$ $\dot{\Gamma} = 3.0$, $*$ $\dot{\Gamma} = 5.0$; (c) Variation of η with χ at $c/c^* = 1.0$: $\diamond$ $\dot{\Gamma} = 0.1$, $\star$ $\dot{\Gamma} = 0.3$, $\square$ $\dot{\Gamma} = 0.5$, $\circ$ $\dot{\Gamma} = 0.7$, $\times$ $\dot{\Gamma} = 1.0$, $\triangleright$ $\dot{\Gamma} = 3.0$, $\triangleleft$ $\dot{\Gamma} = 5.0$. In these simulations, $N_b = 2$, $b = 25$, $z = 1$, and $d^\star = 0.93$.
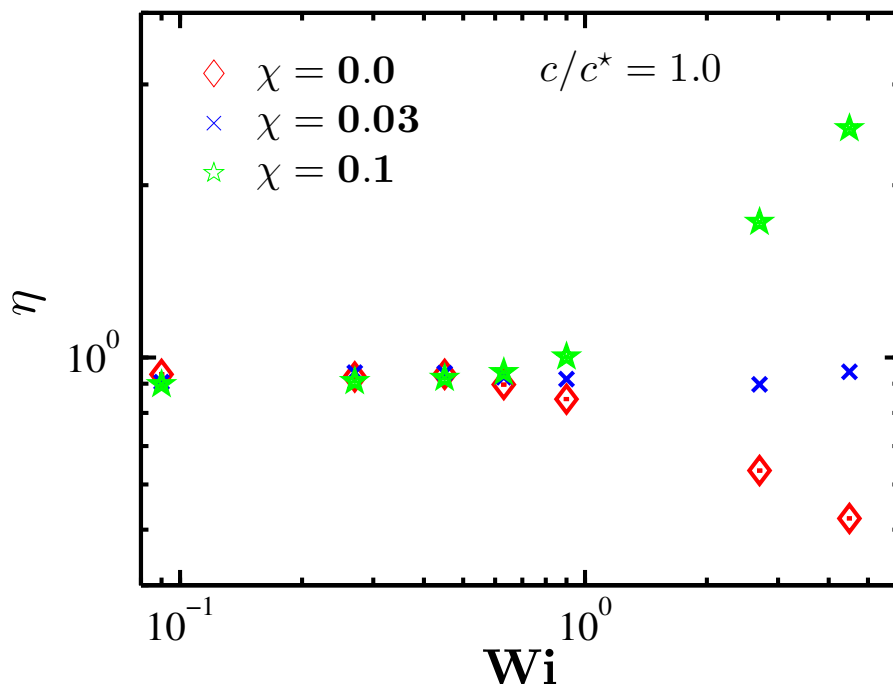
FIGURE 4.9: The dependence of viscosity on flow strength at $c/c^* = 1$, for three values of the mixedness parameter: $\diamond\ \chi = 0$, $\star\ \chi = 0.1$, and $\times\ \chi_c = 0.03$.

2007). However, they have not examined the dependence of χ_c on c/c^*, since they confined their attention to dilute solutions.

A close observation of the change of η with χ in Fig. 4.7 (d), at small values of χ, appears to suggest that the curves for the various values of Wi cross each other at a unique value of χ. A zoomed in version of the behaviour in this region is displayed in Figs. 4.8 (a) to (c), for dilute solutions, and at two non-zero values of c/c^*, respectively. The existence of a critical mixedness parameter that demarcates a shear dominated from an extension dominated regime is very clearly demonstrated in these figures. Interestingly, at all concentrations, the value of χ_c is independent of the flow strength Wi, and the value of η is constant, independent of Wi, at $\chi = \chi_c$. However, the value of χ_c appears to decrease weakly with an increase in c/c^*, from $\chi_c \approx 0.04$, both for dilute solutions and at $c/c^* = 0.176$, to $\chi_c \approx 0.03$ at $c/c^* = 1$. This can be understood as arising from a decrease in the fluctuations of the polymer coil perpendicular to the extension axis, due to a crowding of molecules with increasing concentration. We can anticipate that the

influence of concentration will become more significant for $c/c^* > 1$, when polymer coils begin to interact more strongly with each other. However, a more detailed study of changes in the fluctuations in polymer conformations, and the alignment of molecules relative to the extension and contraction axis, with changes in concentration, is required before a more complete understanding of this observation can be achieved.

The constancy of η with Wi, when $\chi = \chi_c \approx 0.03$, can be seen more clearly in Fig. 4.9, where the dependence of η on Wi is examined, at $c/c^* = 1$, for three values of χ, with two of the values ($\chi = 0$ and $\chi = 0.1$), lying on either side of $\chi_c \approx 0.03$. As discussed earlier, the definition of the viscosity in Eq. (2.21) given in Chapter 2, ensures that it approaches the Newtonian value for $\dot{\gamma} \to 0$, and $\dot{\epsilon} \to 0$. As a result, we expect it to asymptote to the Newtonian value at all values of χ, in the limit of $Wi \to 0$. This is indeed observed in Fig. 4.9 as $Wi \to 0$. At higher values of Wi, the value of χ determines whether there is shear thinning or extension thickening. At the critical value χ_c, however, the solution *remains* Newtonian, independent of Wi. This would suggest that in any ensemble of molecules, there are a proportion of molecules undergoing tumbling motions and alignment, and a proportion of molecules undergoing unravelling from coiled to stretched states, such that the net effect is no change of viscosity with increasing deformation rate. Further studies are definitely warranted to verify if this is indeed the case.

4.4 Conclusion

In this study, simulation results have been obtained with a multi-chain BD algorithm on the viscosity of polymer solutions at finite concentrations, when subjected to planar mixed flow. The fascinating behaviour exhibited in these flows, as demonstrated by the various results reported here, has so far not been examined experimentally. In particular, proving the existence of the critical mixedness

parameter, and exploring the influence of concentration and chain length in determining its value, would be of great interest. In the context of simulations, determining the scaling of χ_c with concentration, solvent quality, and chain length, and establishing the correlation between χ_c and the existence of coil-stretch hysteresis would be extremely valuable. For dilute polymer solutions, it is well known that the size of the coil-stretch hysteresis window observed in planar mixed flows is significantly influenced by the value of the mixedness parameter, vanishing as $\chi \to 0$, and having a maximum at $\chi \to 1$. Studying the dynamics of coil-stretch hysteresis under a variety of circumstances, including varying the concentration, solvent quality and chain length, would provide a fundamental understanding of the hysteresis phenomenon in particular, and of the behaviour of polymer solutions at finite concentrations, in general. The present mesoscopic BD algorithm makes it possible to carry out such studies.

Chapter 5

Parameter-free prediction of DNA dynamics in planar extensional flow of semidilute solutions

5.1   Introduction

Several studies of single molecules of fluorescently labelled DNA have been carried out in order to gain insight into the conformational evolution of polymer chains when subjected to a variety of flow fields (Marciel and Schroeder, 2013; Mai et al., 2012; Chu, 1991; Perkins et al., 1994b; Smith and Chu, 1998; LeDuc et al., 1999; Smith et al., 1999; Babcock et al., 2003; Perkins et al., 1994c; Quake et al., 1997; Smith et al., 1995; Huber et al., 2014; Smith et al., 1996; Perkins et al., 1995; Babcock et al., 2000; Harasim et al., 2013; Schroeder et al., 2003; Teixeira et al., 2007; Wirtz, 1995). These studies have not only enabled the direct visual observation of "molecular individualism" (Gennes, 1997; Smith and Chu, 1998), but have also proved to be of vital importance for the validation of molecular theories of polymer dynamics (Shaqfeh, 2005; Sunthar and Prakash, 2005; Larson and Hu, 1999; Jendrejack et al., 2002; Hsieh et al., 2003; Schroeder et al., 2004b; Smith et al., 1995; Hur et al., 2001; Smith et al., 1996; Robertson and Smith, 2007). Nearly all these investigations have been carried out in either the dilute or concentrated

solution regimes, with only a few in the semidilute regime (Hur et al., 2001; Babcock et al., 2000; Harasim et al., 2013; Huber et al., 2014; Liu et al., 2009). Given the importance of semidilute polymer solutions, both from a fundamental and a practical (Ramakrisna et al., 2005; Gans et al., 2004; Kozer et al., 2007) point of view, it is essential to gain an understanding of the fundamental physics that govern the dynamics of polymer molecules in this regime. In the dilute regime, single molecules studies have revealed the importance of properly accounting for hydrodynamic and excluded volume interactions in molecular theories (Shaqfeh, 2005; Sunthar and Prakash, 2005; Larson and Hu, 1999; Jendrejack et al., 2002; Hsieh et al., 2003; Schroeder et al., 2004b). In semidilute solutions, however, it is known that these interactions gradually get screened with increasing monomer concentration (Gennes, 1979; Rubinstein and Colby, 2003; Jain et al., 2012a). The recent single molecule experiments of Hsiao et al. (2016) on planar extensional flow of unentangled semidilute solutions of λ-phage DNA, provide benchmark data against which molecular theories can be verified. In particular, one can examine if theories accurately capture the subtle changes that occur on the molecular scale, as chains begin to interact and interpenetrate with each other with increasing concentration. The aim of this chapter is to carry out simulations with the present multi-chain Brownian dynamics algorithm (Jain et al., 2012b; Jain et al., 2015), which incorporates hydrodynamic and excluded volume interactions in order to compare predictions with experimental observations. Additionally, the technique of successive fine-graining (Sunthar and Prakash, 2005; Prabhakar et al., 2004) is used to obtain predictions that are independent of model parameters.

Over the past two decades, DNA (and in particular, λ-phage DNA) has been used as model polymer to carry out a number of investigations into single molecule dynamics. The advantage of DNA lies in the monodispersity of the solutions, and the ease with which the molecules can be stained with a dye for visual observation (Pecora, 1991). For instance, in dilute solutions, single molecule studies of DNA have been used to examine the stretching dynamics of DNA molecules in

extensional flows (Perkins et al., 1997; Smith and Chu, 1998), stretching and tumbling dynamics in shear flows (LeDuc et al., 1999; Smith et al., 1999), dynamics in mixed shear and extensional flows (Babcock et al., 2003), direct measurements of diffusion coefficients (Wirtz, 1995; Robertson and Smith, 2006) and relaxation times (Perkins et al., 1994c), and to establish the existence of coil-stretch hysteresis (Schroeder et al., 2003). In concentrated solutions, single molecule studies have established the validity of the reptation hypothesis (Perkins et al., 1994a) and of scaling theories for the molecular weight dependence of diffusion coefficients (Smith et al., 1995). Compared to the wealth of experimental information on single molecule dynamics in the dilute and concentrated regimes, there is comparatively little information on the behavior of macromolecules in the semidilute regime, both under equilibrium and non-equilibrium conditions. The classic early work of Chu and co-workers (Hur et al., 2001; Babcock et al., 2000) was the first attempt to relate macroscopic rheological behavior to microscopic dynamics in shear flows. Steinberg and co-workers have measured the longest relaxation times for semidilute solutions of T4 DNA by carrying out stretch relaxation experiments (Liu et al., 2009). More recently, Bausch and co-workers (Harasim et al., 2013; Huber et al., 2014) have correlated the dynamics of semiflexible polymers in semidilute solutions to the measured dependence of viscosity on shear rate in semidilute solutions. To our knowledge, there appear to be no measurements of single molecule dynamics in extensional flows of unentangled semidilute solutions, prior to the recent work of Hsiao et al. (2016). It is also worth noting that experiments on single molecule behavior in extensional flows of dilute solutions have either separately examined the unravelling of chains from the coiled to the stretched state (Perkins et al., 1997; Smith and Chu, 1998; Schroeder et al., 2003), or the relaxation from the stretched to the coiled state (Perkins et al., 1994b; Schroeder et al., 2003). The experiments of Hsiao et al. (2016) are unique in that they document the response of single chains to step-strain deformation followed by cessation of flow, both in the dilute and semidilute regime, and provide an opportunity to validate simulation

predictions of chain stretch and relaxation in a single experiment.

In the case of dilute polymer solutions undergoing extensional flow, several studies have shown that it is necessary to incorporate the finite extensibility of chains, and the presence of hydrodynamic and excluded volume interactions into molecular theories in order to obtain an accurate prediction of experimental measurements (Shaqfeh, 2005; Larson, 2005; Larson and Hu, 1999; Jendrejack et al., 2002; Hsieh et al., 2003; Schroeder et al., 2004b; Prabhakar et al., 2004). In addition to having to choose the level of coarse-graining through a choice of the number of beads in a bead-spring chain, N_b, the incorporation of these phenomena entails the choice of parameters associated with each of them when carrying out simulations. Thus a choice needs to be made for the values of the nondimensional finite extensibility parameter, b, the nondimensional bead radius, h^*, which is a measure of the strength of hydrodynamic interactions, and the nondimensional excluded volume parameter, z^*, which is a measure of the difference between the solution temperature and the theta temperature. Prakash and co-workers (Sunthar and Prakash, 2005; Prabhakar et al., 2004; Pham et al., 2008) have shown that by using the method of successive fine-graining, predictions can be obtained that are independent of the choice of parameters in the model. The successive fine-graining technique is a specific protocol by which simulation data acquired for bead-spring chains with increasing values of N_b, is extrapolated to the number of Kuhn steps N_k in the polymer chain being simulated. It essentially exploits the universal behavior observed in solutions of long chain polymers, to obtain parameter free simulation predictions. In dilute solutions, the use of successive fine-graining has been shown to lead to quantitatively accurate predictions of the conformational evolution of λ-phage DNA in cross-slot cells (Sunthar and Prakash, 2005) and the extensional viscosity of both DNA (Sunthar et al., 2005) and polystyrene solutions (Prabhakar et al., 2004; Saadat and Khomami, 2015b) in uniaxial extensional flows. The aim of the present paper is to use the successive fine-graining technique to predict the conformational evolution of DNA molecules in unentangled semidilute

solutions when subjected to step-strain deformation followed by cessation of flow, and to verify if accurate predictions of the experimental measurements of Hsiao *et al.* (Hsiao et al., 2016) can be obtained.

Several different mesoscopic simulation techniques have been developed over the past decade for describing the dynamics of unentangled semidilute polymer solutions which take into account the presence of intra and intermolecular long-range hydrodynamic interactions (Ahlrichs et al., 2001; Dünweg and Ladd, 2009; Huang et al., 2010; Stoltz et al., 2006; Jain et al., 2012b; Saadat and Khomami, 2015a). By implementing the Kraynik-Reinelt periodic boundary conditions for mixed flows (Kraynik and Reinelt, 1992; Hunt et al., 2010), Prakash and co-workers (Jain et al., 2015) have recently developed an optimized multi-particle Brownian dynamics algorithm that can simulate arbitrary planar mixed shear and extensional flows of polymer solutions at finite concentrations, a summary of which is presented in Chapter 4. This algorithm is used in the present work to implement the successive fine-graining technique in the context of planar extensional flows.

The structure of this chapter is as follows. In Section 5.2, the governing equations for a bead-spring chain model along with the definitions of various observable quantities, are given. In Section 5.3, a brief overview of the successive fine-graining technique is presented. A detailed comparison of simulation predictions with the experimental observations of Hsiao et al. (2016), in dilute and in semidilute solutions, is presented in Section 5.4. In particular, we carry out a qualitative comparison of the probability distribution of fractional stretch in planar extensional flows, and a quantitative comparison of the conformational evolution of single chains subjected to a step-strain deformation followed by cessation of flow. Finally, in Section 5.5, we summarise the principal conclusions of this work.

5.2   Bead-spring chain model of DNA

A bead-spring chain model is used to represent DNA molecules whereby each molecule is coarse-grained into a sequence of N_b beads (which act as centers of hydrodynamic resistance) connected by $N_b - 1$ massless springs that represent the entropic force between two adjacent beads. A semidilute solution of DNA molecules is obtained by immersing an ensemble of such bead-spring chains in an incompressible Newtonian solvent. The non-dimensional governing equation to track each bead of DNA molecule with time for the present multi-chain BD simulations is the Ito stochastic differential equation based on the Euler integration scheme as presented by Eq. 2.1 in Chapter 2. Hydrodynamic interactions, caused by the movement of one DNA molecule (intermolecular) or by segments of it (intramolecular), are treated with the Rotne-Prager-Yamakawa tensor as described in detail in Section 2.4 of Chapter 2. A wormlike chain (WLC) model, widely used to represent a variety of molecules ranging from biomacromolecules like DNA to wormlike micelles (Bastamante et al., 1994), is used to represent the spring force acting between two beads as given in non-dimensional form by Eq. 2.6 in Section 2.3 of Chapter 2. In this chapter, we present all the numerical non-dimensional length and time units with a star over the variable in order to distinguish them from experimental dimensional variables.

DNA solutions used in rheological measurements are typically good solvents that lie in the crossover regime between θ solutions and athermal solvents, with the solvent quality described by the variable (Pan et al., 2014a; Pan et al., 2014b),

$$z = k \left(1 - \frac{T_\theta}{T} \right) \sqrt{M} \tag{5.1}$$

where, M is the molecular weight, T_θ is the theta temperature, and k is a polymer-solvent chemistry dependent constant. Recently, Pan *et al.* have estimated that $T_\theta \approx 15C$ for the DNA solutions that are typically used in rheological experiments, and have also determined the value of the constant k (Pan et al., 2014a; Pan et

al., 2014b). In particular, they have tabulated the value of z as a function of temperature and molecular weight for a wide variety of DNA fragments. Based on their calculations, a solution of λ-phage DNA is estimated to have a solvent quality $z \approx 0.7$ at 22^0C (the temperature at which the experiments reported in Hsiao et al. (2016) have been carried out). Interestingly, Sunthar *et al.* (Sunthar and Prakash, 2005; Sunthar et al., 2005) found that using $z = 1$ in their dilute solution simulations gave the best agreement between predictions and experimental measurements (within simulation and experimental error bars). For these reasons, we use $z = 1$ in all the current simulations.

The solvent quality can be conveniently controlled in simulations with the help of the narrow Gaussian potential as presented by Eq. 2.10 in Chapter 2, which determines the force due to excluded volume interactions between any two beads μ and ν. This potential is characterized by the strength of the excluded volume interactions, z^* and the range of the interaction, d^*. A mapping between experiments and simulations is achieved by setting $z = z^* \sqrt{N_b}$, with z^* being a measure of the departure from the θ-temperature, and N_b being proportional to the molecular weight (Kumar and Prakash, 2003; Sunthar and Prakash, 2006). As a result, for any choice of N_b, z^* is chosen to be equal to $z/\sqrt{N_b}$ such that the simulations correspond to the given experimental value of z.

The velocity gradient tensor for planar extensional flows is given by (Bird et al., 1987a)

$$(\boldsymbol{\nabla v})_{\text{PEF}} = \begin{pmatrix} \dot{\epsilon}^* & 0 & 0 \\ 0 & -\dot{\epsilon}^* & 0 \\ 0 & 0 & 0 \end{pmatrix} \tag{5.2}$$

where, $\dot{\epsilon}^*$ is the elongation rate. Planar extensional flows are generally difficult to study by computer simulations, since fluid elements are exponentially stretched in one direction and contracted in the perpendicular direction. This leads to a very short window of time to observe the dynamics of single molecules since the

dimensions of the simulation box rapidly become of order of intermolecular distance. This difficulty can be resolved by the implementation of Kraynik-Reinelt periodic boundary conditions (Kraynik and Reinelt, 1992; Todd and Daivis, 1998; Baranyai and Cummings, 1999). As mentioned earlier, Jain et al. (2015) have implemented these boundary conditions for BD simulations in the context of arbitrary planar mixed flows and this algorithm has been adopted here. A summary of the implementation can also be found in Chapter 3.

Simulation predictions are compared with the experimentally measured *stretch* of molecules, when a semidilute solution is subjected to a step-strain deformation in a planar extensional flow. The stretch of a fluorescently dyed DNA molecule, measured in a cross-slot cell, is the projected extent of the molecule in the flow direction. For a bead-spring chain model, this is calculated from,

$$X^*_{\max} \equiv \max_{\mu, \nu} |r^{*x}_\mu - r^{*x}_\nu| \tag{5.3}$$

where, r^{*x}_μ is the x-component of the vector $\mathbf{r}^*_\mu$, with x being the direction of flow. The mean stretch can be obtained from the bead positions in an ensemble of chain configurations from the ensemble average,

$$\bar{X}^* = \langle X^*_{\max} \rangle \tag{5.4}$$

The equilibrium mean stretch is denoted by $\bar{X}^*_{\mathrm{eq}}$. Experimental measurements of stretch are typically reported in terms of the nondimensional ratio $\bar{X}/L$. However, we often find it convenient to additionally use the expansion ratio,

$$E = \frac{\bar{X}^*}{\bar{X}^*_{\mathrm{eq}}} \tag{5.5}$$

in simulations.

The longest relaxation time λ_1 is measured experimentally by fitting the terminal 30% of the stretch of a molecule, as it relaxes from a highly extended state,

with a single exponential decay (Hsiao et al., 2016). In simulations, the longest nondimensional relaxation time $\lambda_1^* = \lambda_1/\lambda_H$, for any bead-spring chain with N_b beads, is obtained by initially stretching each chain to nearly 90% of its fully extended state, and letting it relax to equilibrium. The tail of the decay of the nondimensional stretch $\bar{X}^*$ as a function of nondimensional time t^* is then fitted with a single exponential function of the following form,

$$\bar{X}^*(t^*) = \bar{X}_\infty^* + \left(\bar{X}_0^* - \bar{X}_\infty^*\right) e^{-t^*/\lambda_1^*} \tag{5.6}$$

where, $\bar{X}_0^*$ and $\bar{X}_\infty^*$ are the initial value and the final value (after the chain has fully relaxed) of stretch, respectively, to which the fit is carried out. All three parameters, $\bar{X}_0^*, \bar{X}_\infty^*$ and λ_1^* are determined from the fit. As expected, the value of $\bar{X}_\infty^*$ is close to that of $\bar{X}_{\text{eq}}^*$. However, it should be noted that the latter value is obtained from carrying out a static ensemble average from an equilibrium simulation, after the trajectories have reached a stationary state, as described in Jain (2013). In the section below, we briefly summarize the technique of successive fine-graining, which is used to obtain parameter free predictions of the stretch of DNA in extensional flows.

5.3 Successive fine-graining

The successive fine-graining technique exploits the universal behavior of polymer solutions to obtain property predictions that are independent of the choice of model parameters. At equilibrium, this technique has been widely used to obtain universal predictions from analytical theories and molecular simulations (Zimm, 1980; Kumar and Prakash, 2003; Torre et al., 1984; Freire et al., 1986; García Bernal et al., 1991; Sunthar and Prakash, 2006; Pan et al., 2014b; Jain et al., 2012a). Essentially, data is accumulated for finite chains, and subsequently extrapolated to the long chain limit, $N_b \to \infty$, where the self-similar character of polymer chains is

captured. Extrapolation to the long chain limit has also been used to obtain universal predictions in shear flow, where the finiteness of chain length is not relevant for sufficiently long chains at typically measured shear rates (Kröger et al., 2000; Öttinger, 1987; Öttinger, 1989; Prakash and Öttinger, 1997; Prakash, 2002b; Kumar and Prakash, 2004b). In extensional flows, however, where at high extension rates chains are nearly fully stretched, the finiteness of chain length plays a crucial role in determining the solutions properties. Even under these circumstances, provided the flow has not 'penetrated' below the Pincus blob length scale, universal behavior is still observed (Sunthar and Prakash, 2005; Somani et al., 2010). Prakash and co-workers have modified the successive fine-graining technique for infinitely long chains, by making it applicable under circumstances where it is important to account for the finite length of a chain (Sunthar and Prakash, 2005; Prabhakar et al., 2004; Pham et al., 2008; Bosko and Prakash, 2011). While at its core, the modification consists of changing the extrapolation limit from $N_b \to \infty$ to $(N_b - 1) \to N_k$, where, N_k is the number of Kuhn steps in the underlying chain, the details of the method are more subtle and complex. Sunthar and Prakash have discussed the procedure in great detail in Sunthar and Prakash, 2005. For the sake of completeness, we briefly motivate and explain the salient features of the technique below.

An example of a universal equilibrium property for dilute polymer solutions under θ conditions is the Flory-Fox constant $U_{\eta R}^{\theta}$, defined by (Rubinstein and Colby, 2003),

$$U_{\eta R}^{\theta} = \frac{[\eta]_{\theta} M}{(4\pi/3) \left(R_g^{\theta} \right)^3 N_A} \tag{5.7}$$

where, $[\eta]_{\theta}$ is the zero shear rate intrinsic viscosity, and N_A is Avagadro's constant. It is a surprising experimental observation that $U_{\eta R}^{\theta}$ attains its universal value of 1.49 ± 0.06 for a wide range of polymer-solvent systems (Miyaki et al., 1980), for molecular weights as low as $M = 50,000$ g/mol (Krigbaum et al., 1952; Krigbaum and Flory, 1953). As a result, it is clear that the intrinsic viscosity at the θ

temperature for a majority of dilute polymer solutions can be calculated once the radius of gyration of the polymer under θ conditions is known. For polymer solutions in the crossover region between θ and very good solvents, an additional variable, namely the solvent quality parameter z is required to describe universal behavior. For instance, for a number of different polymer-solvent systems, the ratio,

$$\alpha_\eta(T, M) = \left(\frac{[\eta]}{[\eta]_\theta} \right)^{1/3} \tag{5.8}$$

measured at different temperatures and molecular weights, is found to collapse onto a master plot, when plotted as a function of z (Tominaga et al., 2002; Pan et al., 2014b). Since,

$$[\eta](T, M) = [\eta]_\theta \, \alpha_\eta^3 = U_{\eta R}^\theta \left(\frac{N_A}{M} \right) \left(\frac{4\pi}{3} R_g^\theta \right)^3 [\alpha_\eta(z)]^3 \tag{5.9}$$

it is clear that a knowledge of R_g^θ, and the universal properties $U_{\eta R}^\theta$ and $\alpha_\eta(z)$, enables the determination of the intrinsic viscosity of any dilute solution of linear flexible polymers in the crossover regime. A similar argument can be made for any other static or dynamic property of a dilute polymer solution, $\phi(T, M)$. Essentially, provided one knows a suitably defined universal ratio $U_{\phi R}^\theta$ under θ conditions, and the universal crossover swelling function $\alpha_\phi(z) = \phi(z)/\phi_\theta$, the property ϕ can be determined for the solution at any temperature and polymer molecular weight, given R_g^θ and z. This is the basic content of the two-parameter theory (Yamakawa, 1971), which states that all static and dynamic properties of a dilute solution of linear flexible polymers can be determined once R_g^θ and z are known.

Bead-spring chain models with Hookean springs need three parameters $\{N_b, h^*, z^*\}$, to be specified, when nondimensionalized with the length scale l_H, and time scale λ_H. While the strength of hydrodynamic interactions is specified by the draining parameter (Zimm, 1956; Öttinger and Rabin, 1989), $h = h^* \sqrt{N_b}$, the strength of excluded volume interactions (Schäfer, 2012; Prakash, 2001a) is determined by

$z = z^* \sqrt{N_b}$. Typically, the parameters h^* and z are kept constant when implementing the successive fine-graining procedure of extrapolating finite chain data to the long chain limit, $N_b \to \infty$ (Zimm, 1980; Kumar and Prakash, 2003; Freire et al., 1986; García Bernal et al., 1991; Sunthar and Prakash, 2006; Pan et al., 2014b; Jain et al., 2012a; Kröger et al., 2000; Öttinger, 1987; Öttinger, 1989; Prakash and Öttinger, 1997; Prakash, 2002b). This implies that universal property predictions at equilibrium and in shear flow are obtained in the non-draining limit $h \to \infty$ (independent of the particular choice made for h^*), and at a specific location in the crossover regime specified by the solvent quality z.

The modified successive fine-graining procedure for polymer solutions in extensional flows (Sunthar and Prakash, 2005; Prabhakar et al., 2004) also leads to universal predictions in the limit of large h and constant z. However, the use of finitely extensible springs in place of Hookean springs, in order to account for finite chain length, leads to significant changes in the implementation of the procedure.

When subjected to extensional flow, a dilute polymer solution in the crossover regime is characterized by the following set of variables: $\left\{ R_g^\theta, z, L, Wi, \epsilon \right\}$. Here, L is the finite contour length of the chain, $Wi = \lambda_1 \dot{\epsilon}$ is the nondimensional Weissenberg number, with $\dot{\epsilon}$ being the extension rate, and $\epsilon = \dot{\epsilon} t$ the Hencky strain, which measures the extent of deformation from the onset of flow. The protocol for successive fine-graining of finite chains described briefly below, ensures that universal property predictions are obtained for this set of prescribed experimental variables.

The maximum number of conformational degrees of freedom for a finite chain is the number of Kuhn steps, N_k. Extrapolation of finite chain data can consequently only be carried out to the limit $(N_b - 1) \to N_k$. The number of Kuhn steps in a flexible linear chain can be determined from the expression,

$$N_k = \frac{L^2}{6(R_g^\theta)^2} \tag{5.10}$$

While the θ temperature for DNA in aqueous solutions with excess sodium salt (typically used for cross slot flow measurements), has been shown to be roughly 15°C by Pan *et al.* (Pan et al., 2014a), there does not yet seem to be an accurate measurement of R_g^θ. In the absence of information on R_g^θ, N_k can also be found from the expression $N_k = L/(2\lambda_p)$, where, λ_p is the persistence length. In Appendix B of Pan et al. (2014a), they have reported measurements of λ_p by various authors, using a variety of different techniques, to be roughly 50 nm. As a result, using a contour length of 16 μm, suggests $N_k = 160$. On the other hand, staining with YOYO-1 dye is known to increase the contour length (Perkins et al., 1997; Smith and Chu, 1998). Recent experiments by the Doyle group (Kundukad et al., 2014) suggest that while the contour length is increased by 38% at full saturation of one YOYO-1 per four base pairs of DNA, the persistence length is unchanged. For λ-phage DNA, this implies a stained contour length of 22 μm, in agreement with earlier estimates (Perkins et al., 1997; Smith and Chu, 1998). The number of Kuhn steps would then be roughly $N_k = 220$. Sunthar and Prakash (2005) have argued that results of the successive fine-graining procedure are insensitive to a choice of N_k in the range 150-300, and have used $N_k = 200$ in their simulations of dilute λ-phage DNA solutions subjected to extensional flow. We adopt the same value in the current simulations.

The centrality of the finiteness of chain length is maintained in the successive fine-graining procedure by ensuring that at every level of coarse-graining, the fully stretched length of the bead-spring chain is identical to the contour length of the polymer being modelled. As a consequence, for any choice of the number of beads N_b,

$$L = (N_b - 1)\sqrt{b}\,l_H \tag{5.11}$$

In order to be consistent with the equilibrium properties of the polymer, it is also required that the radius of gyration of the bead-spring chain under θ conditions remains unchanged with fine-graining. If the diemnsional mean-square end-to-end

vector, $\langle Q^2 \rangle$, of a single finitely extensible spring in the bead-spring chain is written as,

$$\langle Q^2 \rangle = 3\, l_H^2\, \chi^2(b) \tag{5.12}$$

with the quantity $\chi(b)$ being defined by this expression, then it is straight forward to show that (Bird et al., 1987b; Sunthar and Prakash, 2005)

$$\left(R_g^\theta\right)^2 = \chi^2(b)\, \frac{(N_b^2 - 1)}{2N_b}\, l_H^2 \tag{5.13}$$

Evaluating the ratio, $L^2/\left(R_g^\theta\right)^2$, from Eqs. 5.11 and 5.13, and using the definition of N_k in Eq. 5.10 implies,

$$\frac{b}{\chi^2(b)} = \frac{3(N_b + 1)}{N_b(N_b - 1)} N_k \tag{5.14}$$

Sunthar and Prakash (2005) have shown that for wormlike chains,

$$\frac{\chi^2(b)}{b} = \frac{1}{3} \frac{\int_0^1 dq^*\, q^{*4}\, e^{-\phi^*(b,q^*)}}{\int_0^1 dq^*\, q^{*2}\, e^{-\phi^*(b,q^*)}} \tag{5.15}$$

where, ϕ^* is the nondimensional spring potential,

$$\phi^*(b, q^*) = \frac{b}{6} \left[2\, q^{*2} + \frac{1}{1 - q^*} - q^* \right] \tag{5.16}$$

These arguments enable the determination of the finite extensibility parameter b, and the nondimensional mean square length of a single spring $\chi^2(b)$, at any level of coarse-graining. A simple and efficient procedure for calculating both b and $\chi^2(b)$ has been described in Sunthar and Prakash (2005), for any choice of N_b and N_k.

The quantity $\chi^2(b)$ also plays an important role in the treatment of hydrodynamic and excluded volume interactions in the successive fine-graining procedure. For a bead-spring chain with finitely extensible springs, the draining parameter can be shown to be given by the expression (Sunthar and Prakash, 2005), $h = \tilde{h}^* \sqrt{N_b}$,

where,

$$\tilde{h}^* = \frac{h^*}{\chi(b)} \tag{5.17}$$

while the solvent quality can be shown to be given by Sunthar and Prakash (2005), $z = \tilde{z}^*\sqrt{N_b}$, where,

$$\tilde{z}^* = \frac{z^*}{[\chi(b)]^3} \tag{5.18}$$

Note that $\chi(b) \to 1$ in the limit $N_b \to \infty$. When carrying out the successive fine-graining procedure for infinite chains, as mentioned earlier, the parameter h^* is held constant as $N_b \to \infty$, while z^* is calculated from $z^* = z/\sqrt{N_b}$ at each level of fine-graining. On the other hand, during the successive fine-graining procedure for finitely extensible bead-spring chains, $\tilde{h}^*$ is held constant at each level of fine-graining, which implies, $h^* = \tilde{h}^* \chi(b)$, and z^* is calculated from the expression, $z^* = \left(z/\sqrt{N_b} \right) [\chi(b)]^3$. Sunthar and Prakash (2005) and Pham et al. (2008) have shown that at equilibrium (where Wi and ϵ are not relevant variables), extrapolation of finite chain data to the limit $(N_b - 1) \to N_k$, using this procedure, leads to property predictions that are in quantitative agreement with known results for bead-rod chains with N_k rods.

In the presence of flow, if comparison of simulation predictions is being made with experimental data at particular values of Wi and ϵ, the successive fine-graining procedure ensures that at each level of coarse-graining, simulations are carried out at the same values of Wi and ϵ. This is achieved by the following series of steps. (i) For any choice of N_b, chains are stretched to nearly 90% of their fully stretched state and allowed to relax. The longest relaxation time λ_1^* (at that value of N_b) is then found by fitting a single exponential decay to the terminal 30% of the mean stretch, as described earlier in the context of Eq. 5.6. (ii) The extension rate $\dot{\epsilon}^*$ used for simulation of chains with N_b beads is then found from the expression, $\dot{\epsilon}^* = Wi/\lambda_1^*$, where, Wi is the experimental Weissenberg number. (iii) Once $\dot{\epsilon}^*$ is known for any N_b, simulations are carried out until a nondimensional time t^*, such that $\dot{\epsilon}^* t^* = \epsilon$. By maintaining Wi and ϵ identical to experimental values at each

level of fine-graining in this manner, we ensure that the extrapolated results in the limit $(N_b - 1) \to N_k$ are also at the specified experimental values.

To date, the successive fine-graining procedure for finite chains has only been used in the context of dilute polymer solutions (Sunthar and Prakash, 2005; Prabhakar et al., 2004; Pham et al., 2008; Saadat and Khomami, 2015b). Recently Jain *et al.* have extrapolated finite chain data in the semidilute regime to the long chain limit to obtain universal predictions for the ratio of semidilute to dilute single chain diffusion coefficients at various values of concentration (Jain et al., 2012a). In the present study, we use the successive fine-graining procedure for finite chains to compare simulation predictions for extensional flows of semidilute solutions with the experimental measurements of Hsiao et al. (2016).

5.4   Results and discussion

A majority of the experimental measurements by Hsiao et al. (2016) in the semidilute regime have been carried out at the scaled concentration $c/c^* = 1$. A striking early observation of single molecule experiments in dilute solutions (Smith and Chu, 1998) was the enormous variability in the transient stretching dynamics of the different molecules, a phenomena characterised by de Gennes as "molecular individualism" (Gennes, 1997). Hsiao et al. (2016) have observed a similarly wide distribution of configurations in their observation of individual molecular trajectories at $c/c^* = 1$, albeit with qualitatively different molecular conformations in semidilute solutions compared to dilute solutions. The light grey curves in Fig. 5.1 display the individual trajectories of 67 chains (with $N_b = 45$) in the main simulation box, in a simulation with parameter values reported in the figure caption. The black curve is the ensemble average over the chains. Clearly, wide variability in the manner in which chains unravel from the coiled to the stretched state is also observed in our simulations of extensional flow.
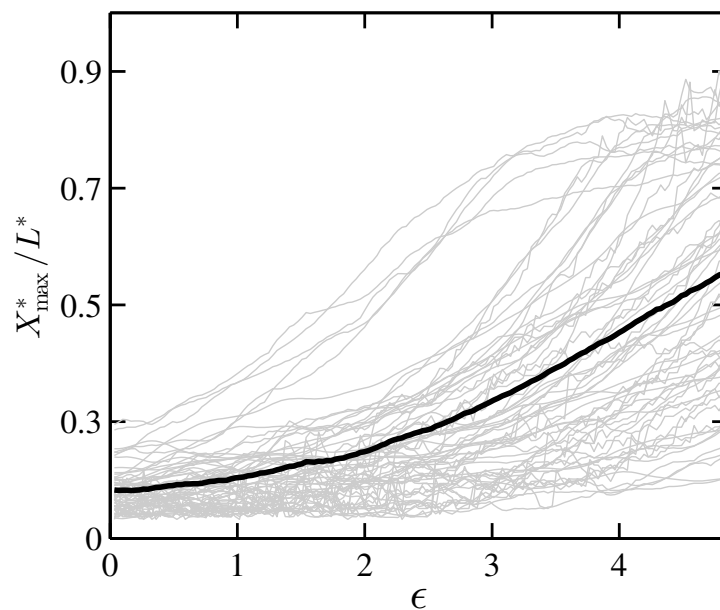
FIGURE 5.1: Evidence of molecular individualism during stretching. The light grey curves are individual trajectories of 67 chains, while the black curve is the ensemble average over the chains, i.e., $(\bar{X}/L)$. Parameter values for the simulation are: $N_b = 45$, $c/c^* = 1$, $z = 1$, $\bar{h}^* = 0.19$, $N_k = 200$ and $Wi = 2.6$.

A qualitative comparison of the probability distribution of chain extension observed in a simulation with $N_b = 45$, and the experiments of Hsiao et al. (2016), is shown in Fig. 5.2. Essentially 50 simulations, each with 67 chains in the main simulation box, were carried out and the fractional extension $(X^*_{\max}/L^*)$ for each of the chains was calculated at various values of ϵ. Here, $L^* = (N_b - 1)\sqrt{b}$. The number of chains in each of the bins, $0 \leq (X^*_{\max}/L^*) < 0.1$, $0.1 \leq (X^*_{\max}/L^*) < 0.2$, etc., was divided by 3350 (the total number of chains in the sample), to obtain the probability distribution. Note that the method of successive fine-graining has not been applied and the simulation results are at a single value of N_b. Nevertheless, a good qualitative agreement can be observed, with simulations reflecting the experimental observation of a broadening of the probability distribution as the accumulated strain increases, with the persistence of chains that remain partially unravelled even at high strains. There is some variability for fractional extension > 0.6, likely due to low sampling at these parameters in the experiments.
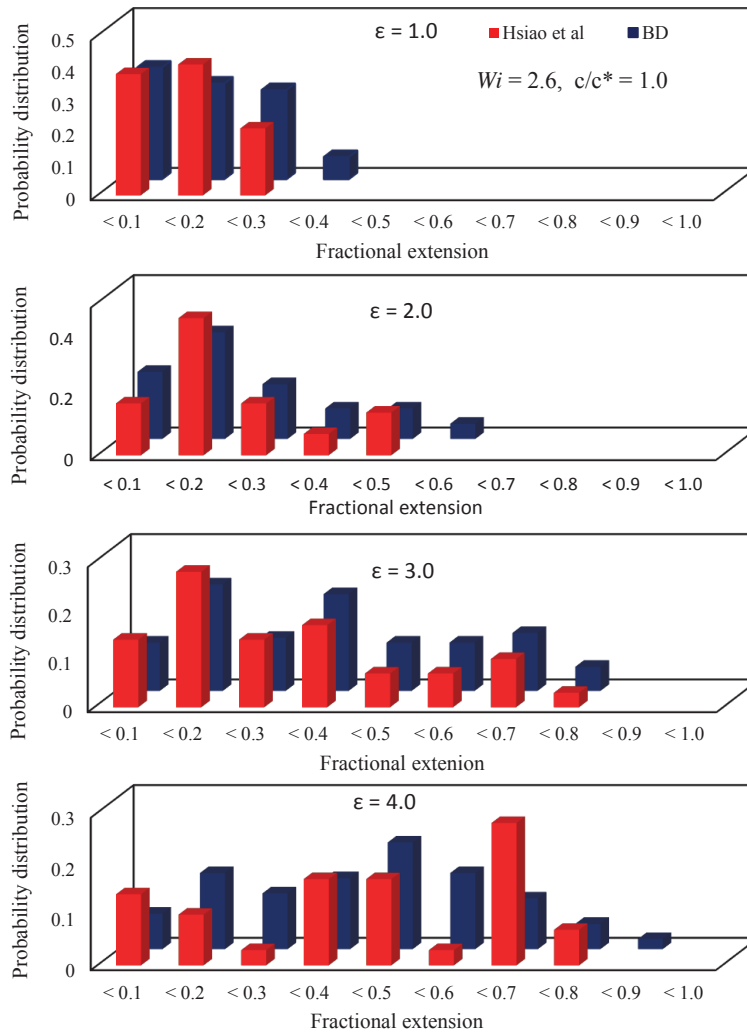
FIGURE 5.2: Probability distribution of chain extension in a semidilute solution at $c/c^* = 1$. Distributions are shown for a range of accumulated strains ϵ at a Weissenberg number $Wi = 2.6$. Red histograms are the experimental results of Hsiao et al. (2016), while the blue histogram are the results of Brownian dynamics simulations with parameter values: $N_b = 45$, $z = 1$, $\tilde{h}^* = 0.19$, and $N_k = 200$. The bins, $0 \leq (X^*_{\max}/L^*) < 0.1$, $0.1 \leq (X^*_{\max}/L^*) < 0.2$, etc., are indicated on the x-axis by the notation < 0.1, < 0.2, etc.

As mentioned earlier, the unique character of the single molecule experiments of Hsiao et al. (2016) is the implementation of a step input on the strain rate $\dot{\epsilon}$, followed by the cessation of flow once the fluid has accumulated a Hencky strain of ϵ. This enables the observation of the non-equilibrium stretching and relaxation dynamics in a single experiment. Fig. 5.3 compares the experimental measurements of the ensemble average stretch ratio E by Hsiao et al. (2016) at $c/c^* = 1$, and $Wi = 2.6$, with BD simulations carried out at various values of N_b. The flow
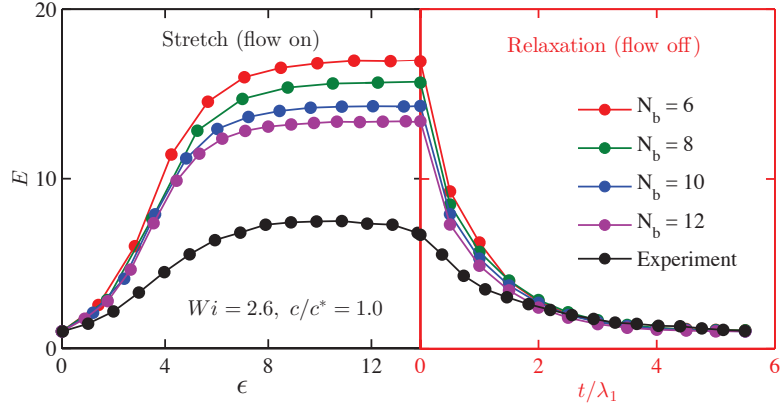
FIGURE 5.3: Transient polymer stretch in a step strain experiment in planar extensional flow at $c/c^* = 1$ and $Wi = 2.6$. The black line and symbols are experimental measurements of the ensemble average stretch ratio by Hsiao et al. (2016) and the various coloured lines and symbols are BD simulations at the various values of N_b indicated in the legend. Common parameter values in all the simulations are: $z = 1$, $\tilde{h}^* = 0.25$, and $N_k = 200$. Values of b, $\chi(b)$, h^*, z^*, λ_1^* and $\dot{\epsilon}^*$ used for each of the simulated values of N_b, are calculated as per the procedure described in section 5.3.

is maintained until $\epsilon = 13$, before being switched off, and the subsequent relaxation is observed for a period of time measured in terms of the nondimensional units, t/λ_1. The use of the stretch ratio and non-dimensional time as the axes enables a direct comparison of simulation and experiments. Clearly, the qualitative behaviour observed in experiments is captured in the simulations. The chains unravel from the coiled state and reach a steady-state value of stretch after about 8 Hencky strain units. While the curves for the different values of N_b are quite different from each other in the stretch phase, they become more tightly bunched together as the chains relax towards their equilibrium coiled state. In spite of the simulation predictions becoming closer to experimental measurements for increasing values of N_b, the significant quantitative difference between simulations and experiment at all values of N_b reported in Fig. 5.3, points to the importance of capturing all the degrees of freedom of the polymer chain being simulated. This is precisely the purpose of successive fine-graining, which we carry out below.

As described in section 5.3, the successive fine-graining technique maintains the key experimental variables constant at each level of fine-graining. For the

TABLE 5.1: Typical values of simulation parameters that arise at each level of coarse-graining when carrying out the successive fine-graining procedure for semidilute simulations, corresponding to the following set of experimental values: $\{c/c^* = 1, z = 1, N_k = 200 \text{ and } Wi = 2.6\}$. The hydrodynamic interaction parameter was maintained constant at $\tilde{h}^* = 0.19$.

N_b	b	$\chi(b)$	z^*	h^*	λ_1^*	$\dot{\epsilon}^*$
6	124.04	0.9413	0.3404	0.1788	11.021	0.1270
8	82.652	0.9258	0.2805	0.1759	17.826	0.0785
10	60.911	0.9114	0.2393	0.1731	25.883	0.0541
12	47.609	0.8976	0.2087	0.1705	35.104	0.0398

experimental results displayed in Fig. 5.3, these are: $\{c/c^* = 1, z = 1, N_k = 200, Wi = 2.6\}$. Note that the choice $N_k = 200$ represents our knowledge of the contour length L, and the persistence length λ_p of λ-phage DNA. For each choice of N_b, the parameters, b, $\chi(b)$, h^*, z^*, λ_1^* and $\dot{\epsilon}^*$ can be calculated as described in section 5.3. A representative set of values of these parameters for various values of N_b, obtained for the case $\tilde{h}^* = 0.19$, is displayed in Table 5.1.

Simulation predictions of the stretch ratio E in a step strain followed by cessation of flow simulation, both in the stretch phase (at $\epsilon = 7$ and $\epsilon = 13$), and in the relaxation phase (at $t/\lambda_1 = 0.5$, and $t/\lambda_1 = 4.0$), at two different values of $\tilde{h}^*$, for a set of coarse-grained chains with $N_b = \{6, 8, 10, 12\}$, are shown in Figs. 5.4. In each case, data accumulated for these values of N_b is extrapolated to the limit $(1/\sqrt{N_\mathrm{k}}) = 1/\sqrt{200}$. Clearly, in all cases, the extrapolated value of the expansion factor E is independent of the choice of value for $\tilde{h}^*$, within simulation error bars. This implies that, at $Wi = 2.6$, and the values of ϵ and t/λ_1 considered in Figs. 5.4, local details of the chain (such as the nondimensional bead radius) are masked from the flow, even though the polymer chains are exposed to a flow field, and universal predictions independent of choice of parameter values are obtained. We can anticipate that at higher Weissenberg numbers, and large values of strain, as the flow penetrates down to the shortest length scales of the chains, the different values chosen for $\tilde{h}^*$ may get "revealed", leading to predictions that are no longer parameter free. For all the values of Wi, ϵ and t/λ_1 considered in the
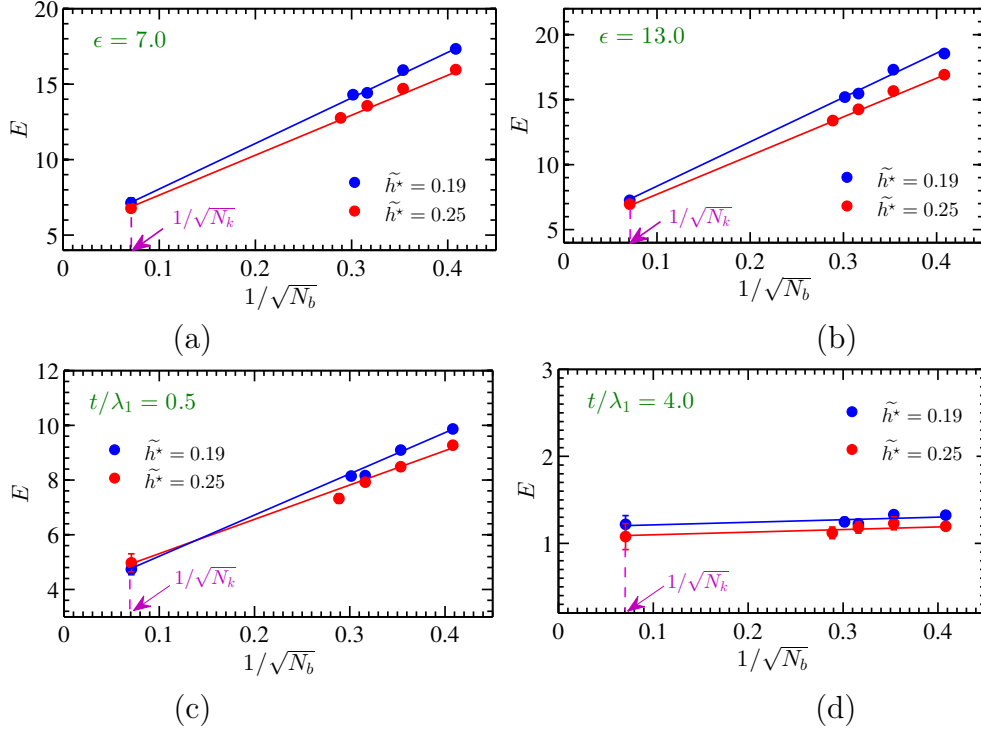
FIGURE 5.4:   Illustration of the extrapolation procedure during the stretching phase ((a) $\epsilon = 7$, and (b) $\epsilon = 13$), and the relaxation phase ((c) $t/\lambda_1 = 0.5$ and (d) $t/\lambda_1 = 4.0$) of a step strain followed by cessation of flow simulation, for two values of $\tilde{h}^*$. Parameters that are common to all simulations are: $c/c^* = 1$, $z = 1$, $N_k = 200$ and $Wi = 2.6$. Values of b, $\chi(b)$, h^*, z^*, λ_1^* and $\dot{\epsilon}^*$ used for each of the simulated values of $N_b = \{6, 8, 10, 12\}$, are calculated as per the procedure described in section 5.3. Lines through the data at these values of N_b indicate extrapolation to the limit $1/\sqrt{200}$.

experiments of Hsiao et al. (2016), however, we obtain parameter free predictions from the successive fine-graining procedure.

Hsiao et al. (2016) have carried out step strain followed by cessation of flow experiments, for an ultra-dilute solution ($c/c^* = 10^{-5}$) and for a semidilute solution ($c/c^* = 1$), for a range of different Weissenberg numbers. Predictions of the transient stretch ratio, obtained by carrying out the successive fine-graining procedure for a dilute solution with $c/c^* = 6.25 \times 10^{-12}$ at $Wi = 2.1$, and for a semidilute solution with $c/c^* = 1$ at $Wi = \{0.6, 1.4, 2.6\}$, at each of the measured values of ϵ in the stretch phase, and t/λ_1 in the relaxation phase, are shown in Figs. 5.5, and compared with the measurements of Hsiao et al. (2016). Clearly, the agreement between simulations and experiments is remarkable, and shows the
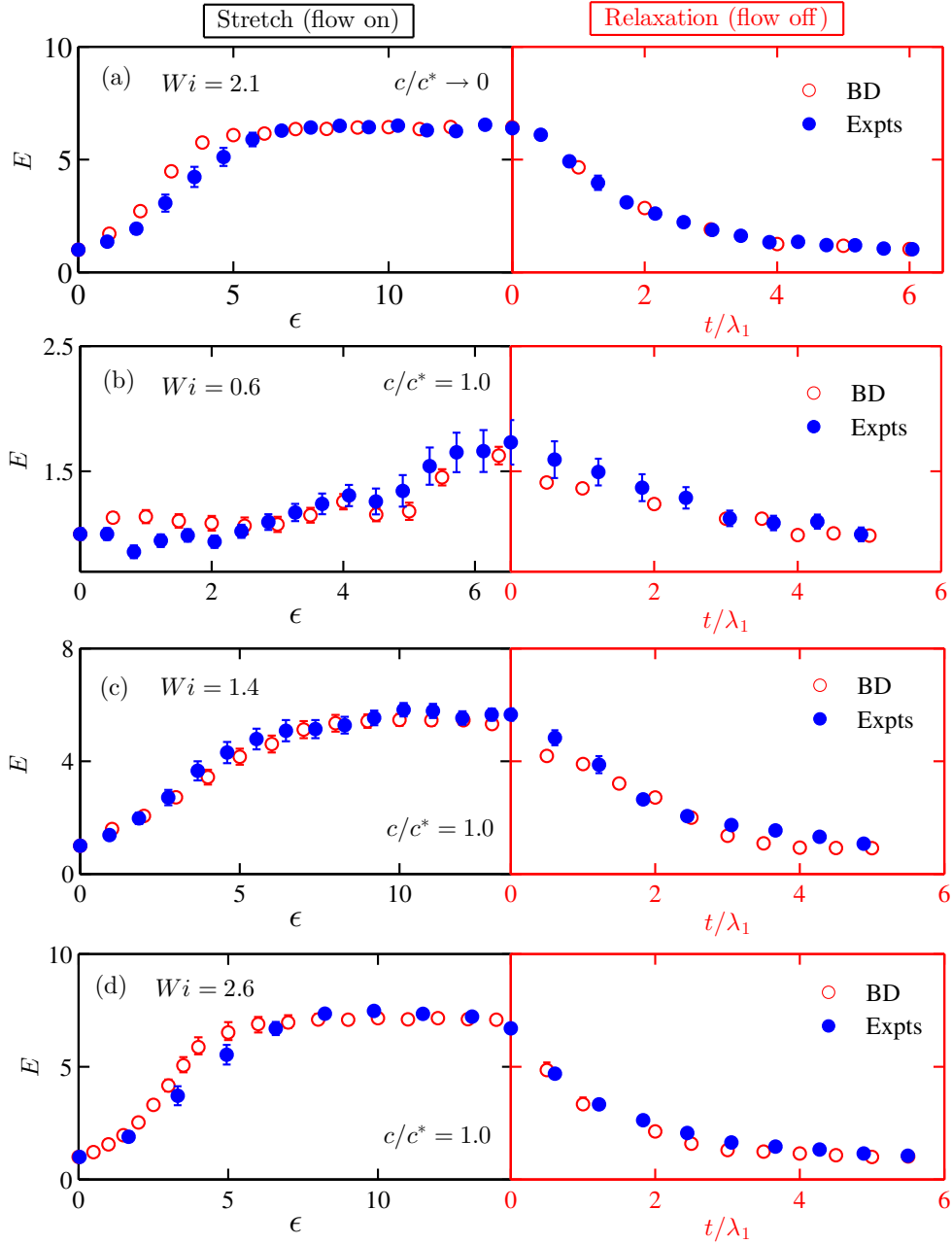
FIGURE 5.5: Comparison of the expansion factor E predicted by successive fine-graining with the experimental observations of Hsiao et al. (2016). The top panel corresponds to a dilute solution at $Wi = 2.1$. The remaining panels correspond to semidilute solutions at $c/c^* = 1$, and $Wi = \{0.6, 1.4, 2.6\}$, respectively. Simulations were carried out at fixed values of $z = 1$ and $N_k = 200$.

usefulness of the successive fine-graining procedure in obtaining parameter free predictions that are in quantitative agreement with measurements. Further, they

suggest that coarse-grained Brownian dynamics simulations appear to be capable of capturing the important physics that determine the dynamics of semidilute solutions.

An important experimental observation by Hsiao et al. (2016) is that the average transient fractional extension in start-up of planar extensional flow in a semidilute solution is much smaller than in a dilute solution, suggesting that interactions with surrounding chains restrains the stretching of chains. The formation of transient structures due to intermolecular interactions has been proposed in earlier experiments on semidilute solutions in shear flow (Hur et al., 2001; Babcock et al., 2000; Harasim et al., 2013; Huber et al., 2014). Fig. 5.6(a) compares the prediction by successive fine-graining of $(\bar{X}/L)$ versus ϵ, for a dilute solution (at $c/c^* = 6.25 \times 10^{-12}$) and a semidilute solution (at $c/c^* = 1$), for three different values of the Weissenberg number. Clearly, $(\bar{X}/L)$ is smaller for semidilute solutions than for dilute solutions at all values of Wi and ϵ, suggesting that BD simulations also exhibit the strong inhibition of chain stretching in semidilute solutions observed in experiments. The precise nature of the intermolecular interactions that lead to this phenomenon will be investigated further in the future. Fig. 5.6(b) compares the successive fine-graining predictions of the average transient fractional extension in semidilute solutions, with the experimental observations of Hsiao et al. (2016). This comparison is identical to the one carried out for semidilute solutions in Fig. 5.5. However, it is restricted to the stretching dynamics, and is in terms of the ratio $(\bar{X}/L)$ rather than E. Fig. 5.6(c) compares the successive fine-graining predictions of $(\bar{X}/L)$ for dilute solutions with experimental observations. At $Wi = 0.6$, comparison is made with the measurements of Perkins et al. (1997). The comparison with the dilute solution measurements of Hsiao et al. (2016) for $Wi = 2.1$ is identical to the comparison of stretching dynamics in Fig. 5.5, but is reported in terms of $(\bar{X}/L)$ rather than E. We have not carried out simulations at $Wi = 1.2$, for which Hsiao et al. (2016) have reported experimental measurements. However, as seen in the figure, successive fine-graining
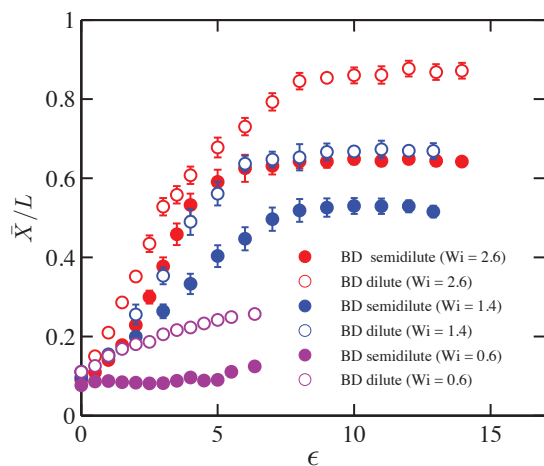
(a)
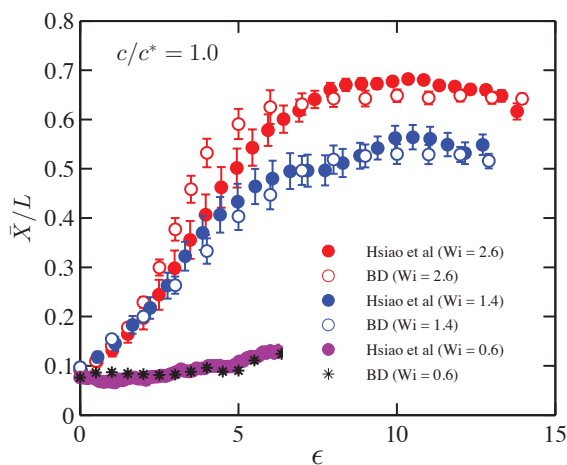
(b)
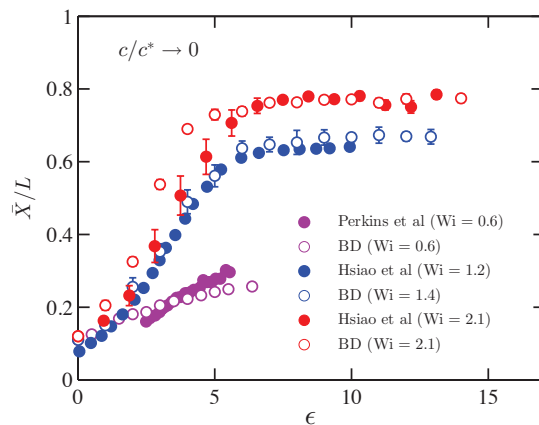
(c)

FIGURE 5.6:   Transient polymer stretch in dilute and semidilute so-
lutions at various values of the Weissenberg number. (a) Comparison
of transient fractional extension ($\bar{X}/L$) in planar extensional flow for di-
lute and semidilute solutions (at $c/c^* = 1$) predicted by successive fine-
graining. (b) Comparison of ($\bar{X}/L$) for semidilute solutions predicted
by successive fine-graining with experimental observations of Hsiao et al.
(2016). (c) Comparison of ($\bar{X}/L$) for dilute solutions predicted by suc-
cessive fine-graining with experimental observations of Hsiao et al. (2016)
and Perkins et al. (1997).

predictions at $Wi = 1.4$ are very close to the experimental values at $Wi = 1.2$. Figs. 5.6(b) and 5.6(c) once again reflect the quantitative accuracy with which successive fine-graining can predict transient chain stretch in extensional flows.

5.5 Summary and conclusions

A bead-spring chain model with N_b beads connected by springs obeying a worm-like chain spring force law has been used to model DNA molecules, and an ensemble of such chains in a simulation box with periodic boundary conditions is used to represent DNA solutions at a scaled finite concentration, c/c^*. The instantaneous location of all the beads in the system is determined by using a Brownian dynamics simulation algorithm to numerically integrate the stochastic differential equation that governs the time evolution of the spatial position of all the beads. Pair-wise long-range hydrodynamic interactions between the beads are modelled with a Rotne-Prager-Yamakawa tensor, and the conditionally convergent nature of the sum over all interactions is ameliorated by using an optimised Ewald summation technique. A narrow Gaussian potential is used to treat pair-wise excluded volume interactions between the beads, and the solvent quality of the solution, z, is captured by an appropriate choice of the strength of excluded volume interactions. The problem of simulating planar extensional flows in the context of periodic boundary conditions is tackled by implementing Kraynik-Reinelt boundary conditions. The principal observable quantity that is calculated is the average non-dimensional stretch $\bar{X}^*$, which is the ensemble averaged projected extent of a molecule in the flow direction. The non-dimensional stretch ratio, $E = \bar{X}^*/\bar{X}^*_{\text{eq}}$, and the transient normalised stretch, $\bar{X}^*/L^*$, are then obtained for a number of values of N_b, as a function of the Hencky strain ϵ in a transient stretching simulation (at various Weissenberg numbers Wi), and as a function of (t^*/λ_1^*), when the chains relax following the cessation of flow.

These results, however, are dependent on the choice of the number of beads N_b, and the values of the hydrodynamic interaction parameter h^*, and the excluded volume parameter z^*. In order to render the predictions parameter-free, the successive fine-graining technique is used to process the simulation data obtained for various values of N_b. Essentially, the experimentally relevant variables, $\{R_g^\theta, z, L, c/c^*, Wi\}$ are kept constant at each level of coarse-graining, and simulation data obtained at various values of N_b are extrapolated to the limit $(N_b - 1) \to N_k$. This is carried out at each value of ϵ in the stretching phase, and at each value of (t^*/λ_1^*) in the relaxation phase, in a simulation where a step strain deformation is followed by cessation of flow. The resulting predictions of E versus ϵ, and E versus (t/λ_1), are shown to be universal, in the sense that they do not depend on model parameters, at all the values of Wi considered here. The simulations predictions can consequently be directly compared with experiments without the need to tune any simulation parameters.

The recent experiments of Hsiao et al. (2016), using single molecule techniques to examine the dynamics of DNA molecules in semidilute solutions subjected to planar extensional flow, provide the motivation for the simulations reported in this work. Hsiao et al. (2016) observe that there is broad variability in the stretching dynamics of individual DNA in semidilute solutions, as observed previously for dilute solutions. However, possibly due to intermolecular interactions, the average transient stretch, $\bar{X}$, at identical Weissenberg numbers, is much smaller in semidilute solutions than in dilute solutions. The most salient experimental measurement in Hsiao et al., 2016, in the context of the present simulations, is the response of DNA molecules to a step strain deformation followed by the cessation of flow, both in ultra-dilute solutions, and for semidilute solutions at $c/c^* = 1$. In particular, measurements of the dependence of $(\bar{X}/L)$ on ϵ in the stretching phase, and on (t/λ_1) in the relaxation phase are reported at various values of Wi.

A qualitative comparison of simulation predictions with the experimental observations of Hsiao et al. (2016) (for semidilute solutions at $c/c^* = 1$) is first carried

out using a bead-spring chain model with $N_b = 45$. It is shown that in planar extensional flows, with increasing strain in the fluid, a wide variation in the transient unravelling dynamics of chains from a coiled state to a stretched state is observed in simulations, at a fixed value of Wi (see Fig. 5.1). Additionally, the probability distribution of the fractional stretch is seen to broaden significantly with increasing strain (see Fig. 5.2). Both these predictions are in qualitative agreement with experimental observations.

Comparison of simulation predictions for semidilute solutions at $c/c^* = 1$ (for various values of N_b) with experimental observations of the composite stretch relaxation curve for the transient stretch ratio E as a function of ϵ in the stretching phase, and (t/λ_1) in the relaxation phase, reveals a large discrepancy between predictions and experiments, and points to the shortcomings of using a bead-spring chain model with insufficient degrees of freedom (see Fig. 5.3).

Extrapolation of simulation data accumulated for a number of values of N_b to the limit $(N_b - 1) \to N_k$, using the successive fine-graining protocol, leads to predictions of the stretch ratio E which are independent of the choice of value for the hydrodynamic interaction parameter $\tilde{h}^*$. This is demonstrated (for semidilute solutions at $c/c^* = 1$) at two values of ϵ in the stretching phase, and at two values of (t/λ_1) in the relaxation phase, at a Weissenberg number $Wi = 2.6$ (see Fig. 5.4).

The extrapolated values of E obtained in this manner, at several values of ϵ and (t/λ_1), is assembled together and compared with experimental observations, for a dilute solution at $Wi = 2.1$, and for semidilute solutions at $Wi = \{0.6, 1.4, 2.6\}$. The successive fine-graining technique is shown to produce quantitatively accurate predictions of observations, both in the stretching and relaxation phases, across the range of Weissenberg numbers (see Fig. 5.5).

Finally, the experimental observation in a step strain deformation of inhibited transient stretching of DNA in semidilute solutions compared to dilute solutions, is seen to occur in simulations as well. A comparison of the normalised average stretch, $\bar{X}/L$ versus ϵ, obtained by successive fine-graining at various values of

Wi, shows that chains in dilute solutions always unravel more rapidly, and reach a higher steady-state value than in semidilute solutions. Further, as in the case of E, simulation predictions of $\bar{X}/L$ are seen to be in excellent agreement with experiments in dilute and in semidilute solutions (see Fig. 5.6).

Chapter 6

Coil-stretch hysteresis at finite concentrations

6.1 Introduction

The molecular mechanisms underlying the dynamics of flexible polymers in solution have long held the fascination of physicists (Rubinstein and Colby, 2003). It is recognized that at infinite dilution, intramolecular hydrodynamic interactions play a central role in determining mechanical properties of dilute polymer solutions. These interactions within each polymeric coil lead to the shielding of interior segments from the external flow field. The drag coefficient ζ_0 of an equilibrium coil of radius R_0 is close to that of a solid sphere of the same radius although most of its interior volume is occupied by the solvent. At the other extreme of concentration, neighbouring chains absorb the momentum propagation due to solvent perturbations, hydrodynamically screening segments of the same chain from one another. Macroscopic behaviour in concentrated solutions instead depends on the constrained thermal motion of each chain within its loose cage of neighbouring chains (Doi and Edwards, 1986).

Most of the analysis of hydrodynamic and excluded volume screening in semidilute solutions thus far has been restricted to conditions close to equilibrium where polymer chains are isotropic coils. Conventionally, the semidilute regime sets in

above the concentration $c^* \sim R_0^{-3}$ at which coils begin to overlap and interpenetrate. De Gennes (1974) argued that in semidilute solutions the typical length scale beyond which intermolecular screening becomes important is that at which the intramolecular segmental density is equal to the average segmental density in the whole solution. The polymer solution can be hence thought of as being spanned by "concentration blobs" within each of which the motion of segments of a chain are correlated with each other through hydrodynamic interactions. Segments separated by distances larger than the correlation blob size ξ_c only experience Rouse-like correlations due to backbone connectivity. The higher the concentration is in this semidilute regime, the smaller is ξ_c. Thus, within a blob, intramolecular shielding is important, whereas between blobs, intermolecular screening dominates. At sufficiently high concentrations, c is comparable to the segmental size b, and screening dominates to such an extent that molecules behave like freely draining chains. This blob picture explains well the observed scaling behaviour of dynamical properties near equilibrium; for instance, ζ_0 and the largest relaxation time λ_0 increase linearly with c in semidilute theta solutions, whereas in dilute solutions, these are independent of c.

The crossover from dilute to concentrated polymer solutions under conditions well out of equilibrium in strong flows however is not yet well understood. Here, we study the phenomenon of coil stretch hysteresis, which sheds some light on the emergence of hydrodynamic screening in highly stretched polymer molecules. The existence of the hysteresis was originally pointed out in the context of single polymer chains in dilute solutions by De Gennes (1974), Hinch (1977) and Tanner (1975). As chains stretch and segments separate out in a strong flow, hydrodynamic interactions and the shielding they provide weaken, exposing segments to the flow and increasing the average friction coefficient of the chain. The relative strength of an extensional flow is typically expressed in terms of the Weissenberg number $Wi = \dot{\epsilon}\lambda_0$, where $\dot{\epsilon}$ is the strain rate of the imposed flow and λ_0 is the timescale of the slowest relaxation mode of a polymer molecule in a quiescent solution.

Steady state in extensional flow is primarily the result of a balance between internal resistance of polymer molecules to stretching and the frictional drag force exerted on molecules by the flowing solvent. The work of De Gennes, Hinch and Tanner showed that due to the conformation-dependent friction of flexible molecules, the balance of forces leads to multiple steady states and pronounced hysteretic behaviour in macroscopic conformational and rheo-optical properties. The hysteresis occurs in a window of Weissenberg numbers, $Wi_{s-c} < Wi < Wi_{c-s}$, where Wi_{c-s} and Wi_{s-c} are the critical values for the coil-to-stretch and stretch-to-coil transitions. Single-molecule experiments (Schroeder et al., 2003) and Brownian dynamics simulations (Agarwal et al., 1998; Hsieh and Larson, 2005; Prabhakar and Prakash, 2006) and measurements with the filament stretching rheometer (FiSER) (Sridhar et al., 2007) have conclusively demonstrated the existence of this phenomenon in dilute polymer solutions.

It is known that the ratio Wi_{c-s}/Wi_{s-c} characterizing the width of the hysteresis window is proportional to ratio of the average friction coefficient ζ_s of a polymer chain stretched close to its contour length L, to the value ζ_0 (De Gennes, 1974; Schroeder et al., 2003; Prabhakar et al., 2016). In dilute solutions, $\zeta_0 \sim \eta_s R_0$ (where η_s is the solvent viscosity) and it is well known that the prefactor to the scaling relationship is a universal constant independent of the local hydrodynamic characteristics of monomers for large flexible molecules close to the non-draining limit (Kröger et al., 2000). Since typically $\zeta_s > \zeta_0$ for isolated chains, coil-stretch hysteresis in the dilute regime is observed for sufficiently long molecules. On the other hand, the Rouse theory is expected to hold for freely draining chains in concentrated unentangled solutions. In that case, there should be no hysteresis since the friction coefficient changes little with conformation for freely-draining chains i.e. $\zeta_s \sim \zeta_0 \sim h_K^* \eta_s L$. The Rouse friction is non-universal, depending directly on $h_K^* = a_K/(\sqrt{\pi} b_K)$, the hydrodynamic radius a_K of a single Kuhn segment normalized by its length b_K.

Until now, all the studies related to coil-stretch hysteresis phenomena have been

carried out in the ultra-dilute limit, i.e., by observing conformations of single chains (in the case of experiments), and performing simulations on single coarse-grained models for polymer molecules. So, the question is: how does the hysteresis window then change with concentration in going from dilute to concentrated solutions ? To the best of our knowledge, there are no prior simulations, or experimental investigations, on how concentration influences the extent of coil-stretch hysteresis exhibited in polymer solutions. In this study, we aim to examine the influence of concentration on the extent of coil-stretch hysteresis.

Importantly, in the context of the present work De Gennes (1974) in his original theory also predicted that in planar mixed flows, the coil-stretch hysteresis window would progressively decrease with increasing shear rate. As discussed previously in mixed flows, both elongational and rotational components exist but their contributions vary, characterized by a mixedness parameter, χ, with the limit of $\chi \to 0$, corresponds to pure shear flow, while the limit $\chi \to 1$ represents pure elongational flow. We investigate the influence of both polymer concentration and flow mixedness on the extent of coil-stretch hysteresis in polymer solutions undergoing planar mixed flows.

The chapter is organized as follows: In Section 6.2, we first present the scaling predictions of the influence of concentration on the hysteresis window size in extensional flows as discussed by Prabhakar et al. (2016). Simulation results are presented in the light of theoretical predictions in Section 6.3 for planar extensional flows, followed by simulation results for planar mixed flows. In Section 6.4, we summarize the central findings of the present work.

6.2   Scaling predictions

Prabhakar et al. (2016) combined the idea of a "correlation blob" with that of the "tension blob" proposed by Pincus (1976) to analyze the competition between

chain stretching and intermolecular screening in weakening intramolecular hydrodynamic interactions. The effects of chain self-avoidance and solvent quality were ignored for the sake of simplicity in that study. When a single polymer chain is stretched, the tension in the chain results in an anisotropic chain structure only beyond a characteristic length scale ξ_t. A single partially stretched chain can thus be pictured as a biased random walk of tension blobs. Hydrodynamically, the dilute regime for such partially stretched chains (region I in Fig. 6.1) is such that $cR^3 \ll 1$, where $R \gg R_0$ is the average end-to-end distance in a chain. Transverse conformational fluctuations in partially stretched polymer chains are large and similar in size to R_0 (Pincus, 1976). It is observed that these transverse fluctuations do not significantly contribute to ζ_s which is instead well approximated by treating a floppy stretched chain as a linear array of tension blobs so that $\zeta_s \sim \eta_s R / \ln(R/\xi_t)$ (Doi and Edwards, 1986; Prabhakar et al., 2016; Batchelor, 1970).

Due to transverse conformational fluctuations, stretched molecules begin to overlap when $cRR_0^2 \sim 1$ i.e. when $c/c^* \sim (R/R_0)^{-1}$ (dotted line in Fig. 6.1). Thus, even in nominally dilute solutions, chain overlap can be significant as a result of partial stretching. When such overlaps begin to occur in regime II in Fig. 6.1, correlation blobs are larger than tension blobs and hence anisotropic. Prabhakar et al. (2016) showed however that irrespective of any such overlaps, hydrodynamic screening by stretched neighbouring chains leads to a slow logarithmic increase in $\zeta_s \sim \eta_s R / [\ln(R/R_0) - \ln(c/c^*)]$ across the whole of regime II. Friction between stretched chains begins to increase linearly with concentration only after chains overlap to such an extent that the screening length $\xi_c < \xi_t$, the tension blob size. For any given chain stretch, solutions then enter regime III in Fig. 6.1 when $c/c^* \sim R/R_0$. In this regime, the shape, size and number of correlation blobs become independent of chain stretch R since they are below the length scale ξ_t at which the effect of stretching is significant. Their dependence on c/c^* is identical to that for equilibrium coils, and therefore, $\zeta_s = \zeta_0$ in regime III.
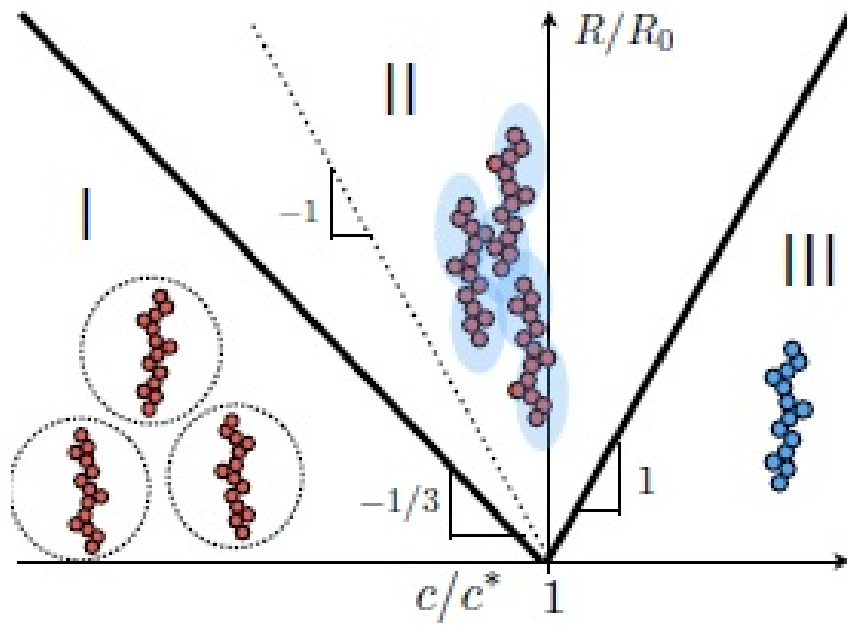
FIGURE 6.1: Stretch-concentration state diagram for polymer so-
lutions: I - dilute regime; II - weakly screened semidilute regime
(between the bold lines); III - strongly-screened semidilute regime.
The dotted line indicates overlap of partially stretched chains with
large transverse fluctuations. Tension blobs are coloured red, while
correlation blobs are coloured blue. Solvent-quality effects and en-
tanglements are neglected for simplicity. Reproduced from Prab-
hakar et al. (2016).

Predictions obtained with the blob model for the hysteresis window size are
presented in Fig. 6.2. As mentioned earlier, the ratio $Wi_{c-s}/Wi_{s-c} \sim \zeta_s/\zeta_0$ in gen-
eral. When $c < c^*$ in the weak-screening regime (II in Fig. 6.1), ζ_s increases
logarithmically with c whereas ζ_0 is nearly constant. In contrast, when $c > c^*$ with
the stretched state in regime II, while the equilibrium state is strongly screened
and ζ_0 increases linearly with c, the ratio ζ_s/ζ_0 decreases nearly as $(c/c^*)^{-1}$. Thus,
coil-stretch hysteresis is expected to be maximal at $c \sim c^*$. At high enough con-
centrations when even stretched chains are strongly screened, $\zeta_s \sim \zeta_0$: friction
becomes independent of conformation and hysteresis vanishes. Interestingly, when
chains are highly stretched or hydrodynamic screening is strong, the prefactors to
the scaling relationships for ζ_s are predicted to become sensitive to the frictional
characteristics of a single Kuhn segment, although hydrodynamic properties of
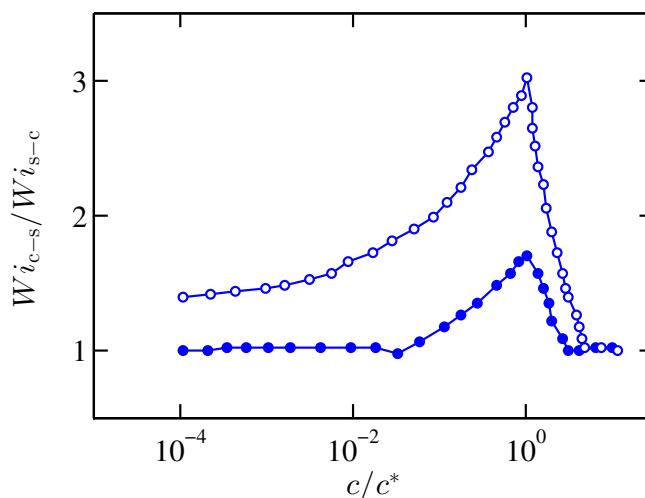
FIGURE 6.2: Concentration dependence of the width of the hysteresis window as predicted by the blob model of Prabhakar et al. (2016) at two values of h_K^*, namely, 0.025 (line with filled symbols) and 0.075 (line with open symbols). All data are for $N_K = 1300$.

isotropic coils of long flexible molecules are known to be relatively insensitive to segmental friction in the limit of infinite dilution. The ratio ζ_s/ζ_0 and hence the hysteresis window size is predicted to be directly proportional to hydrodynamic radius of a single Kuhn segment (Fig. 6.2). Therefore, in summary, the hysteresis window size is expected to first increase, reach a maximum at $c \sim c^*$, and then gradually decreases with increasing concentration i.e. there is a non-monotonic influence of concentration on the hysteresis window size. These scaling predictions by Prabhakar et al. (2016) are verified by simulations as discussed below.

6.3 Brownian dynamics simulation

A bead-spring chain model is used to represent polymer molecules wherein each molecule is coarse-grained into a sequence of N_b beads (which act as centers of hydrodynamic resistance) connected by $N_b - 1$ massless springs that represent the entropic force between two adjacent beads. The non-dimensional governing equation to track each bead of the polymer chain with time for the present multi-chain

BD simulations is the Ito stochastic differential equation based on the Euler integration scheme as presented by Eq. 2.1 in Chapter 2. Hydrodynamic interactions, caused by the movement of one polymer chain (intermolecular) or by segments of it (intramolecular), are treated with the Rotne-Prager-Yamakawa tensor as described in detail in Section 2.4 in Chapter 2. The entropic spring force acting between two adjacent beads is modeled by the FENE force law, given in Section 2.3 in Chapter 2 in detail. Furthermore, the Kraynik and Reinelt (1992) periodic boundary conditions are used to mimic the semidilute polymer solutions undergoing planar extensional and mixed flows as discussed in detail in Chapter 3.

The stress tensor (non-dimensionalized by $n_p k_B T$, where n_p is the number of polymer chains per unit volume), for a multi-chain system, can be calculated from Eq. 2.20 given in Chapter 2 by taking only the term contributed due to spring forces, i.e.,

$$\boldsymbol{\sigma} = \frac{1}{N_c} \left[\sum_{N_c} \sum_{\nu=1}^{N_b-1} \langle \mathbf{Q}_\nu \mathbf{F^c}(\mathbf{Q}_\nu) \rangle \right] \qquad (6.1)$$

where $\mathbf{Q}_\nu$ is the connector vector between the two beads $\mathbf{Q}_\nu = \mathbf{r}_{\nu+1} - \mathbf{r}_\nu$, and $\mathbf{F}^c(\mathbf{Q}_\nu)$ is the spring force between the beads ν and $\nu + 1$. All the results are reported here in terms of the scaled concentration c/c^*. Simulations were performed for two different initial configurations of the polymer molecules, namely, an initially coiled state where the polymer molecules are in the coiled state at the onset of flow, and an initially stretched state where the polymer chains are in the stretched state (90% of their full stretch) at the start-up of the flow. Prior to start the flow, the system is equilibrated for at least $50 - 80$ units of non-dimensional time for both initially coiled and initially stretched state configurations of the polymer chains. In order to observe the hysteresis window at a particular value of c/c^*, the value of strain rate ($\dot{\epsilon}$) is gradually increased (with a step of 0.005) in the case of initially coiled state until the coil to stretch (CS) transition occurs, whereas in the case of initially stretched chains, the value of strain rate is progressively decreased (with a step of 0.005) until the stretch to coil (SC) transition

occurs. At a particular value of strain rate, the viscosity of the polymer solutions is calculated once it reaches to the steady state after certain period of strain for both initially coiled and stretched state configurations of the polymer chains. The average value of the viscosity is carried out over 100 independent trajectories with 50000 data points in each trajectory.

6.3.1 Results

Planar extensional flows

For both initial configurations of the polymer chains, the following values of the numerical parameters are used: number of beads per chain, $N_b = 20$, number of Kuhn steps, $N_{ks} = 65$, hydrodynamic interaction parameter, $h^\star = 0.25$ and time step size, $\Delta t = 0.005$. Simulations were carried out for a range of values of $c/c^\star$, namely, $0, 0.05, 0.1, 0.5, 1.3$ and 2. The velocity gradient tensor for an extensional flow is given by Eq. 2.12 presented in Chapter 2. Once the stress tensor is calculated (Eq. 6.1), the viscosity of polymer solutions in an planar extensional flow ($\bar{\eta}_1$) is calculated by Eq. 2.25 written in Chapter 2.

Fig. 6.3 displays the results of the present simulations. As can be seen clearly, in the ultra-dilute limit ($c/c^* \to 0$), there is no hysteresis window present at all. However, as the concentration gradually increases, the hysteresis window starts to appear at $c/c^* = 0.05$, and it keeps until $c/c^* = 0.1$. With further increase in the concentration, the window size starts to decrease. The trend continues until $c/c^\star = 1.3$. Finally, at $c/c^\star = 2.0$, the hysteresis window disappears completely.

In Fig. 6.4, results are presented in terms of the ratio of Wi_{c-s}/Wi_{s-c} as discussed by Prabhakar et al. (2016) in their scaling predictions. The figure clearly indicates that there is a non-monotonic dependence on concentration of the width of the hysteresis window size, present which qualitatively supports the arguments of Prabhakar et al. (2016).
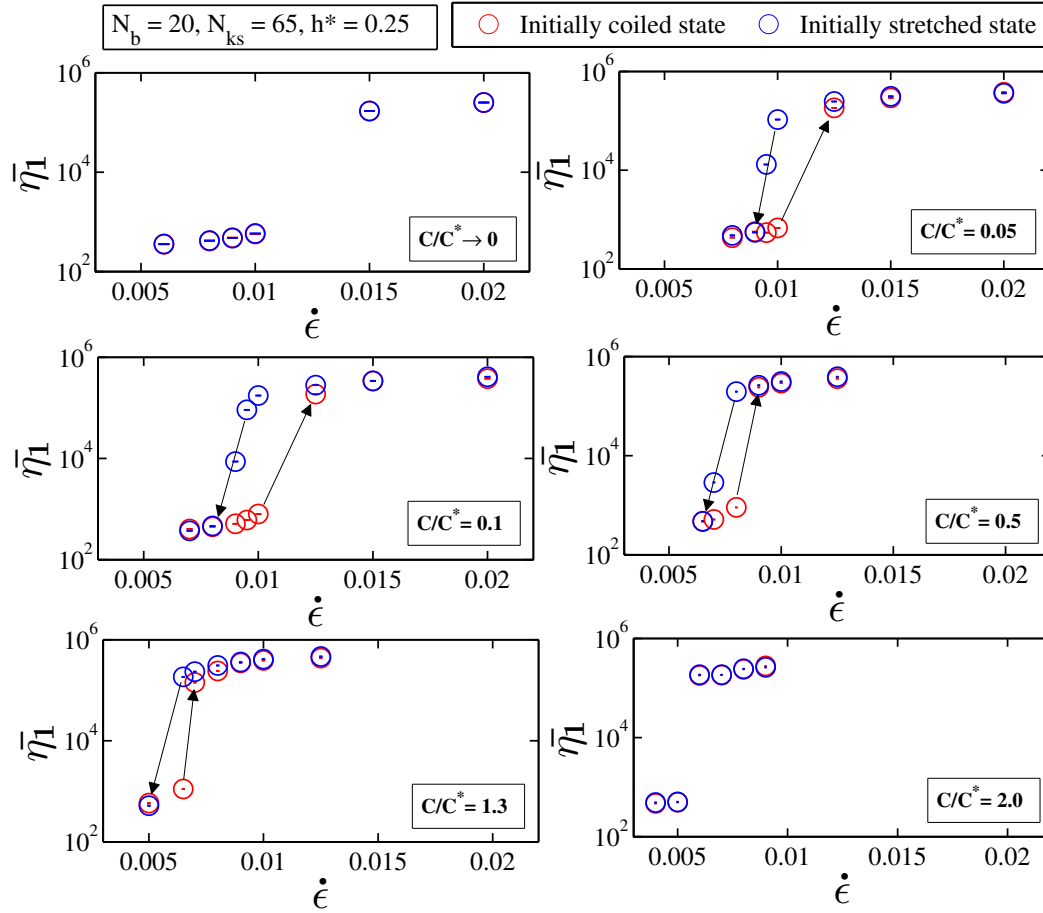
FIGURE 6.3: Influence of the concentration on the width of the hysteresis window size.

Planar mixed flows

The velocity gradient tensor for planar mixed flows in terms of the strength of mixed flow $\dot{\Gamma}$, and the mixedness parameter χ is given by Eq. 2.14 and the PMF viscosity is calculated by Eq. 2.26 as presented in Chapter 2.

De Gennes (1974) predicted that in planar mixed flows, the hysteresis window size gradually decreases as the shear rate progressively increases, i.e., the value of χ gradually decreases. On the other hand, as we have seen the hysteresis window progressively increases with the gradual increase of the concentration in the semidilute regime (up to $c \sim c^*$) which means the concentration has the opposite influence on the window size. Therefore in planar mixed flows, the ultimate size of the hysteresis window depends on these two competing mechanisms. In order
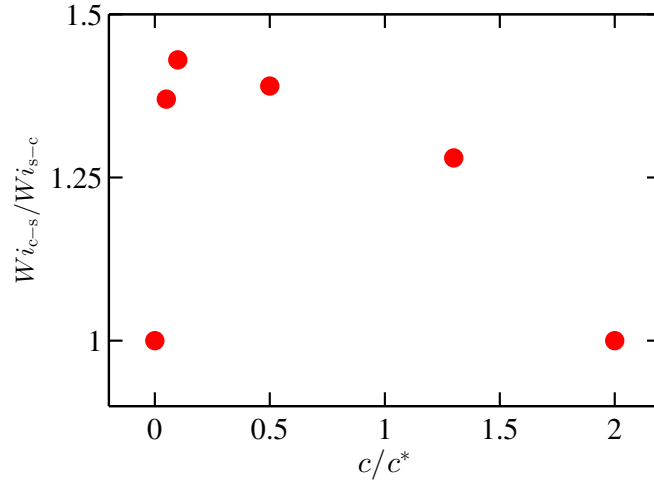
FIGURE 6.4:   Influence of the concentration on the width of the hysteresis window size.
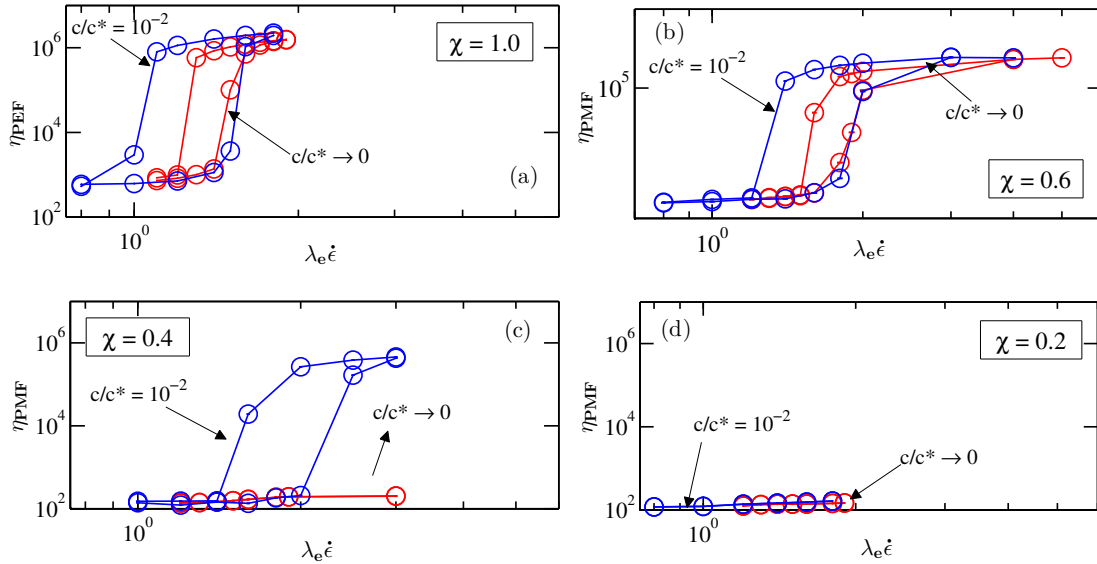
FIGURE 6.5:   Influence of the concentration and flow mixedness parameter on the width of the hysteresis window size.

to establish this, we run simulations at two concentrations namely, $c/c^* \to 0$ and $c/c^* = 10^{-2}$ for four values of χ, namely, 1.0 (pure extensional flow), 0.6, 0.4 and 0.2, and the results are presented in Fig. 6.5. The simulation parameters are $N_b = 26$, $N_k = 200$ and $h^* = 0.25$.

From Fig. 6.5(a), it can be again clearly seen that at $\chi = 1.0$, which corresponds to the pure extensional flow, the window size is larger at $c/c^* = 10^{-2}$ than at $c/c^* \to 0$. With decreasing values of χ, the size of the window for both concentrations

decreases, as evident in Figs. 6.5(b), (c) and (d). Furthermore it can be seen that at $\chi = 0.4$, the hysteresis window still exists at $c/c^* = 10^{-2}$, whereas for the ultra-dilute solution, there is no hysteresis window at all. This suggests that in planar mixed flows, the disappearance of the coil-stretch window occurs for smaller values of χ at lower concentrations.

6.4   Conclusions

This study addresses the phenomena of coil-stretch hysteresis in polymer solutions undergoing either pure planar extensional flow or mixed flow, i.e., a combination of shear and extensional flow, at finite concentrations. The present simulation results show an increase followed by a decrease in the coil-stretch hysteresis window size with increasing concentration in pure extensional flow, which is in qualitative agreement with the recent theoretical predictions by Prabhakar et al. (2016). Moreover, this study reveals that there is a competitive influence present between the concentration and flow mixedness parameter on the hysteresis window size in polymer solutions subjected to planar mixed flows.

Chapter 7

Conclusions and Future Work

The broad objective of this work has been to develop a predictive understanding of the behaviour of semidilute polymer solutions experiencing a variety of flows such as shear flow, extensional flow or a mixture of both, using a multi-chain BD algorithm. In order to achieve this, firstly, we have developed an optimized multi-particle BD algorithm which is capable to accurately capturing both hydrodynamic and excluded volume interactions, and which is able to simulate polymer solutions subject to arbitrary flows. Secondly, we have used this multi-chain BD algorithm to solve a variety of interesting problems in the domain of polymer physics involving flowing semidilute polymer solutions. In particular, the following is a brief list of the key aspects of this thesis:

1. We have successfully implemented the SPME method into the present multi-chain BD algorithm to efficiently treat long-ranged electrostatic and hydro-dynamic interactions, resulting in an algorithm of order $N\ln N$ in both cases. Additionally, we have proposed a simple and easy to follow scheme based on scaling arguments for the times taken by different steps involved in this method, which leads to the choice of optimal values for the governing parameters involved in the method. This in turn, leads to the total computational time being a minimum value for both HI and ES interactions (Chapter 3).

2. We have studied the dynamics of polymer solutions at finite concentrations

undergoing planar mixed flows (Chapter 4). In particular, we have investigated the effect of shear rate, extension rate, flow mixedness parameter and flow strength on the size of polymer chains and on the polymer contribution to viscosity for FENE dumbbells at finite concentrations. Furthermore, we have found a critical mixedness parameter, χ_c (which is a function of polymer concentrations), at which the viscosity remains constant irrespective of the values of the flow strength or Weissenberg number.

3. We have studied the stretching dynamics of λ-phage DNA molecules in an extensional flow, and the relaxation phenomena upon cessation of flow, as a function of concentration and Weissenberg number using the present multichain BD algorithm (Chapter 5). Parameter-free numerical predictions were obtained by the successive fine-graining technique which was introduced by Prakash and co-workers (Sunthar and Prakash, 2005; Prabhakar et al., 2004), and compared with single molecules experimental results of Hsiao et al. (2016). Excellent quantitative agreement in terms of the expansion ratio, E, (which is defined as the ratio of the transient stretch to that at equilibrium) was found between the two results. Furthermore, in this study, some key features of semidilute λ-phage DNA solutions undergoing extensional flows, have been revealed. For instance, with increasing values of strain, a wide variation in the transient unravelling dynamics of chains from a coiled state to a stretched state was observed thereby supporting the phenomenon of "molecular individualism" observed earlier in dilute solutions. The probability distribution of the fractional stretch of DNA molecules was seen to broaden significantly with increasing values of strain. Furthermore, this study revealed that polymer chains in dilute solutions always unravel more rapidly, and reach a higher steady-state value than in semidilute solutions. All these observations are in line with the experimental investigations of Hsiao et al. (2016).

4. We have investigated the well known "coil-stretch hysteresis" phenomena exhibited in polymer solutions at finite concentrations. In particular, we have studied the influence of concentration on the hysteresis window size of polymer solutions undergoing planar extensional flows. Our simulation results have shown an increase followed by a decrease in the hysteresis window size with increasing concentration, which is in line with the recent predictions of Prabhakar et al. (2016) based on blob theory. Furthermore, in the case of planar mixed flows, we have shown that the hysteresis window size depends on the competitive effects of concentration and the flow mixedness parameter (Chapter 6).

7.1 Future work

Some directions in which the studies of semidilute solutions can be pursued in the future are listed below:

1. Although we have made the present multi-chain BD algorithm sufficiently fast by the implementation of the SPME technique, however, the present implementation is for an equilibrated system where the simulation box remains cubic in shape with time, i.e. it doesn't deform in time. It is to be noted that the situation becomes complicated for a system under the influence of a flow field. For instance, in the case of an extensional flow, the side of the simulation box in the direction of flow gets exponentially stretched while the side perpendicular to it contracts exponentially with time. This makes the implementation of the SPME technique more challenging, in particular, the application of FFTW becomes difficult. This is because in order to carry out FFT of an array of data points using the FFTW package, we need to create grid of points in all three directions of the simulation box. These are fixed for an equilibrated system but for a system undergoing flow, they will change with time depending on the side length of the simulation box. It is

worth considering the implementation of the SPME method into the present multi-chain BD algorithm in the future.

2. The current SPME method can be made faster by employing paralellization techniques using MPI (Message Passing Interface) or OpenMP (Open Multi-Processing) for the application of the FFTW package. This will then enable the simulation of a large number of long polymer chains that are required for studying the universal behavior of semidilute solutions.

3. There are a number of scopes for improving the present BD algorithm. For instance, the present algorithm is based on a simple Euler integration scheme. The implementation of a semi-implicit predictor-corrector method may lead to an improvement of the speed of the present multi-chain BD algorithm, as observed earlier in case of the dilute code. Further, a Verlet table can be implemented to make the evaluation of the real space part of the Ewald sum more efficient. All these improvements could make the present BD algorithm competitive with other mesoscopic simulation algorithms available in the literature.

4. We have studied the mixed flow dynamics of FENE dumbbells at finite concentrations in the absence of hydrodynamic interactions. This work can be extended to study the effect of polymer size and hydrodynamic interactions on the rheological properties of polymer solutions at finite concentrations. Further, in planar mixed flows, we have found the critical mixedness parameter, χ_c, at which the viscosity remains constant independent of the values of Weissenberg number, and which is a function of concentration. It would be interesting to carry out an investigation on how the chain size and hydrodynamic interaction parameter influence the critical value of the mixedness parameter.

5. In the present study, simulations have been performed to study the stretching dynamics of linear DNA molecules in an extensional flow, and a detailed comparison with the experimental results of Hsiao et al. (2016) has been carried out. It would be really worthwhile to study the dynamics of circular DNA molecules, which exhibit fascinating behaviour in extensional flow, as observed experimentally recently by Li et al. (2015).

6. The current study of coil-stretch hysteresis has been qualitative in nature. A detailed comparison with experimental observations, using the successive fine-graining technique would be a powerful test of whether all the important physics that governs the phenomenon has been captured in the simulations.

Appendix A

Approximation of structure factor for electrostatic interactions

The manner by which the term $\exp(2\pi i \mathbf{k} \cdot \mathbf{r}_\mu)$ in the expression for the structure factor, defined in Eq. 3.11 for electrostatic interactions, can be interpolated to p neighbouring sites, where p is the order of interpolation, has already been shown in Sec. 3.2.3 in the context of hydrodynamic interactions. The detailed derivation of it, has also been presented by Essmann et al. (1995) and by others (Wang et al., 2010; Ballenegger et al., 2012). Here, we rewrite some of these expressions for the sake of completeness.

The position vector $\mathbf{r}_\mu$ of particle μ inside the reciprocal unit cell is rescaled as $\xi_{\mu i} = K_i r_{\mu i}/L$, where K_i is the total number of mesh points in the direction i, and L is the length of the system. In the new fractional co-ordinate system, the exponential term in the structure factor defined in Eq. 3.11 can be rewritten as follows:

$$\exp(2\pi i \mathbf{k} \cdot \mathbf{r}_\mu) = \exp\left(2\pi i k_1 \frac{\xi_{\mu 1}}{K_1}\right) \exp\left(2\pi i k_2 \frac{\xi_{\mu 2}}{K_2}\right) \exp\left(2\pi i k_3 \frac{\xi_{\mu 3}}{K_3}\right) \qquad \text{(A.1)}$$

We can approximate the term $\exp\left(2\pi i k_i \frac{\xi_{\mu i}}{K_i}\right)$ using the properties of cardinal B-splines interpolation as follows (Essmann et al., 1995):

$$\exp\left(2\pi i k_i \frac{\xi_{\mu i}}{K_i}\right) \approx b_\mu(k_{\mu i}) \sum_{m=-\infty}^{+\infty} M_p(\xi_{\mu i} - m) \cdot \exp\left(2\pi i \frac{k_i}{K_i} m\right) \qquad \text{(A.2)}$$

where

$$b_\mu(k_{\mu i}) = \exp\left[2\pi i(p-1)\frac{k_{\mu i}}{K_i}\right] \times \left[\sum_{k=0}^{p-2} M_p(k+1)\exp\left(2\pi i k_{\mu i}\frac{k}{K_i}\right)\right]^{-1} \quad (A.3)$$

where $M_p(u)$ are the Cardinal B-splines with p^{th} order of interpolation. The structure factor, $\mathbf{S}^{\text{ES}}(\mathbf{k})$ defined in Eq. 3.11, is then approximated as follows:

$$\mathbf{S}^{\text{ES}}(\mathbf{k}) \approx \tilde{\mathbf{S}}^{\text{ES}}(\mathbf{k}) \approx b_1(k_1)b_2(k_2)b_3(k_3)\mathcal{F}(Q)(k_1,k_2,k_3) \quad (A.4)$$

where $\mathcal{F}(Q)$ is the three-dimensional discrete Fourier transform of the matrix array $Q(\mathbf{k})$ of dimension $K_1 \times K_2 \times K_3$ given by the following expression:

$$Q(k_1,k_2,k_3) = \sum_{\mu=1}^{N}\sum_{p_1,p_2,p_3} q_\mu M_p(\xi_1^\mu - k_1 - p_1 K_1)M_p(\xi_2^\mu - k_2 - p_2 K_2)M_p(\xi_3^\mu - k_3 - p_3 K_3)$$

$$(A.5)$$

Hence, the reciprocal part of the energy of the Ewald sum for electrostatic interactions defined in Eq. 3.9 can be written in approximate form as follows:

$$E_{reci} = \frac{1}{2\pi V}\sum_{\mathbf{k}\neq\mathbf{0}}\frac{\exp(-\pi^2\mathbf{k}^2/\alpha^2)}{\mathbf{k}^2}B(k_1,k_2,k_3)\mathcal{F}(Q)(k_1,k_2,k_3)\mathcal{F}(Q)(-k_1,-k_2,-k_3)$$

$$= \frac{1}{2}\sum_{k_1=0}^{K_1-1}\sum_{k_2=0}^{K_2-1}\sum_{k_3=0}^{K_3-1} Q(k_1,k_2,k_3)\cdot(\theta_{\text{rec}}\star Q)(k_1,k_2,k_3)$$

$$(A.6)$$

where, the pair potential θ_{rec} is given by $\theta_{rec} = F(B\cdot C)$, and $\star$ denotes the convolution between θ_{rec} and Q. The array C is given by the following expression:

$$C(k_1,k_2,k_3) = \frac{1}{\pi V}\frac{\exp(-\pi^2\mathbf{k}^2/\alpha^2)}{\mathbf{k}^2} \quad (A.7)$$

and the array B is given by the same expression as given by Eq. 3.20 in Sec. 3.2.3. Finally, the reciprocal force on particle μ in the direction i can be calculated by

the following expression:

$$F_{reci} = -\frac{\partial E_{reci}}{\partial \mathbf{r}_{i\mu}} = \frac{1}{2} \sum_{k_1=0}^{K_1-1} \sum_{k_2=0}^{K_2-1} \sum_{k_3=0}^{K_3-1} \frac{\partial Q(k_1, k_2, k_3)}{\partial \mathbf{r}_{i\mu}} \cdot (\theta_{\text{rec}} \star Q)(k_1, k_2, k_3) \qquad (A.8)$$

Appendix B

Initial lattice vector for PMFs

Kraynik and Reinelt (1992) point out in their seminal paper on the derivation of PBCs for PEF, that $(\boldsymbol{\nabla v})_{\mathrm{PEF}}$ can be replaced by any diagonalizable constant matrix with real eigenvalues and zero trace. Hunt et al. (2010) have exploited this observation by noting that $(\boldsymbol{\nabla v})_{\mathrm{PMF}}$ is a diagonalizable matrix,

$$
\begin{pmatrix} \dot{\epsilon} & 0 & 0 \\ \dot{\gamma} & -\dot{\epsilon} & 0 \\ 0 & 0 & 0 \end{pmatrix} = \begin{pmatrix} 1 & 0 & 0 \\ \frac{\dot{\gamma}}{2\dot{\epsilon}} & 1 & 0 \\ 0 & 0 & 1 \end{pmatrix} \begin{pmatrix} \dot{\epsilon} & 0 & 0 \\ 0 & -\dot{\epsilon} & 0 \\ 0 & 0 & 0 \end{pmatrix} \begin{pmatrix} 1 & 0 & 0 \\ -\frac{\dot{\gamma}}{2\dot{\epsilon}} & 1 & 0 \\ 0 & 0 & 1 \end{pmatrix} = \mathbf{T} \cdot \mathbf{D} \cdot \mathbf{T^{-1}} \quad \text{(B.1)}
$$

where $\mathbf{T}$ is a transformation matrix that consists of the eigenvectors of $(\boldsymbol{\nabla v})_{\mathrm{PMF}}$, and the diagonal matrix $\mathbf{D}$ has the same component form as $(\boldsymbol{\nabla v})_{\mathrm{PEF}}$. The Kraynik-Reinelt periodic boundary condition for PEF is written in terms of the lattice evolution matrix $\boldsymbol{\Lambda} = \exp{(\mathbf{D}t)}$. Similarly for PMF, as the velocity gradient tensor $(\boldsymbol{\nabla v})_{\mathrm{PMF}}$ is diagonalizable, we can write the lattice evolution matrix $\boldsymbol{\Lambda}'$ as

$$
\boldsymbol{\Lambda}' = \exp{((\boldsymbol{\nabla v})_{\mathrm{PMF}}t)} = \exp{(\mathbf{T} \cdot \mathbf{D} \cdot \mathbf{T^{-1}}t)} = \mathbf{T} \cdot \exp{(\mathbf{D}t)} \cdot \mathbf{T^{-1}} \quad \text{(B.2)}
$$

As $(\boldsymbol{\nabla v})_{\mathrm{PMF}} = \mathbf{T} \cdot \mathbf{D} \cdot \mathbf{T^{-1}}$ with $\mathbf{D}$ being a diagonal matrix, a new set of initial basis vectors,

$$
\mathbf{b_i^{0\prime}} = \mathbf{b_i^0} \cdot \mathbf{T^{-1}} \quad \text{(for } i = 1, 2, 3) \quad \text{(B.3)}
$$

exists in PMF, such that this new set is reproducible in the case of PMF (Hunt et al., 2010). The tensor $\mathbf{T}^{-1}$, thus, can be understood as a mapping necessary to make the PEF basis vectors $\mathbf{b_i^0}$ (in PEF) reproducible in the PMF (see Refs. Kraynik and Reinelt (1992) and Jain (2013) for more detail on PEF lattice basis vectors). An equation for the lattice reproducibility condition for PMF can be written as,

$$\mathbf{b_i}' = \mathbf{b_i^{0\prime}} \cdot \mathbf{\Lambda}' \tag{B.4}$$

where $\mathbf{b_i}'$ denotes the lattice vector at time τ_p (strain period). Using this relation, and substituting $\mathbf{\Lambda}'$ from Eq. (B.2) in Eq. (B.4) leads to the following simplification

$$
\begin{aligned}
\mathbf{b_i}'(t = \tau_p) &= \mathbf{b_i^{0\prime}} \cdot \mathbf{\Lambda}'(\tau_p) \\
&= \mathbf{b_i^0} \cdot \mathbf{T}^{-1} \cdot \mathbf{T} \cdot \exp\left(\mathbf{D}t\right) \cdot \mathbf{T}^{-1} \\
&= \mathbf{b_i^0} \cdot \exp\left(\mathbf{D}t\right) \cdot \mathbf{T}^{-1} \\
&= \left[N_{i1}\mathbf{b_1^0} + N_{i2}\mathbf{b_2^0} + N_{i3}\mathbf{b_3^0}\right] \cdot \mathbf{T}^{-1} \\
&= N_{i1}\mathbf{b_1^0} \cdot \mathbf{T}^{-1} + N_{i2}\mathbf{b_2^0} \cdot \mathbf{T}^{-1} + N_{i3}\mathbf{b_3^0} \cdot \mathbf{T}^{-1} \\
&= N_{i1}\mathbf{b_1^{0\prime}} + N_{i2}\mathbf{b_2^{0\prime}} + N_{i3}\mathbf{b_3^{0\prime}}
\end{aligned}
\tag{B.5}
$$

This equation for the reproducibility condition is identical to the one for PEF (Kraynik and Reinelt, 1992), except that $\mathbf{b_i^0}$ is replaced by $\mathbf{b_i^{0\prime}}$. The vectors $\mathbf{b_1^{0\prime}}$, $\mathbf{b_2^{0\prime}}$ and $\mathbf{b_3^{0\prime}}$ can be found easily since $\mathbf{b_1^0}$, $\mathbf{b_2^0}$ and $\mathbf{b_3^0}$ are known for PEF. The mapping of Eq. (B.3) is applied to $\mathbf{b_i^0}$ to obtain a reproducible lattice under mixed flow as follows.

$$
\begin{aligned}
\mathbf{b_1^{0\prime}} &= \mathbf{b_1^0} \cdot \mathbf{T}^{-1} \\
&= \begin{pmatrix} \cos\theta & \sin\theta & 0 \end{pmatrix} \begin{pmatrix} 1 & 0 & 0 \\ -\frac{\dot{\gamma}}{2\dot{\epsilon}} & 1 & 0 \\ 0 & 0 & 1 \end{pmatrix} \\
&= \left[\left(\cos\theta - \frac{\dot{\gamma}}{2\dot{\epsilon}}\sin\theta\right), \sin\theta, 0\right]
\end{aligned}
\tag{B.6}
$$

$$\mathbf{b_2^{0'}} = \mathbf{b_2^0} \cdot \mathbf{T}^{-1}$$

$$= \begin{pmatrix} -\sin\theta & \cos\theta & 0 \end{pmatrix} \begin{pmatrix} 1 & 0 & 0 \\ -\frac{\dot{\gamma}}{2\dot{\epsilon}} & 1 & 0 \\ 0 & 0 & 1 \end{pmatrix} \tag{B.7}$$

$$= \left[\left(-\sin\theta - \frac{\dot{\gamma}}{2\dot{\epsilon}}\cos\theta \right), \cos\theta, 0 \right]$$

$$\mathbf{b_3^{0'}} = \mathbf{b_3^0} \cdot \mathbf{T}^{-1}$$

$$= \begin{pmatrix} 0 & 0 & 1 \end{pmatrix} \begin{pmatrix} 1 & 0 & 0 \\ -\frac{\dot{\gamma}}{2\dot{\epsilon}} & 1 & 0 \\ 0 & 0 & 1 \end{pmatrix} \tag{B.8}$$

$$= [0, 0, 1]$$

where θ is the magic angle, which is similar to that for PEF. In contrast to PEF, where the basis lattice vectors are orthogonal, in the case of PMF, they are non-orthogonal and not equal in length. If the elongational rate is high or the shear rate is small, these lattice vectors becomes almost orthogonal and equal in length. These basis lattice vectors are used as an initial lattice configuration.

Bibliography

Agarwal, U. S., R. Bhargava, and R. A. Mashelkar (1998). "Brownian dynamics simulation of a polymer molecule in solution under elongational flow". In: *J. Chem. Phys.* 108, pp. 1610–1617.

Ahlrichs, P. and B. Dünweg (1999). "Simulation of a single polymer chain in solution by combining lattice Boltzmann and molecular dynamics". In: *J. Chem. Phys.* 111, pp. 8225–8239.

Ahlrichs, P. and B. Dünweg (1999). "Simulation of a single polymer chain in solution by combining lattice Boltzmann and molecular dynamics". In: *J. Chem. Phys.* 111, p. 8225.

Ahlrichs, P., R. Everaers, and B. Dünweg (2001). "Screening of hydrodynamic interactions in semidilute polymer solutions: A computer simulation study". In: *Phys. Rev. E* 64, p. 040501.

Babcock, H. P., D. E. Smith, J. S. Hur, E. S. G. Shaqfeh, and S. Chu (2000). "Relating the microscopic and macroscopic response of a polymeric fluid in a shearing flow". In: *Phys. Rev. Lett.* 85, pp. 2018–2021.

Babcock, H. P., R. E. Teixeira, J. S. Hur, E. S. G. Shaqfeh, and S. Chu (2003). "Visualization of molecular fluctuations near the critical point of the coil-stretch transition in polymer elongation". In: *Macromolecules* 36, pp. 4544–4548.

Baird, D. G. and D. I. Collias (1998). *Polymer Processing: Principles and Design*. Wiley New York.

Ballenegger, V., J. J. Cerda, O. Lenz, and C. Holm (2008). "The optimal P3M algorithm for computing electrostatic energies in periodic systems". In: *J. Chem. Phys.* 128, p. 034109.

Ballenegger, V., J. J. Cerdà, and C. Holm (2012). "How to convert SPME to P3M: Influence functions and error estimates". In: *J. Chem. Theo. Comp.* 8, pp. 936–947.

Baranyai, A. and P. T. Cummings (1995). "Nonequilibrium molecular dynamics study of shear and shear-free flows in simple fluids". In: *J. Chem. Phys.* 103, pp. 10217–10225.

— (1999). "Steady state simulation of planar elongation flow by nonequilibrium molecular dynamics". In: *J. Chem. Phys.* 110, pp. 42–45.

Bastamante, C., J. F. Marko, E. D. Siggia, and S. Smith (1994). "Entropic elasticity of lambda-phage DNA". In: *Science* 265, pp. 1599–1600.

Batchelor, G. K. (1970). "Slender-body theory for particles of arbitrary cross-section in Stokes flow". In: *J. Fluid Mech.* 44, pp. 419–440.

Beenakker, C. W. J. (1986). "Ewald sum of the Rotne-Prager tensor". In: *J. Chem. Phys.* 85, pp. 1581–1582.

Bhupathiraju, R., P. T. Cummings, and H. D. Cochran (1996). "An efficient parallel algorithm for non-equilibrium molecular dynamics simulations of very large systems in planar Couette flow". In: *Mol. Phys.* 88, pp. 1665–1670.

Bird, R. B., R. C. Armstrong, and O. Hassager (1987a). *Dynamics of Polymeric Liquids: Fluid Mechanics.* Vol. 1. New York: John Wiley and Sons.

Bird, R. B., C. F. Curtiss, R. C. Armstrong, and O. Hassager (1987b). *Dynamics of Polymeric Liquids: Kinetic Theory.* Vol. 2. New York: John Wiley and Sons.

Bosko, J. T. and J. R. Prakash (2011). "Universal behavior of dendrimer solutions". In: *Macromolecules* 44, pp. 660–670.

Brown, W. and T. Nicolai (1990). "Static and dynamic behavior of semidilute polymer solutions". In: *Coll. & Poly. Sci.* 268.11, pp. 977–990.

Cerdà, J. J., V. Ballenegger, and C. Holm (2011). "Particle-particle particle-mesh method for dipolar interactions: On error estimates and efficiency of schemes with analytical differentiation and mesh interlacing". In: *J. Chem. Phys.* 135, p. 184110.

Chu, S. (1991). "Laser manipulation of atoms and particles". In: *Science* 253, pp. 861–866.

Chui, C. K. (2014). *An Introduction to Wavelets*. Vol. 1. Academic press.

Crosby, A. and J. R. Lister (2013). "Hydrodynamic diffusion of sedimenting point particles in a vertical shear flow". In: *J. Fluid Mech.* 730, pp. 699–732.

Daivis, P. J., M. L. Matin, and B. D. Todd (2003). "Nonlinear shear and elongational rheology of model polymer melts by non-equilibrium molecular dynamics". In: *J. Non-Newt. Fluid Mech.* 111, pp. 1–18.

Dalal, I. S., N. Hoda, and R. G. Larson (2012). "Multiple regimes of deformation in shearing flow of isolated polymers". In: *J. Rheol.* 56, pp. 305–332.

Darden, T., D. York, and L. Pedersen (1993). "Particle mesh Ewald: An NlogN method for Ewald sums in large systems". In: *J. Chem. Phys.* 98, pp. 10089–10092.

De Gennes, P. G. (1974). "Coil-stretch transition of dilute flexible polymers under ultrahigh velocity gradients". In: *J. Chem. Phys.* 60, pp. 5030–5042.

— (1976a). "Dynamics of entangled polymer solutions. I. The Rouse model". In: *Macromolecules* 9, pp. 587–593.

— (1976b). "Dynamics of entangled polymer solutions. II. Inclusion of hydrodynamic interactions". In: *Macromolecules* 9, pp. 594–598.

— (1979). *Scaling Concepts in Polymer Physics*. Cornell University Press.

Deserno, M. and C. Holm (1998a). "How to mesh up Ewald sums. I. A theoretical and numerical comparison of various particle mesh routines". In: *J. Chem. Phys.* 109, pp. 7678–7693.

— (1998b). "How to mesh up Ewald sums. II. An accurate error estimate for the particle-particle-particle-mesh algorithm". In: *J. Chem. Phys.* 109, pp. 7694–7701.

Doi, M. and S. F. Edwards (1986). *The Theory of Polymer Dynamics*. Oxford, New York: Clarendon Press.

Dua, A. and B. J. Cherayil (2003). "Polymer dynamics in linear mixed flow". In: *J. Chem. Phys.* 119, pp. 5696–5700.

Dünweg, B. and A. J. C. Ladd (2008). "Lattice Boltzmann simulations of soft matter systems". In: *Adv. Poly. Sci.* Pp. 1–78.

Dünweg, B. and A. J. C. Ladd (2009). "Lattice Boltzmann simulations of soft matter systems". In: *Adv. Poly. Sci.* 221, pp. 1–78.

Eastwood, J. W. (1975). "Optimal particle-mesh algorithms". In: *J. Comp. Phys.* 18, pp. 1–20.

Essmann, U., L. Perera, M. L. Berkowitz, T. Darden, H. Lee, and L. G. Pedersen (1995). "A smooth particle mesh Ewald method". In: *J. Chem. Phys.* 103, pp. 8577–8593.

Evans, D. J. (1979). "The frequency dependent shear viscosity of methane". In: *Mol. Phys.* 37, pp. 1745–1754.

Ewald, P. P. (1921). "Die Berechnung optischer und elektrostatischer Gitterpotentiale". In: *Annalen der Physik* 369, pp. 253–287.

FFTW package. URL:

Fincham, D. (1994). "Optimization of the Ewald Sum for Large Systems". In: *Mol. Sim.* 13, pp. 1–9.

Freire, J. J, A. Rey, and J. Garcia de La Torre (1986). "Monte Carlo calculations for linear and star polymers with intramolecular interactions. 2. Nonpreaveraged study of hydrodynamic properties at the θ state". In: *Macromolecules* 19, pp. 457–462.

Fuller, G. G. and L. G. Leal (1981). "The effects of conformation-dependent friction and internal viscosity on the dynamics of the nonlinear dumbbell model for a dilute polymer solution". In: *J. Non-Newt. Fluid Mech.* 8, pp. 271 –310.

Gans, B. J. de, P. C. Duineveld, and U. S. Schubert (2004). "Inkjet printing of polymers: state of the art and future developments". In: *Adv. Mat.* 16, pp. 203–213.

García Bernal, J. M., M. M. Tirado, J. J. Freire, and J. Garcia de La Torre (1991). "Monte Carlo calculation of hydrodynamic properties of linear and cyclic polymers in good solvents". In: *Macromolecules* 24, pp. 593–598.

Gennes, P. G. de (1974). "Coil-stretch transition of dilute flexible polymers under ultrahigh velocity gradients". In: *J. Chem. Phys.* 60, pp. 5030–5042.

— (1979). *Scaling Concepts in Polymer Physics*. Cornell University Press.

— (1997). "Molecular individualism". In: *Science* 276, pp. 1999–2000.

Gompper, G., T. Ihle, D. M. Kroll, and R. G. Winkler (2009). "Multi-particle collision dynamics: a particle-based mesoscale simulation approach to the hydrodynamics of complex fluids". In: *Advances Computer Simulation Approaches for Soft Matter Sciences III*, pp. 1–87.

Greengard, L. and V. Rokhlin (1987). "A fast algorithm for particle simulations". In: *J. Comp. Phys.* 73, pp. 325–348.

Hajizadeh, E., B. D. Todd, and P. J. Daivis (2014). "Nonequilibrium molecular dynamics simulation of dendrimers and hyperbranched polymer melts undergoing planar elongational flow". In: *J. Rheol.* 58, pp. 281–305.

Hansen, D. P. and D. J. Evans (1994). "A parallel algorithm for nonequilibrium molecular dynamics simulation of shear flow on distributed memory machines". In: *Mol. Sim.* 13, pp. 375–393.

Harasim, M., B. Wunderlich, O. Peleg, M. Kröger, and A. R. Bausch (2013). "Direct observation of the dynamics of semiflexible polymers in shear flow". In: *Phys. Rev. Lett.* 110, p. 108302.

Hartkamp, R., S. Bernardi, and B. D. Todd (2012). "Transient-time correlation function applied to mixed shear and elongational flows". In: *J. Chem. Phys.* 136, p. 064105.

Hartkamp, R., B. D. Todd, and S. Luding (2013). "A constitutive framework for the non-Newtonian pressure tensor of a simple fluid under planar flows". In: *J. Chem. Phys.* 138, p. 244508.

Hasimoto, M. (1959). "On the Periodic Fundamental Solutions of the Stokes Equations and Their Applications to Viscous Flow Past a Cubic Array of Spheres". In: *J. Fluid Mech.* 5, p. 317.

Hernández-Ortiz, J. P., J. J. de Pablo, and M. D. Graham (2006). "NlogN method for hydrodynamic interactions of confined polymer systems: Brownian dynamics". In: *J. Chem. Phys.* 125, p. 164906.

Hinch, E. J. (1977). "Mechanical models of dilute polymer solutions in strong flows". In: *Phys. Fluids* 20, S22–S30.

Hockney, R. W. and J. W. Eastwood (1988). *Computer Simulation using Particles.* CRC Press.

Hockney, R. W., S. P. Goel, and J. W. Eastwood (1973). "A 10000 particle molecular dynamics model with long range forces". In: *Chem. Phys. Lett.* 21, pp. 589–591.

Hoffman, B. D. and E. S. G. Shaqfeh (2007). "The dynamics of the coil-stretch transition for long, flexible polymers in planar mixed flows". In: *J. Rheol.* 51, pp. 947–969.

Hounkonnou, M. N., C. Pierleoni, and J.-P. Ryckaert (1992). "Liquid Chlorine in shear and elongational flows: A nonequilibrium molecular dynamics study". In: *J. Chem. Phys.* 97, pp. 9335–9344.

Hsiao, K., C. Sasmal, J. R. Prakash, and C. M. Schroeder (2016). "Direct observation of DNA dynamics in semi-dilute solutions in extensional flow". In: *Submitted.*

Hsieh, C.-C. and R. G. Larson (2004). "Modeling hydrodynamic interaction in Brownian dynamics: Simulations of extensional and shear flows of dilute solutions of high molecular weight polystyrene". In: *J. Rheol.* 48, pp. 995–1021.

— (2005). "Prediction of coil-stretch hysteresis for dilute polystyrene molecules in extensional flow". In: *J. Rheol.* 49, pp. 1081–1089.

Hsieh, C.-C., L. Li, and R. G. Larson (2003). "Modeling hydrodynamic interaction in Brownian dynamics: simulations of extensional flows of dilute solutions of DNA and polystyrene". In: *J. Non-Newt. Fluid Mech.* 113, pp. 147–191.

Huang, C.-C., R. G. Winkler, G. Sutmann, and G. Gompper (2010). "Semidilute polymer solutions at equilibrium and under shear Flow". In: *Macromolecules* 43, pp. 10107–10116.

Huber, B., M. Harasim, B. Wunderlich, M. Kröger, and A. R. Bausch (2014). "Microscopic origin of the non-Newtonian viscosity of semiflexible polymer solutions in the semidilute regime". In: *ACS Macro Lett.* 3, pp. 136–140.

Hünenberger, P. H. and J. A. McCammon (1999). "Ewald artifacts in computer simulations of ionic solvation and ion–ion interaction: a continuum electrostatics study". In: *J. Chem. Phys.* 110, pp. 1856–1872.

Hunt, T. A., S. Bernardi, and B. D. Todd (2010). "A new algorithm for extended nonequilibrium molecular dynamics simulations of mixed flow". In: *J. Chem. Phys.* 133, p. 154116.

Hur, J. S., E. S. G. Shaqfeh, and R. G. Larson (2000). "Brownian dynamics simulations of single DNA molecules in shear flow". In: *J. Rheol.* 44, pp. 713–742.

Hur, J. S., E. S. G. Shaqfeh, H. P. Babcock, D. E. Smith, and S. Chu (2001). "Dynamics of dilute and semidilute DNA solutions in the start-up of shear flow". In: *J. Rheol.* 45, pp. 421–450.

Hur, J. S., E. S. G. Shaqfeh, H. P. Babcock, and S. Chu (2002). "Dynamics and configurational fluctuations of single DNA molecules in linear mixed flows". In: *Phys. Rev. E* 66, p. 011915.

Jain, A. (2013). "Unravelling the Dynamics of Semidilute Polymer Solutions Using Brownian Dynamics". PhD thesis. Monash University.

Jain, A., B. Dünweg, and J. R. Prakash (2012a). "Dynamic crossover scaling in polymer solutions". In: *Phys. Rev. Lett.* 109, p. 088302.

Jain, A., P. Sunthar, B. Dünweg, and J. R. Prakash (2012b). "Optimization of a Brownian-dynamics algorithm for semidilute polymer solutions". In: *Phys. Rev. E* 85, p. 066703.

Jain, A., C. Sasmal, R. Hartkamp, B. D. Todd, and J. R. Prakash (2015). "Brownian dynamics simulations of planar mixed flows of polymer solutions at finite concentrations". In: *Chem. Eng. Sci.* 121, pp. 245–257.

Jendrejack, R. M., J. J. de Pablo, and M. D. Graham (2002). "Stochastic simulations of DNA in flow: Dynamics and the effects of hydrodynamic interactions". In: *J. Chem. Phys.* 116, pp. 7752–7759.

Kapral, R. (2008). "Multiparticle collision dynamics: simulation of complex systems on mesoscales". In: *Adv. Chem. Phys.* 140, p. 89.

Knudsen, H., J. Werth, and D. Wolf (2008). "Failure and success of hydrodynamic interaction models". In: *Eur. Phys. J. E: Soft Matter and Bio. Phys.* 27.

Kolafa, J. and J. W. Perram (1992). "Cutoff errors in the Ewald summation formulae for point charge systems". In: *Mol. Sim.* 9, pp. 351–368.

Kozer, N., Y. Y. Kuttner, G. Haran, and G. Schreiber (2007). "Protein-protein association in polymer solutions: from dilute to semidilute to concentrated". In: *Biophys. J.* 92, pp. 2139–2149.

Kraynik, A. M. and D. A. Reinelt (1992). "Extensional motions of spatially periodic lattices". In: *Int. J. Mult. Flow* 18, pp. 1045–1059.

Krigbaum, W. R. and P. J. Flory (1953). "Molecular weight dependence of the intrinsic viscosity of polymer solutions. II". In: *J. Poly. Sci.* 11, pp. 37–51.

Krigbaum, W. R., L. Mandelkern, and P. J. Flory (1952). "Molecular weight dependence of intrinsic viscosity of polymer solutions". In: *J. Poly. Sci.* 9, pp. 381–384.

Kröger, M., A. Alba-Pérez, M. Laso, and H. C. Öttinger (2000). "Variance reduced Brownian simulation of a bead-spring chain under steady shear flow considering hydrodynamic interaction effects". In: *J. Chem. Phys.* 113, pp. 4767–4773.

Kröger, Martin (2004). "Simple models for complex nonequilibrium fluids". In: *Phys. Rep.* 390, pp. 453–551.

Kumar, K. S. and J. R. Prakash (2003). "Equilibrium swelling and universal ratios in dilute polymer solutions: exact Brownian dynamics simulations for a delta function excluded volume potential". In: *Macromolecules* 36, pp. 7842–7856.

— (2004a). "Universal consequences of the presence of excluded volume interactions in dilute polymer solutions undergoing shear flow". In: *J. Chem. Phys.* 121, pp. 3886–3897.

— (2004b). "Universal consequences of the presence of excluded volume interactions in dilute polymer solutions undergoing shear flow". In: *J. Chem. Phys.* 121, pp. 3886–3897.

Kundukad, B., J. Yan, and P. S. Doyle (2014). "Effect of YOYO-1 on the mechanical properties of DNA". In: *Soft matter* 10, pp. 9721–9728.

Larson, R. G. (1999). *The Structure and Rheology of Complex Fluids*. 1st. New York: Oxford University Press.

— (2005). "The rheology of dilute solutions of flexible polymers: Progress and problems". In: *J. Rheol.* 49, pp. 1–70.

Larson, R. G. and H. Hu (1999). "Brownian dynamics simulations of a DNA molecule in an extensional flow field". In: *J. Rheol.* 43, pp. 267–304.

Larson, R. G., H. Hu, D. E. Smith, and S. Chu (1999). "Brownian dynamics simulations of a DNA molecule in an extensional flow field". In: *J. Rheol.* 43, pp. 267–304.

LeDuc, P., C. Haber, G. Bao, and D. Wirtz (1999). "Dynamics of individual flexible polymers in a shear flow". In: *Nature* 399, pp. 564–566.

Lee, J. S., R. Dylla-Spears, N. P. Teclemariam, and S. J. Muller (2007). "Microfluidic four-roll mill for all flow types". In: *App. Phys. Lett.* 90, p. 074103.

Lees, A. W. and S. F. Edwards (1972). "The computer study of transport processes under extreme conditions". In: *J. Phys. C: Solid State Phys.* 5, p. 1921.

Li, Y., K.-W. Hsiao, C. A. Brockman, D. Y. Yates, R. M. Robertson-Anderson, J. A. Kornfield, M. J. San Francisco, C. M. Schroeder, and G. B. McKenna (2015). "When ends meet: circular DNA stretches differently in elongational flows". In: *Macromolecules* 48, pp. 5997–6001.

Liang, Z., Z. Gimbutas, L. Greengard, J. Huang, and S. Jiang (2013). "A fast multipole method for the Rotne–Prager–Yamakawa tensor and its applications". In: *J. Comp. Phys.* 234, pp. 133–139.

Lindbo, D. and A.-K. Tornberg (2010). "Spectrally accurate fast summation for periodic Stokes potentials". In: *J. Comp. Phys.* 229, pp. 8994–9010.

— (2011). "Spectral accuracy in fast Ewald-based methods for particle simulations". In: *J. Comp. Phys.* 230, pp. 8744–8761.

— (2012). "Fast and spectrally accurate Ewald summation for 2-periodic electrostatic systems". In: *J. Chem. Phys.* 136, p. 164111.

Linse, B. and P. Linse (2014). "Tuning the smooth particle mesh Ewald sum: application on ionic solutions and dipolar fluids." In: *J. Chem. Phys.* 141, p. 184114.

Liu, Y., Y. Jun, and V. Steinberg (2009). "Concentration dependence of the longest relaxation times of dilute and semi-dilute polymer solutions". In: *J. Rheol.* 53, pp. 1069–1085.

Luty, B. A., M. E. Davis, I. G. Tironi, and W. F. Van Gunsteren (1994). "A comparison of particle-particle, particle-mesh and Ewald methods for calculating electrostatic interactions in periodic molecular systems". In: *Mol. Sim.* 14, pp. 11–20.

Mai, D. J., C. Brockman, and C. M. Schroeder (2012). "Microfluidic systems for single DNA dynamics". In: *Soft Matt.* 8, pp. 10560–10572.

Malevanets, A. and R. Kapral (1999). "Mesoscopic model for solvent dynamics". In: *J. Chem. Phys.* 110, pp. 8605–8613.

Marciel, A. B. and C. M. Schroeder (2013). "New directions in single polymer dynamics". In: *J. Poly. Sci. Part B: Poly. Phys.* 51, pp. 556–566.

Miyaki, Y., Y. Einaga, H. Fujita, and M. Fukuda (1980). "Flory's viscosity factor for the system polystyrene + cyclohexane at 34.5C". In: *Macromolecules* 13, pp. 588–592.

Muthukumar, M. and S. F. Edwards (1982). "Screening concepts in polymer solution dynamics". In: *Polymer* 23, pp. 345–348.

— (1983). "Screening of hydrodynamic interaction in a solution of rodlike macromolecules". In: *Macromolecules* 16, pp. 1475–1478.

Omari, R. A., A. M. Aneese, C. A. Grabowski, and A. Mukhopadhyay (2009). "Diffusion of nanoparticles in semidilute and entangled polymer solutions". In: *J. Phys. Chem. B* 113, pp. 8449–8452.

Öttinger, H. C. (1987). "Generalized Zimm model for dilute polymer solutions under theta conditions". In: *J. Chem. Phys.* 86, pp. 3731–3749.

— (1989). "Gaussian approximation for Rouse chains with hydrodynamic interaction". In: *J. Chem. Phys.* 90, pp. 463–473.

— (2012). *Stochastic processes in polymeric fluids: tools and examples for developing simulation algorithms.* Springer Science & Business Media.

Öttinger, H. C. and Y. Rabin (1989). "Renormalization-group calculation of viscometric functions based on conventional polymer kinetic theory". In: *J. Non-Newt. Fluid Mech.* 33, pp. 53–93.

Pan, S., D. A. Nguyen, T. Sridhar, P. Sunthar, and J. R. Prakash (2014a). "Universal solvent quality crossover of the zero shear rate viscosity of semidilute DNA solutions". In: *J. Rheol.* 58, pp. 339–368.

Pan, S., D. Ahirwal, D. A. Nguyen, T. Sridhar, P. Sunthar, and J. R. Prakash (2014b). "Viscosity radius of polymers in dilute solutions: universal behavior from DNA rheology and Brownian dynamics simulations". In: *Macromolecules* 47, pp. 7548–7560.

Pecora, R. (1991). "DNA: a model compound for solution studies of macromolecules". In: *Science* 251, pp. 893–898.

Perkins, T., D. Smith, R. Larson, and S. Chu (1995). "Stretching of a single tethered polymer in a uniform flow". In: *Science* 268, pp. 83–87.

Perkins, T. T., D. E. Smith, and S. Chu (1994a). "Direct observation of tube-like motion of a single polymer chain". In: *Science* 264, pp. 819–822.

— (1994b). "Relaxation of a single DNA molecule observed by optical microscopy". In: *Science* 264, pp. 822–826.

Perkins, T. T., S. R. Quake, D. E. Smith, and S. Chu (1994c). "Relaxation of a single DNA molecule observed via optical microscopy". In: *Science* 264, pp. 822–825.

Perkins, T. T., D. E. Smith, and S. Chu (1997). "Single polymer dynamics in an elongational flow". In: *Science* 276, pp. 2016–2021.

Petersen, H. G. (1995). "Accuracy and efficiency of the particle mesh Ewald method". In: *J. Chem. Phys.* 103, pp. 3668–3679.

Pham, T. T., P. Sunthar, and J. R. Prakash (2008). "An alternative to the bead-rod model: bead-spring chains with successive fine graining". In: *J. Non-Newt. Fluid Mech.* 149, pp. 9–19.

Pincus, P. (1976). "Excluded volume effects and stretched polymer chains". In: *Macromolecules* 9, pp. 386–388.

Prabhakar, R. and J. R. Prakash (2004). "Multiplicative separation of the influences of excluded volume, hydrodynamic interactions and finite extensibility on the rheological properties of dilute polymer solutions". In: *J. Non-Newt. Fluid Mech.* 116, p. 163.

— (2006). "Gaussian approximation for finitely extensible bead-spring chains with hydrodynamic interaction". In: *J. Rheol.* 50, pp. 561–593.

Prabhakar, R. and J. Ravi Prakash (2002). "Viscometric functions for Hookean dumbbells with excluded volume and hydrodynamic interactions". In: *J. Rheol.* 46, pp. 1191–1220.

Prabhakar, R., J. R. Prakash, and T. Sridhar (2004). "A successive fine-graining scheme for predicting the rheological properties of dilute polymer solutions". In: *J. Rheol.* 48, pp. 1251–1278.

Prabhakar, R., S. Gadkari, T. Gopesh, and M. J. Shaw (2016). "Influence of stretching induced self-concentration and self-dilution on coil-stretch hysteresis and capillary thinning of unentangled polymer solutions". In: *J. Rheol.* 60, pp. 345–366.

Prakash, J. R. (2001a). "Rouse chains with excluded volume interactions: Linear viscoelasticity". In: *Macromolecules* 34, pp. 3396–3411.

— (2001b). "The influence of the range of excluded volume interactions on the linear viscoelastic properties of dilute polymer solutions". In: *Chem. Eng. Sci.* 56, pp. 5555–5564.

— (2002a). "Rouse chains with excluded volume interactions in steady simple shear flow". In: *J. Rheol.* 46, pp. 1353–1380.

— (2002b). "Rouse chains with excluded volume interactions in steady simple shear flow". In: *J. Rheol.* 46, pp. 1353–1380.

— (2009). "Micro and macro in the dynamics of dilute polymer solutions: Convergence of theory with experiment". In: *Korea-Australia Rheol. J.* 21, pp. 245–268.

Prakash, J. R. and H. C. Öttinger (1997). "Universal viscometric functions for dilute polymer solutions". In: *J. Non-Newt. Fluid Mech.* 71, pp. 245–272.

— (1999). "Viscometric functions for a dilute solution of polymers in a good solvent". In: *Macromolecules* 32, pp. 2028–2043.

Quake, S. R., H. Babcock, and S. Chu (1997). "The dynamics of partially extended single molecules of DNA". In: *Nature* 388, pp. 151–154.

Ramakrisna, S., K. Fujihara, W.-E. Teo, T.-C. Lim, and Z. Ma (2005). *An Introduction to Electrospinning and Nanofibers*. World Scientific.

Richter, D., K. Binder, B. Ewen, and B. Stühn (1984). "Screening of hydrodynamic interactions in dense polymer solutions: a phenomenological theory and neutron-scattering investigations". In: *J. Phys. Chem.* 88, pp. 6618–6633.

Robertson, R. M. and D. E. Smith (2006). "Diffusion of isolated DNA molecules: dependence on length and topology". In: *Proc. Nat. Aca. Sci. U.S.A.* 103, pp. 7310–7314.

— (2007). "Self-diffusion of entangled linear and circular DNA molecules: Dependence on length and concentration". In: *Macromolecules* 40, pp. 3373–3377.

Rotne, J. and S. Prager (1969). "Variational treatment of hydrodynamic interaction in polymers". In: *J. Chem. Phys.* 50, pp. 4831–4837.

Rubinstein, M. and R. H. Colby (2003). *Polymer Physics.* Oxford University Press.

Saadat, A. and B. Khomami (2015a). "Matrix-free Brownian dynamics simulation technique for semidilute polymeric solutions". In: *Phys. Rev. E* 92, p. 033307.

— (2015b). "Molecular based prediction of the extensional rheology of high molecular weight polystyrene dilute solutions: A hi-fidelity Brownian dynamics approach". In: *J. Rheol.* 59, pp. 1507–1525.

Saintillan, D., E. Darve, and E. S. G. Shaqfeh (2005). "A smooth particle-mesh Ewald algorithm for Stokes suspension simulations: The sedimentation of fibers". In: *Phys. Fluids* 17, p. 3301.

Schäfer, L. (2012). *Excluded Volume Effects in Polymer Solutions: As Explained by the Renormalization Group.* Springer Science & Business Media.

Schmitz, R. and B. U. Felderhof (1982). "Mobility matrix for two spherical particles with hydrodynamic interaction". In: *Phys. A. Statistical Mechanics and its Applications* 116, pp. 163–177.

Schoenberg, I. J. (1973). *Cardinal Spline Interpolation.* SIAM, Philadelphia, PA.

Schroeder, C. M., H. P. Babcock, E. S. G. Shaqfeh, and S. Chu (2003). "Observation of polymer conformation hysteresis in extensional flow". In: *Science* 301, pp. 1515–1519.

Schroeder, C. M., E. S. G. Shaqfeh, and S. Chu (2004a). "Effect of hydrodynamic interactions on DNA dynamics in extensional flow: Simulation and single molecule experiment". In: *Macromolecules* 37, pp. 9242–9256.

— (2004b). "Effect of hydrodynamic interactions on DNA dynamics in extensional flow: simulation and single molecule experiment". In: *Macromolecules* 37, pp. 9242–9256.

Schroeder, C. M., R. E. Teixeira, E. S. G. Shaqfeh, and S. Chu (2005). "Dynamics of DNA in the flow-gradient plane of steady shear Flow: Observations and simulations". In: *Macromolecules* 38, pp. 1967–1978.

Shan, Y., J. L. Klepeis, M. P. Eastwood, R. O. Dror, and D. E. Shaw (2005). "Gaussian split Ewald: A fast Ewald mesh method for molecular simulation". In: *J. Chem. Phys.* 122, p. 054101.

Shaqfeh, E. S. G. (2005). "The dynamics of single-molecule DNA in flow". In: *J. Non-Newt. Fluid Mech.* 130, pp. 1–28.

Shiwa, Y. (1995). "Theory of polymer relaxation times in semi-Dilute solutions". In: *Int. J. Modern Phys. B* 9, pp. 57–67.

Shiwa, Y., Y. Oono, and P. R. Baldwin (1988). "Dynamics of semidilute polymer solutions: hydrodynamic screening". In: *Macromolecules* 21, pp. 208–214.

Sierou, A. and J. F. Brady (2001). "Accelerated Stokesian dynamics simulations". In: *J. Fluid Mech.* 448, pp. 115–146.

Smith, D. E. and S. Chu (1998). "Response of flexible polymers to a sudden elongational flow". In: *Science* 281, pp. 1335–1340.

Smith, D. E., T. T. Perkins, and S. Chu (1995). "Self-Diffusion of an Entangled DNA Molecule by Reptation". In: *Phys. Rev. Lett.* 75, pp. 4146–4149.

— (1996). "Dynamical scaling of DNA diffusion coefficients". In: *Macromolecules* 29, pp. 1372–1373.

Smith, D. E., H. P. Babcock, and S. Chu (1999). "Single polymer dynamics in shear flows". In: *Science* 283, pp. 1724–1727.

Somani, S., E. S. G. Shaqfeh, and J. R. Prakash (2010). "Effect of Solvent Quality on the Coil- Stretch Transition". In: *Macromolecules* 43, pp. 10679–10691.

Sridhar, T., D. A. Nguyen, R. Prabhakar, and J. R. Prakash (2007). "Rheological observation of glassy dynamics of dilute polymer solutions near the coil-stretch transition in elongational flows". In: *Phys. Rev. Lett.* 98, p. 167801.

Stoltz, C. (2006). "Simulation of dilute polymer and polyelectrolyte solutions: Concentration effects". PhD thesis. The University of Wisconsin.

Stoltz, C., J. J. de Pablo, and M. D. Graham (2006). "Concentration dependence of shear and extensional rheology of polymer solutions: Brownian dynamics simulations". In: *J. Rheol.* 502, p. 137.

Sunthar, P. and J. R. Prakash (2005). "Parameter-free prediction of DNA conformations in elongational flow by successive fine graining". In: *Macromolecules* 38, pp. 617–640.

— (2006). "Dynamic scaling in dilute polymer solutions: The importance of dynamic correlations". In: *Euro. Lett.* 75, p. 77.

Sunthar, P., D. A. Nguyen, R. Dubbelboer, J. R. Prakash, and T. Sridhar (2005). "Measurement and prediction of the elongational stress growth in a dilute solution of DNA molecules". In: *Macromolecules* 38, pp. 10200–10209.

Tanner, R. I. (1975). "Stresses in Dilute Solutions of Bead-Nonlinear-Spring Macromolecules. III. Friction Coefficient Varying with Dumbbell Extension". In: *J. Rheol.* 19, pp. 557–582.

Teixeira, R. E., A. K. Dambal, D. H. Richter, E. S. G. Shaqfeh, and S. Chu (2007). "The individualistic dynamics of entangled DNA in solution". In: *Macromolecules* 40, pp. 2461–2476.

Thurston, G. B. and A. Peterlin (1967). "Influence of finite number of chain segments, hydrodynamic interaction, and internal viscosity on intrinsic birefringence and viscosity of polymer solutions in an oscillating laminar flow field". In: *J. Chem. Phys.* 46, pp. 4881–4885.

Todd, B. D. and P. J. Daivis (1998). "Non-equilibrium molecular dynamics simulations of planar elongational flow with spatially and temporally periodic boundary conditions". In: *Phys. Rev. Lett.* 81, p. 1118.

Todd, Billy D (2001). "Computer simulation of simple and complex atomistic fluids by nonequilibrium molecular dynamics techniques". In: *Comput. Phys. Commun.* 142, pp. 14–21.

Tominaga, Y., I. Suda, M. Osa, T. Yoshizaki, and H. Yamakawa (2002). "Viscosity and hydrodynamic-radius expansion factors of oligo- and poly(a-methylstyrene)s in dilute solution". In: *Macromolecules* 35, pp. 1381–1388.

Torre, J. Garcia De la, M. C. Lopez Martinez, and M. M. Tirado (1984). "Monte Carlo study of hydrodynamic properties of flexible linear chains: analysis of several approximate methods". In: *Macromolecules* 17, pp. 2715–2722.

Wang, H., F. Dommert, and C. Holm (2010). "Optimizing working parameters of the smooth particle mesh Ewald algorithm in terms of accuracy and efficiency." In: *J. Chem. Phys.* 133.3, pp. 034117–034117.

Wirtz, D. (1995). "Direct measurement of the transport properties of a single DNA molecule". In: *Phys. Rev. Lett.* 75, p. 2436.

Woo, N. J. and E. S. G. Shaqfeh (2003). "The configurational phase transitions of flexible polymers in planar mixed flows near simple shear". In: *J. Chem. Phys.* 119, pp. 2908–2914.

Xu, D., Sanchez-Romaguera, S. Barbosa, W. Travis, J. de Wit, P. Swanb, and S. G. Yeates (2007). "Inkjet printing of polymer solutions and role of chain entanglement". In: *J. Mater. Chem.* 17, pp. 4902–4907.

Yamakawa, H. (1970). "Transport Properties of Polymer Chains in Dilute Solution: Hydrodynamic Interaction". In: *J. Chem. Phys.* 53.1, pp. 436–443.

— (1971). *Modern Theory of Polymer Solutions*. Harper & Row.

York, D. and W. Yang (1994). "The fast Fourier Poisson method for calculating Ewald sums". In: *J. Chem. Phys.* 101, pp. 3298–3300.

Zettl, U, S. T. Hoffmann, F. Koberling, G. Krausch, J. Enderlein, L. Harnau, and M Ballauff (2009). "Self-diffusion and cooperative diffusion in semidilute polymer solutions as measured by fluorescence correlation spectroscopy". In: *Macromolecules* 42, pp. 9537–9547.

Zimm, B. H. (1956). "Dynamics of polymer molecules in dilute solution: viscoelasticity, flow birefringence and dielectric loss". In: *J. Chem. Phys.* 24, pp. 269–278.

— (1980). "Chain molecule hydrodynamics by the Monte-Carlo method and the validity of the Kirkwood-Riseman approximation". In: *Macromolecules* 13, pp. 592–602.